

## Review

## Graphene-based flexible electronic devices

Tae-Hee Han<sup>a,1</sup>, Hobeom Kim<sup>b,1</sup>, Sung-Joo Kwon<sup>b,1</sup>, Tae-Woo Lee<sup>a,\*</sup><sup>a</sup> Department of Materials Science and Engineering, Seoul National University, 1 Gwanak-ro, Gwanak-gu, Seoul, 08826, Republic of Korea<sup>b</sup> Department of Materials Science and Engineering, Pohang University of Science and Technology (POSTECH), Pohang, Gyungbuk, 790-784, Republic of Korea

## ARTICLE INFO

## Article history:

Received 13 February 2017

Accepted 23 May 2017

Available online 13 June 2017

## Keywords:

Graphene  
 Flexible electronics  
 Transparent electrodes  
 Organic light-emitting diodes  
 Organic solar cells  
 Organic transistors  
 Encapsulation

## ABSTRACT

Flexible electronic devices fabricated on plastic substrate are more desirable than rigid counterparts for future displays, lightings, or solar cells. For flexible electronics to become practical, the indium-tin-oxide (ITO) electrode should be replaced due to its brittleness, increasing cost, and chemical instability. Graphene has emerged as a promising material for flexible transparent conducting electrodes because of its unique electronic and mechanical properties with high optical transmittance. Therefore, graphene has been widely used in flexible electronic devices including light-emitting diodes (LEDs), solar cells (SCs), and field-effect transistors (FETs). However, for practical applications of graphene in flexible electronics, its limitations should also be overcome. This review describes the use of graphene in LEDs, SCs and FETs, and various strategies to overcome the deficiencies of graphene to obtain highly-efficient and stable flexible electronics. Finally, we present future prospects and suggest further directions for research on graphene-based flexible electronic devices.

© 2017 Elsevier B.V. All rights reserved.

## Contents

1.	Introduction .....	2
1.1.	Flexible electronics .....	2
1.2.	General synthetic methods for graphene .....	2
2.	Inherent limitations of materials .....	3
2.1.	Indium-tin-oxide .....	3
2.2.	Graphene .....	5
3.	Flexible light-emitting diodes using graphene .....	9
3.1.	Requirements of electrode for OLEDs .....	9
3.2.	Solution-processed graphene electrodes .....	9
3.3.	Surface modifications of graphene .....	11
3.3.1.	Organic light-emitting diodes .....	11
3.3.2.	Organic-inorganic hybrid perovskite LEDs .....	15
3.4.	Air-stability for graphene .....	15
3.5.	Device architectures of OLEDs on graphene .....	19
3.6.	Optical outcoupling of OLEDs on graphene .....	22
3.7.	Device Bending stability of OLEDs on graphene .....	22
4.	Flexible solar cells with graphene .....	23
4.1.	Graphene as an electrode for organic solar cells .....	23
4.2.	Solution-processed graphene electrodes for organic solar cells .....	23
4.3.	CVD-grown graphene electrode for organic solar cells .....	23
4.3.1.	Uniform formation of interlayers on graphene .....	23
4.3.2.	Graphene doping for an electrode of OSCs .....	27
4.3.3.	Flexible OSCs that use flexible graphene electrodes .....	28

\* Corresponding author.

E-mail addresses: [twlees@snu.ac.kr](mailto:twlees@snu.ac.kr), [taewlees@gmail.com](mailto:taewlees@gmail.com) (T.-W. Lee).<sup>1</sup> These authors equally contributed to this work.

4.4.	Perovskite solar cells using graphene electrode .....	28
5.	Field-effect transistor using graphene .....	30
5.1.	Requirement of materials for FETs .....	30
5.2.	Graphene as an electrode for FETs .....	30
5.3.	Graphene as channel for FETs .....	34
6.	Flexible encapsulation using graphene .....	38
6.1.	Requirements of encapsulant for flexible electronics .....	38
6.2.	Flexible encapsulation using graphene .....	38
7.	Conclusion and outlook .....	39
	Acknowledgements .....	41
	References .....	41

## 1. Introduction

### 1.1. Flexible electronics

For human convenience, flexible electronics have been being increasingly developed in a number of areas. Flexible electronic devices that are bendable, foldable, rollable, and ultimately wearable will transform the ways in which electronics are used. Flexible electronics are built on a thin flexible substrate instead of a bulky rigid substrate, and are therefore lighter, smaller, and more comfortable than rigid electronics [1–3]. For practical use of flexible electronics, all materials in the device should have high degree of mechanical durability under bending. Several major components of current electronic devices are not flexible, and should be replaced with alternative materials: brittle inorganic materials are not compatible with flexibility. In contrast, electronic devices based on organic materials have great potential to provide flexibility or stretchability [4–6].

Indium-tin-oxide (ITO) has been the most widely used transparent conducting electrode for optoelectronic devices such as liquid crystal displays, organic light-emitting diodes (OLEDs), and organic solar cells (OSCs) for several decades. However, ITO electrode has several critical drawbacks such as poor tolerance to mechanical stress, chemical instability, and high-cost fabrication [7–11]. For successful development of flexible optoelectronics, finding a transparent and flexible replacement for ITO counterparts is a major challenge, so numerous alternative flexible conductors such as metal nanowires, conducting polymers, carbon nanotubes, and graphene have been tested [12–15]. Among them, graphene is a promising candidate because it has unique properties that are desirable in flexible electronics.

Electronic devices based on organic materials are susceptible to degradation by external influences such as oxygen and moisture, and therefore must be encapsulated for protection [16–18]. However, current encapsulants are made of glass due to its impermeability and reliability, but they are rigid and fragile; this is another critical obstacle to development of practical flexible electronics.

In this review, we focus on the use of graphene in electrodes of flexible organic or organic-inorganic hybrid LEDs, SCs and field effect transistors (FETs), and evaluate its feasibility as a flexible encapsulant (Fig. 1).

### 1.2. General synthetic methods for graphene

Graphene is a one-atomic-thick carbon sheet in which carbon atoms form a  $sp^2$ -hybridized hexagonal array. This structure yields special electrical, mechanical and optical properties that can be useful in electronics and optoelectronic devices [2,24–30]. Novoselov et al. first demonstrated high electrical mobility of single-layer graphene ( $\sim 10,000 \text{ cm}^2 \text{ V}^{-1} \text{ s}^{-1}$  at room temperature) obtained by mechanical exfoliation using scotch tape, and fabricated the world's first graphene-based transistor; the device

showed an ambipolar electric field effect and a high carrier concentration ( $10^{13} \text{ cm}^{-2}$ ) (Fig. 2) [26]. R. R. Nair et al. demonstrated that graphene also has high optical transmittance ( $T$ ), which can be calculated as  $T = 100 - 2.3N(\%)$ , where  $N$  is the number of graphene layers [31]. Single-layer graphene (SLG) has  $T \sim 97.7\%$ , which is a major advantage of a graphene electrode in optoelectronic devices. Defect-free SLG also has excellent mechanical properties; C. Lee et al. demonstrated a very high breaking strength of  $\sim 42 \text{ N/m}$ , which corresponds to Young's modulus  $\sim 1100 \text{ GPa}$  and intrinsic strength  $\sim 125 \text{ GPa}$ , and is 200 times higher than steel [32]. These outstanding electrical, optical and mechanical properties of graphene give it potential applications as a flexible electrode.

Mechanical exfoliation [26] is the simplest method to obtain SLG. Repeated application of scotch tape separates graphite into progressively-thinner flakes until SLG is obtained (Fig. 3a) [35]. Because graphite is formed of a number of  $sp^2$  covalent bonded carbon sheets, the Van-der-Waals attraction force between adjacent graphene sheets is relatively weak, so the low frictional coefficient between graphene sheets enables easy split into SLG by the weak adhesive force of scotch tape. Mechanical exfoliation method is simple, and can give defect-free SLG, but yields a limited number of small graphene flakes. Therefore, this method is not suitable for practical production of graphene films for flexible electronics.

Chemical synthesis can mass-produce large-area graphene (Fig. 3b). The process entails oxidation of graphite and then reduction of the resultant graphene oxide (GO). The most common method to chemically synthesize graphene sheets is Hummer's method [36], in which graphite is oxidized using a strong acid and oxidation agent, so water molecules can intercalate between graphene sheets because of the high hydrophilicity of GO. This process increases the distance between pairs of graphene sheets to  $6\text{--}12 \text{ \AA}$ , and thereby enables exfoliation of GO sheets by extended ultrasonication [37]. However, GO sheets obtained by Hummers method contain functional groups such as hydroxyl, carboxylic, and epoxy groups, which significantly degrade most of the unique properties of SLG. Therefore, to recover specific nature of graphene, GO sheets should be chemically reduced to remove the functional groups.

G. Eda et al. reported a solution-processed deposition of reduced GO (rGO) film; the method produces uniform graphene film with controllable thickness [38]. The large-area film is composed of various rGO flakes with thickness from a single layer to few layers. Therefore, electronic and optical properties of rGO film such as sheet resistance ( $R_{sh}$ ) and  $T$  can be controlled over several orders of magnitude by controlling solution-based deposition parameters [38]. The thinnest rGO film exhibited ambipolar transistor characteristics as reported in an SLG transistor formed by mechanical exfoliation, and the film had  $R_{sh} \sim 43 \text{ k}\Omega/\text{sq}$  after reduction of GO and thermal annealing. The solution-based easy fabrication of graphene film is a major advantage of chemical synthesis, but the oxidation-reduction

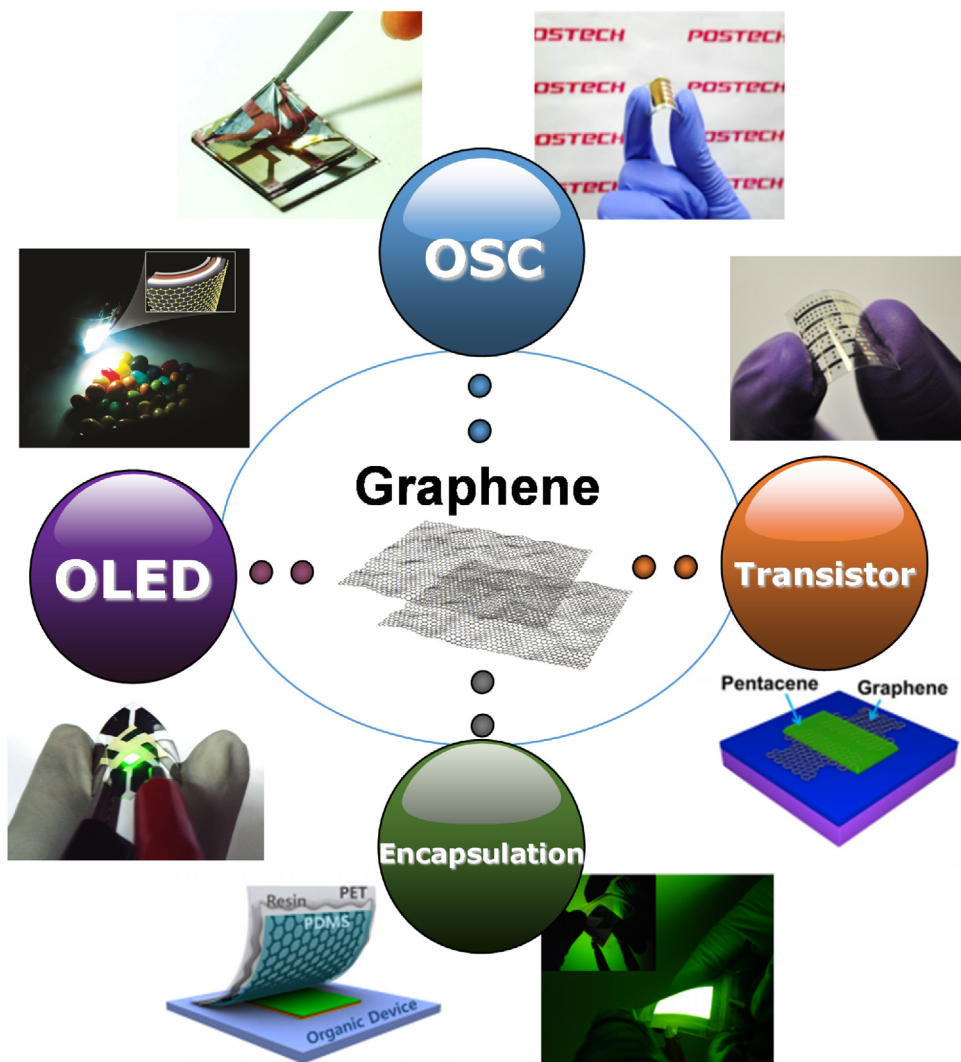


**Fig. 1.** Applications of graphene to flexible electronics such as OLEDs, OSCs, OFETs, and encapsulations. Reproduced from (left) [12] Copyright 2012, Nature Publishing Group, (top) [19] Copyright 2014 American Chemical Society, [20] Copyright 2014 IOP Publishing, (right) [21] Copyright 2012 IOP Publishing, [22] Copyright 2015 Nature Publishing Group, (bottom) [23] Copyright 2016 American Chemical Society.

process degrades the electrical properties of rGO film, and this is a significant obstacle to practical applications of graphene as transparent electrodes.

Chemical vapor deposition (CVD) can produce high-quality graphene film of large area (Fig. 3c) [39]. CVD uses catalytic transition metals such as Ni, Cu, and Pt. CVD growth of graphene can be categorized into two mechanisms: i) carbon segregation and precipitation and ii) surface growth according to carbon solubility in metal catalysts [40]. Metal catalysts such as Ni that have high solubility for carbon, absorb carbons that are released by decomposition of hydrocarbon sources at high temperature (~1000 °C), then carbons precipitate on the metal surface and form graphene upon cooling of the substrate. In contrast, catalytic metals such as Cu that have low solubility for carbon enable surface growth of graphene; the adsorbed hydrocarbon sources decompose on the surface of the metal at high temperature. Nucleation and continuous growth allow formation of large-area SLG on the catalyst. After the catalytic metals are chemically etched away, the graphene can be transferred onto the target substrate.

Roll-to-roll production of 30-inch scale SLG film has been achieved using CVD on copper foil as a large-area metal catalyst by

S. Bae et al.; chemical doping of SLG resulted in low  $R_{sh} \sim 125 \Omega/\text{sq}$  with  $T=97.4\%$  [34]. Stacking of SLG further reduced  $R_{sh}$  to ~30  $\Omega/\text{sq}$ , but retained  $T \sim 90\%$ , which is comparable to  $T$  of an ITO electrode. Use of CVD may be the most practical way to achieve large-scale growth of high-quality graphene for flexible electronics.

## 2. Inherent limitations of materials

### 2.1. Indium-tin-oxide

ITO has high electrical conductivity and high  $T$  for visible light, and therefore has been an essential component in optoelectronic devices such as liquid crystal displays (LCDs), touch panels, OLEDs, and OSCs for several decades. ITO film is fabricated by high-vacuum sputtering, and the most-frequently-used ITO film is composed of  $\text{In}_2\text{O}_3$  doped with 10%  $\text{SnO}_2$ ; substitution of  $\text{Sn}^{4+}$  for  $\text{In}^{3+}$  increases electron density in the film; therefore ITO has low resistivity ( $<10^{-3} \Omega/\text{cm}$ ) and high electrical conductivity ( $\sim 10 \Omega/\text{sq}$ ) [8]. Metal ion substitution into ITO requires high energy, so high-temperature annealing ( $>300^\circ\text{C}$ ) should be applied

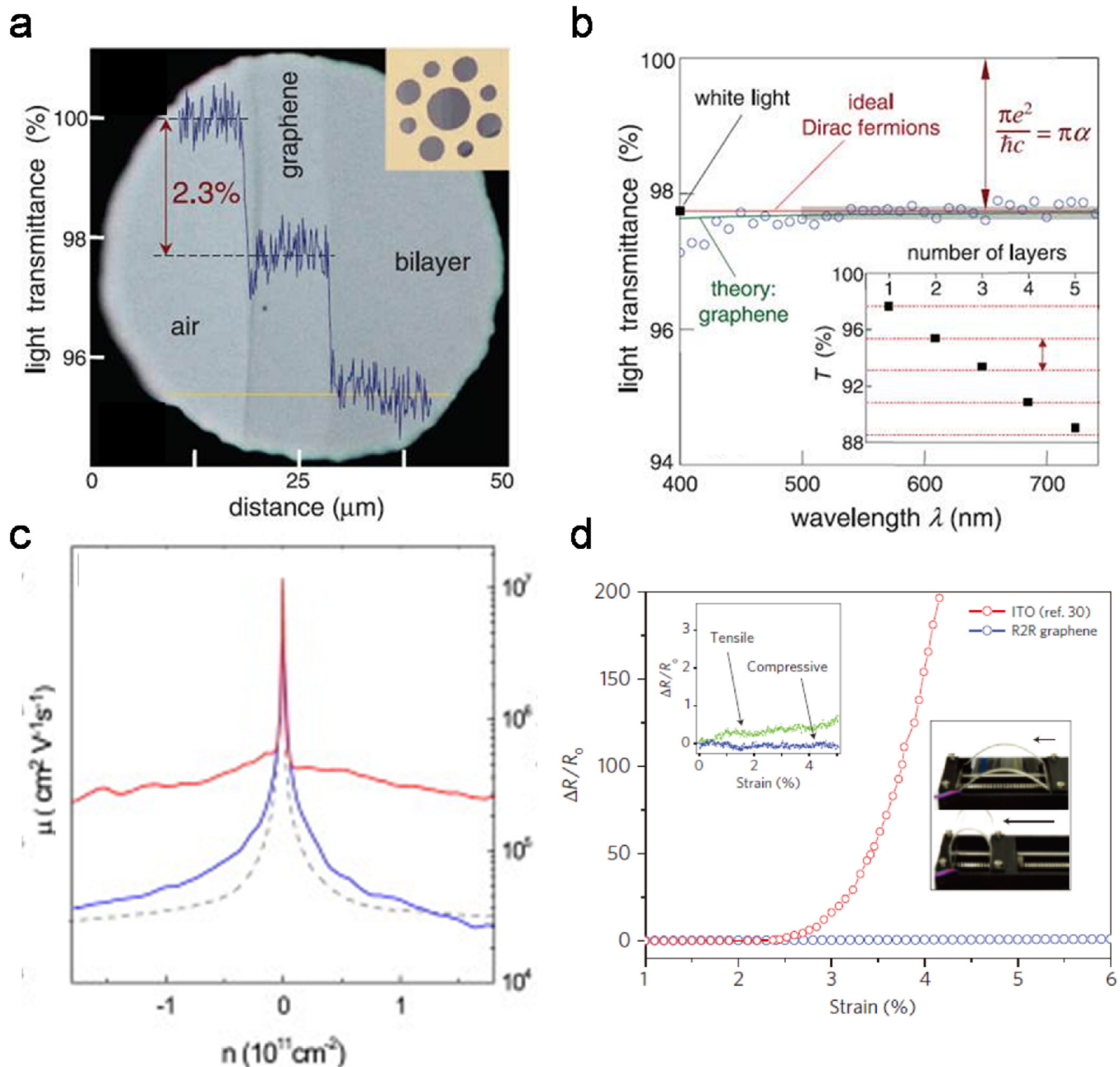


**Fig. 2.** (a) Effect of number (1, 2) of graphene layers on optical transmittance, (b) Effect of the number of graphene layers on transmittance of white light. Reproduced from [31] Copyright 2008, American Association for the Advancement of Science, (c) Effect of carrier density on carrier mobility in suspended graphene-based device. Reproduced from [3] Copyright 2008, Elsevier, (d) Change in resistance of graphene film produced by roll-to-roll process as a function of strain. Reproduced from [34] Copyright 2010, Nature Publishing Group.

to obtain crystalline ITO film that has high electrical conductivity [9]. However, high-temperature annealing is not suitable for plastic substrates which have low thermal resistance.

Several factors are driving the need to find a replacement for ITO electrodes. The cost of ITO is increasing due to depletion of raw materials used in its fabrication. Mechanical stress drastically decreases the electrical conductivity of ITO films because crystalline ITO is easily cracked by mechanical strain  $>1\%$  (Fig. 4a,b) [10,11,42]. Initiated small cracks propagate as bending or tensile stress increases; they join together to form larger cracks, which cause delamination of ITO films from the plastic substrate [10,11]. ITO is also chemically unstable; this is a major problem for organic electronic devices. ITO is very vulnerable under acidic atmosphere. An acidic aqueous solution of PEDOT:PSS can easily

etch ITO electrodes, and release metal atoms into overlying layers. M. P. de Jong et al. reported that the interface between ITO and PEDOT:PSS is not stable, and demonstrated instability of ITO by Rutherford backscattering studies [43]. Spin-coating of PEDOT:PSS solution immediately diffuses 0.02 at.% of In into PEDOT:PSS layer, and thermal annealing of the film at  $100^\circ\text{C}$  increases the In concentration in the layer to 0.2 at.% (Fig. 4c). S. T. Lee et al. also reported that device operation significantly increases the penetration depth of metal atom diffusion even in OLEDs that do not include an acidic polymer [44]. Electrical migration of In ions reaches the cathode of OLEDs under device operation, and these diffused metal atoms reduce the performances of OLEDs. K. W. Wong et al. used self-assembled monolayer (SAM) on top of the ITO anode to block detrimental reactions between ITO and PEDOT:PSS

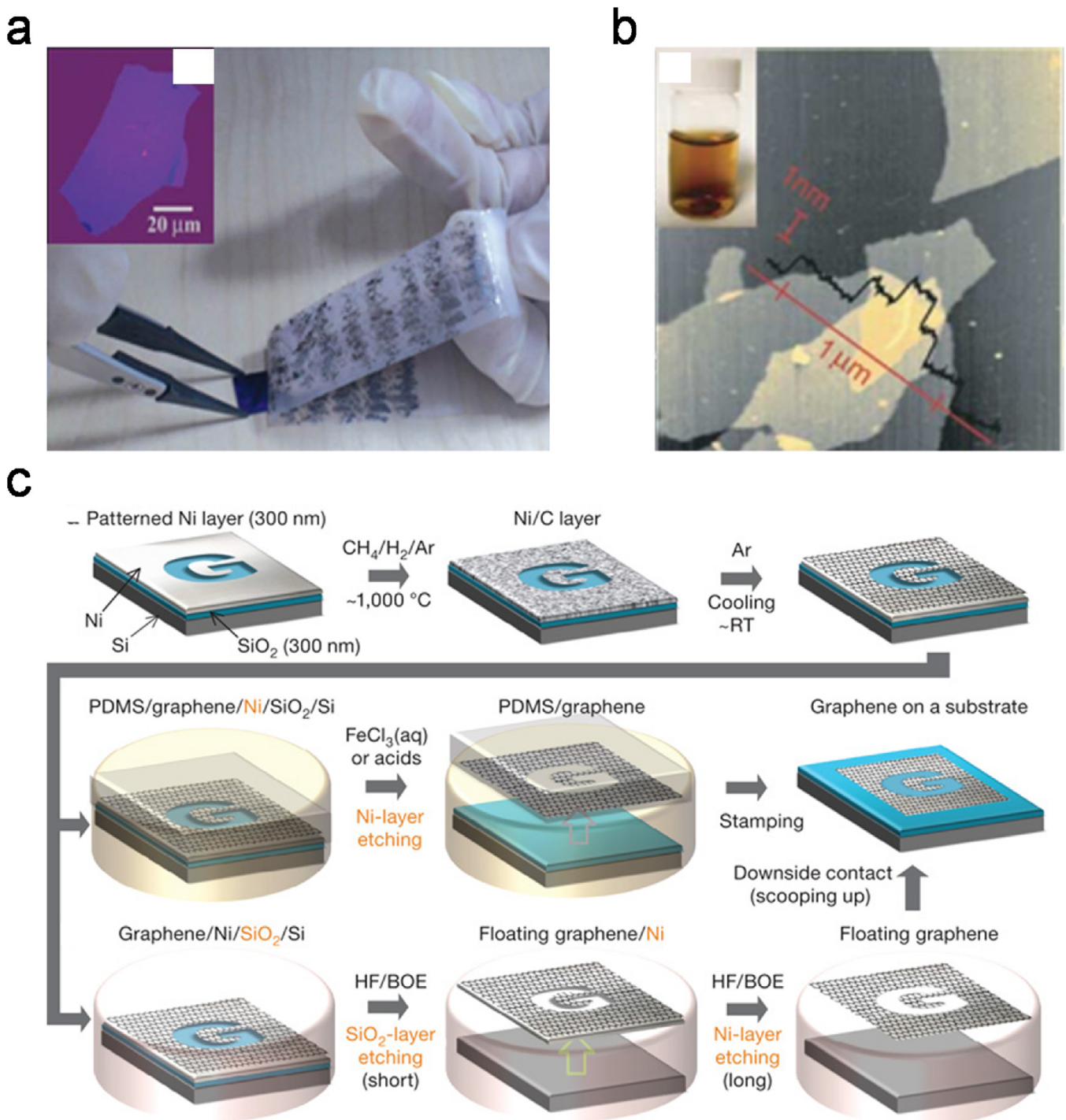


**Fig. 3.** (a) Mechanical exfoliation of graphene using scotch tape (inset: single-layer graphene flake transferred to Si wafer). Reproduced from [35] and [26] Copyright 2012, Nature Publishing Group and Copyright 2014, American Association for the Advancement of Science, (b) AFM image of chemically-exfoliated graphite oxide sheets on mica substrate. Reproduced from [41] Copyright 2006, Nature Publishing Group, (c) Schematic illustration of growth, etching, transfer process of CVD-grown graphene. Reproduced from [39] Copyright 2009, Nature Publishing Group.

[45]. Passivation of ITO by using a short-chain alkylsiloxane SAM effectively blocked etching and subsequent diffusion of metal atoms from ITO into organic layers. By acting as charge traps and exciton quenchers (or non-radiative recombination centers), diffused metal species degrade charge injection, transport, and electroluminescent properties in organic optoelectronic devices (Fig. 4d) [12,44,46]. Therefore, chemical instability is also a major impediment to use of ITO in flexible optoelectronics. ITO should be replaced with alternative transparent conducting electrodes to

develop flexible optoelectronics because of its incompatible fabrication process with plastic substrate, increasing cost, brittleness, and release of metal species.

## 2.2. Graphene

Graphene has exceptional charge mobility, thermal conductivity, and ultra-high mechanical strength. However, pristine graphene has several drawbacks that impede its practical

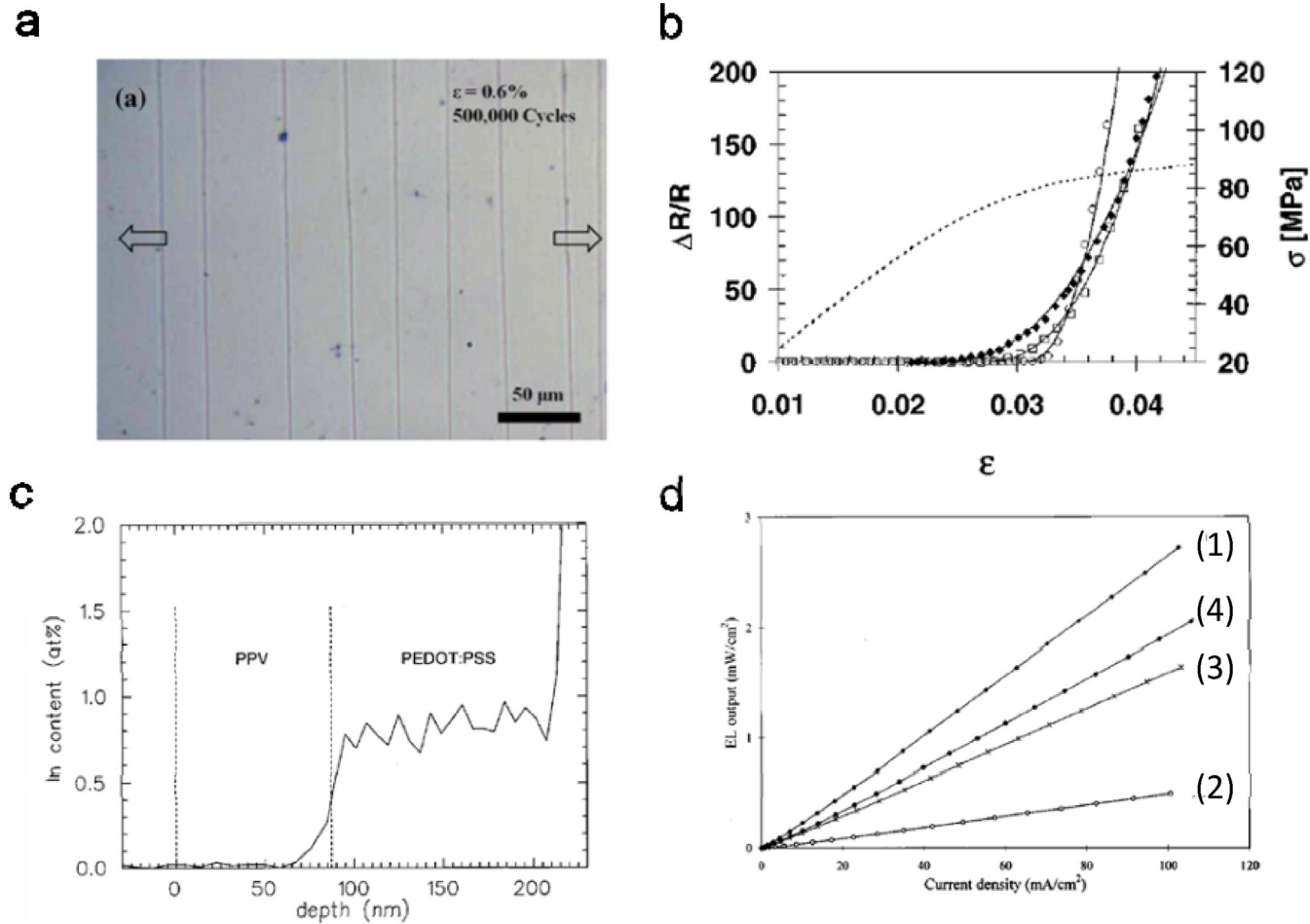


**Fig. 4.** (a) Optical image of cracked ITO on PET substrate against 500,000 cycles of bending with 0.6% strain. Reproduced from [47] Copyright 2013, Elsevier, (b) Change in resistance of ITO on PET as a function of strain (thickness of ITO:  $\blacklozenge$  105,  $\square$  42,  $\circ$  16.8 nm) and strain-stress curve (dotted line). Reproduced from [11] Copyright 2000, American Institute of Physics, (c) Depth profile of In content in PPV/PEDOT:PSS film exposed in air for 2 d measured by Rutherford backscattering. Reproduced from [43] Copyright 2000, American Institute of Physics, (d) Electroluminescence output as a function of current density in OLEDs using (1) Alq<sub>3</sub> (75 nm), (2) In-doped Alq<sub>3</sub> (15 nm)/Alq<sub>3</sub> (60 nm), (3) Alq<sub>3</sub> (15 nm)/In-doped Alq<sub>3</sub> (15 nm)/Alq<sub>3</sub> (45 nm), and (4) Alq<sub>3</sub> (50 nm)/In-doped Alq<sub>3</sub> (15 nm)/Alq<sub>3</sub> (10 nm). Reproduced from [44] Copyright 1999, American Institute of Physics.

application as an electrode. Pristine graphene has higher  $R_{sh} > 300 \Omega/\text{sq}$  and lower work function ( $WF$ )  $\sim 4.4 \text{ eV}$  than those of ITO ( $\sim 10 \Omega/\text{sq}$ ,  $4.8 \text{ eV}$ ), and is therefore not appropriate for use as an electrode in organic and organic-inorganic hybrid electronics. High  $R_{sh}$  makes a device conduct or collect limited current at a given applied bias, and low  $WF$  causes a large energy barrier (or offset) between the anode and the overlying layer; as a result, hole injection is reduced in OLEDs, and open circuit voltage is decreased in OSCs. The changes reduce device efficiency compared with ITO-based counterparts [12,48–50]. To overcome these disadvantages of pristine graphene for practical applications, various doping methods such as substitutional doping [51–55] and charge-transfer doping [12,34,48,56–58] have been conducted on pristine graphene to tailor its electrical properties.

Substitutional doping can alter the properties of graphene [51–55]. Introducing hetero-atoms into the graphene lattice substantially modifies its electronic structure, and thereby changes various electrical properties including its zero bandgap, electrical conductivity, and  $WF$  (Fig. 5a,b) [53,55,59,60]. N and B atoms are similar in size to C atoms, and are therefore commonly used for substitutional doping of graphene. Substitutionally-doped graphene can be prepared by CVD using hetero-atom precursors. N-doped graphenes are commonly synthesized by supplying gaseous NH<sub>3</sub> and CH<sub>4</sub> as N and C sources, respectively [53]. Similarly, B-doped graphene can be synthesized using

B-containing precursors such as boronic acid [60]. Substitutional doping provides precise modifications of electrical properties of graphene, but disrupts its electronic nature, and therefore seriously degrades its electrical conductivity [55,60].

Charge-transfer doping is another method to control the electrical properties of graphene [12,34,48,56,61,62]. Electronic charge transfer doping is spontaneously caused by difference between Fermi energy level of graphene and electron affinity of acceptor or ionization potential of donor molecule [57,63]. For example, when the highest occupied molecular orbital (HOMO) energy level of a semiconducting dopant is higher than the Fermi energy level of graphene, the dopant donates its electrons to the graphene, so its electron concentration increases. In contrast, when semiconducting dopant material has lower lowest unoccupied molecular orbital (LUMO) energy level than the Fermi energy level of graphene, dopants withdraws electrons from graphene, and its hole concentration increases (Fig. 6a) [57,63]. Also, when the surface-adsorbed dopant molecule takes part in electrochemical redox reaction with graphene, electrochemical charge transfer doping occurs, and it depends on reduction potential of dopant molecules and Gibbs free energy of its reaction (Fig. 6b, c) [57,64]. Charge transfer doping is generally considered that a dopant with electron donating group leads n-type doping, and that a dopant with an electron-withdrawing group leads to p-type doping of graphene when dopant molecules are adsorbed on the surface of

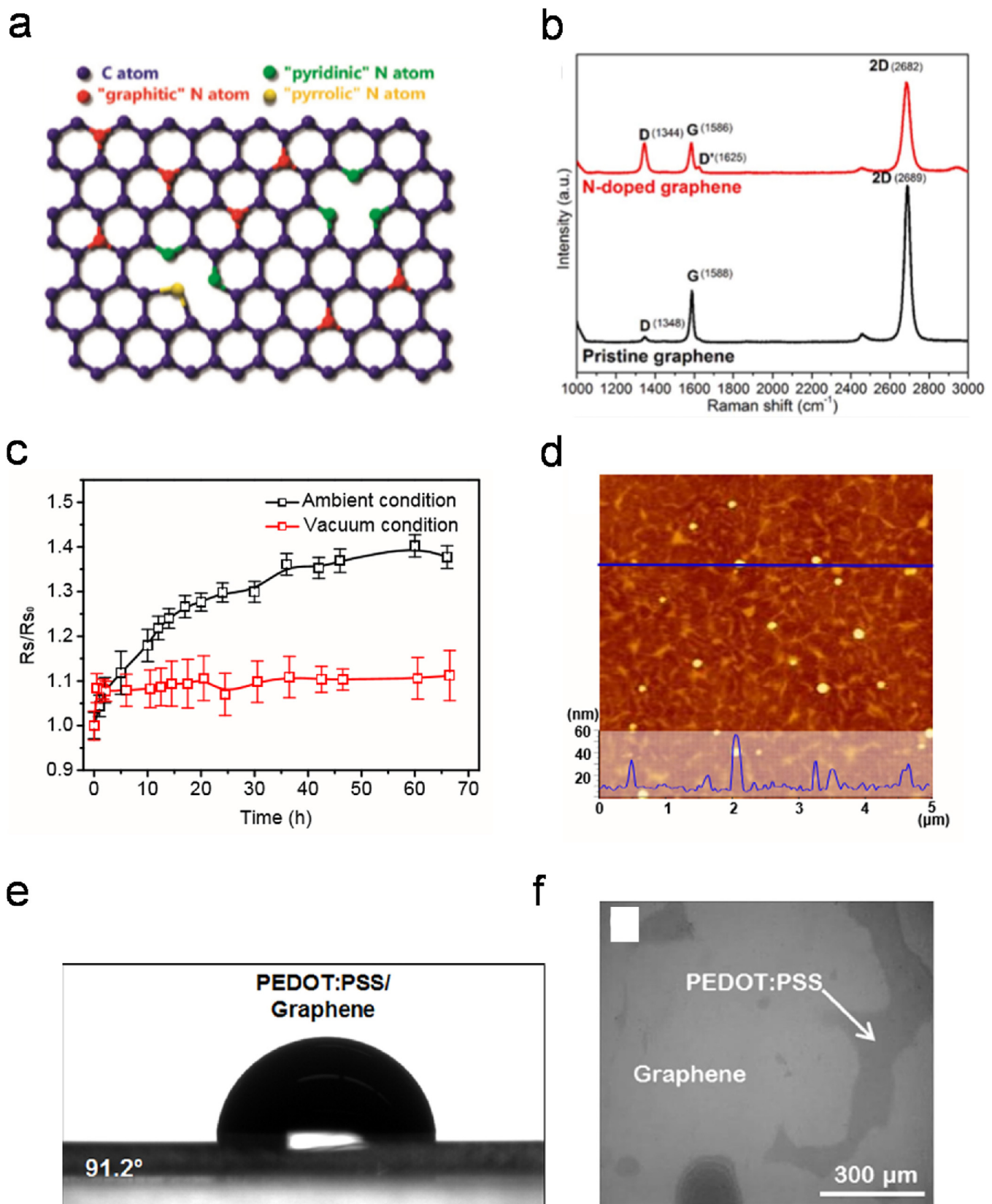


**Fig. 5.** (a) Schematic illustration of substitutionally n-doped graphene by CVD growth. Reproduced from [53] Copyright 2009, American Chemical Society, (b) Raman spectra of substitutionally n-doped graphene by CVD and pristine graphene. Reproduced from [55] Copyright 2012, Nature Publishing Group, (c) Change in normalized sheet resistance of  $\text{HNO}_3$ -doped graphene as a function of time in ambient or vacuum condition, (d) AFM image of  $\text{AuCl}_3$ -doped graphene surface. Reproduced from [12] Copyright 2012, Nature Publishing Group, (e) Contact angle of PEDOT:PSS on graphene. Reproduced from [68] Copyright 2013, American Chemical Society, (f) Optical microscopy image of PEDOT:PSS coated on graphene. Reproduced from [69] Copyright 2015, Elsevier.

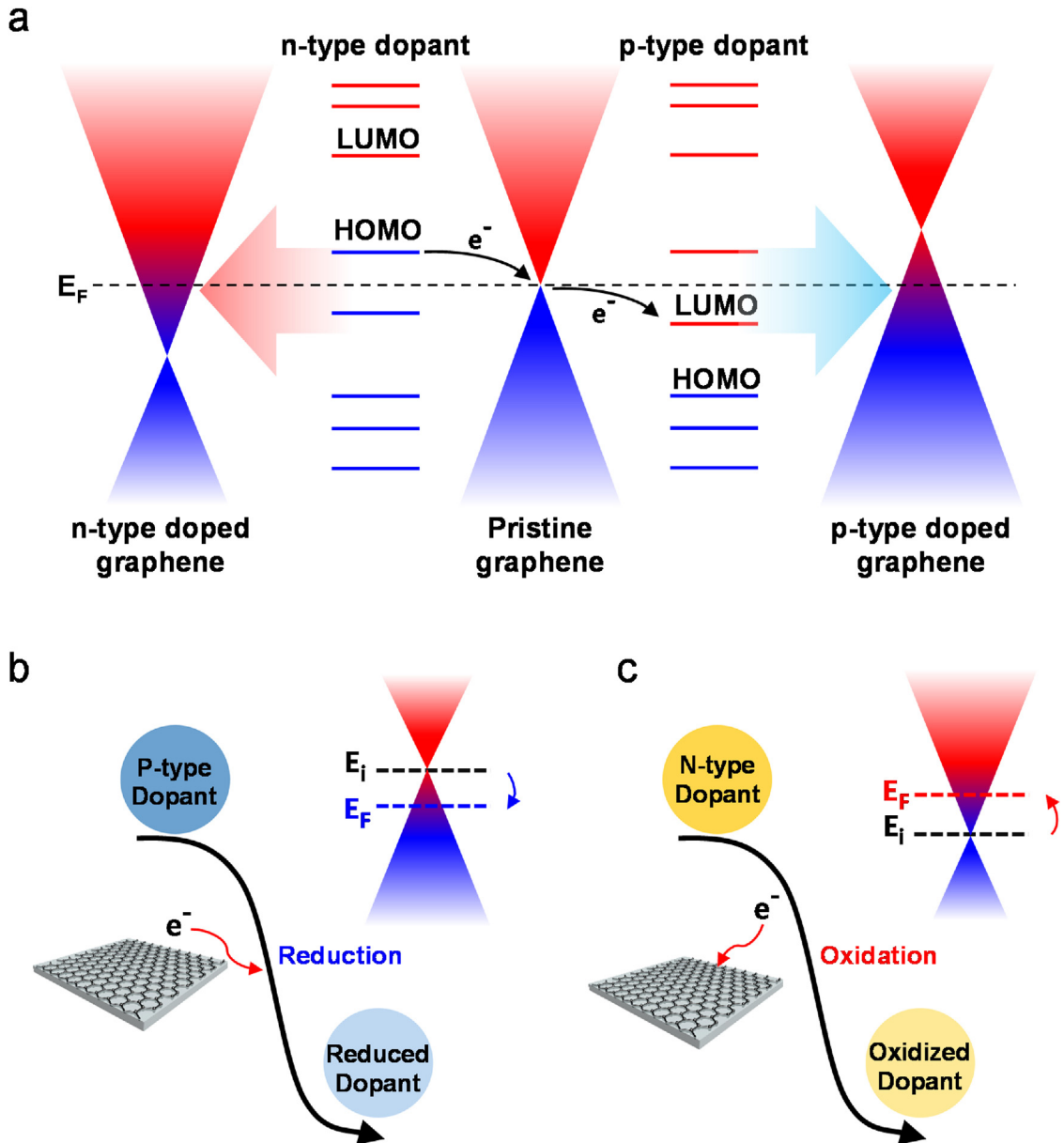


**Fig. 6.** (a) Schematic illustration of charge transfer doping mechanism according to energy levels of semiconducting dopant materials, (b) p-type doping by reduction of p-type dopant material, and (c) n-type doping by oxidation of n-type dopant material.

graphene [65]. Electrostatic potential caused by dipole moment of charge transfer complex between graphene and dopant molecule induces a doping effect in graphene [66].

Graphene doping formed by spontaneous charge transfer does not substantially change the electronic structure of graphene and thus degrades its properties in graphene. Charge transfer doping of graphene has been generally performed using various dopants including inorganic acids and metal chlorides. Inorganic acids (e.g., HCl, HNO<sub>3</sub>, H<sub>2</sub>SO<sub>4</sub>) have been commonly used as p-type chemical dopants for graphene because they can form charge transfer complexes with graphene by withdrawing electrons from the graphene, and increased hole concentration in graphene have improved its electrical conductivity and its WF [12,34,67]. However, inorganic small-molecule dopants are highly volatile, so they cannot provide sufficient doping stability in ambient conditions; the  $R_{sh}$  of graphene doped by inorganic small-molecule acid gradually increases in ambient condition (Fig. 5c) [12,48]. Metal chlorides have also been used as a charge-transfer p-type

dopant of graphene, and showed efficient p-type doping that resulted in high electrical conductivity ~30 Ω/sq and high WF ~5 eV [12,56]. However, reduction of the metal cations causes large metal particles to form on the graphene surface (Fig. 5d). These particles on graphene can protrude severely, and thus increase electrical leakage or short current in thin-film devices [12]. Doping of graphene with metal chloride can also cause noticeable reduction in  $T_c$ ; this is another disadvantage in opto-electronic devices [56].

Graphene is hydrophobic, so aqueous solutions do not coat it uniformly. Development of solution-processed flexible electronic devices requires that this problem be solved (Fig. 5e,f). Complete coverage on the graphene by an interfacial buffer layer is vital to facilitate charge injection or extraction and to avoid local shorting through the prominent surface on the electrode [20,68–72]. O<sub>2</sub>-plasma or ultraviolet-ozone surface treatment of graphene can change its surface from hydrophobic to hydrophilic by inducing formation of oxygen-containing functional groups, but

these processes greatly degrade graphene's electrical properties by disrupting its  $sp^2$  hybridized carbon networks [49,73]. Therefore, achievement of uniform coating of an interfacial layer on graphene electrode requires development of surface modification methods that do not influence graphene's electrical properties.

### 3. Flexible light-emitting diodes using graphene

#### 3.1. Requirements of electrode for OLEDs

OLEDs are composed of electroluminescent organic materials sandwiched by two metallic electrodes. When a forward bias is applied to the electrodes, holes and electrons are injected through HOMO and LUMO energy levels of adjacent organic materials from anode and cathode, respectively. Injected charge carriers are transported to the electroluminescent organic emitting layer (EML), where electrons and holes recombine; this process generates light, which can exit from the device through a transparent conducting electrode. Therefore, at least one electrode should have high  $T$  to minimize optical light loss. Charge balance strongly affects quantum efficiency of OLEDs, so efficient charge injection from electrodes, and subsequent balanced charge transport, are important to obtain highly-efficient and stable OLEDs [74–78]. When an anode has low electrical conductivity, current is limited at a given applied voltage, so luminous power efficiency of OLEDs can be reduced. Also, when the anode has a low WF, a large energy barrier forms between the anode and the overlying organic layer; as a result, luminous current and power efficiencies of OLEDs decrease. Because pristine graphene has lower WF ( $\sim 4.4$  eV) than that of ITO ( $\sim 4.8$  eV), simple replacement of ITO with graphene increases the energy barrier to hole injection between anode and adjacent organic layer ( $> 5.4$  eV) in the OLED (Fig. 7) [12,48–50]. For these reasons, the anode must have high electrical conductivity and WF to minimize voltage drop at the electrode, and to provide sufficient charge injection into the overlying organic hole-transporting layer (HTL) or EML. To actualize practical applications of flexible OLEDs, both electrodes should tolerate a high degree of flexion without degradation of electrical properties [12,79,80]. Additionally, the electrode should have a smooth surface morphology to prevent local thinning, which causes electrical leakage and short current in thin-film devices [12,48].

Environmental stability of the electrode is also necessary for practical applications of flexible OLEDs. OLEDs that use a polymeric hole injection layer (HIL) on top of ITO have inefficient charge injection and low device efficiency because the solution process to

deposit the conventional acidic hole-injecting conducting polymer (PEDOT:PSS) on ITO easily etches its surface and release metal species (Section 2.1) [12,44,46]. Graphene doped with volatile dopants is also unstable in ambient conditions [12,56,81,82]. Because electrical properties of doped graphene are gradually degraded in ambient condition, this instability is a major impediment to practical use of flexible OLEDs. Therefore, the ideal flexible electrode should have good  $T$ , smooth surface, flexibility, high electrical conductivity, appropriate WF, and high environmental stability.

#### 3.2. Solution-processed graphene electrodes

The first OLEDs that use a graphene anode were reported in 2010 [83]; the graphene anode was solution-processed graphene film formed by spin-coating of a water-based dispersion of functionalized graphenes. The solution-processed graphene film was  $\sim 7$  nm thick, and had  $R_{sh} \sim 800 \Omega/\text{sq}$  and  $T \sim 82\%$ ; this  $R_{sh}$  of graphene film was much higher than the theoretical estimate, because solution-processed graphene film incorporates numerous grain boundaries and defects. The OLEDs used a device structure [glass/graphene/PEDOT:PSS/N,N'-Di(1-naphthyl)-N,N'-diphenyl-(1,1'-biphenyl)-4,4'-diamine (NPD)/tris-(8-hydroxyquinoline)aluminum ( $\text{Alq}_3$ )/LiF/Al]; the device that used graphene showed higher operating voltage and lower luminous efficiency ( $\sim 0.2\% \text{ ph/el}$ ,  $\sim 0.3 \text{ lm/W}$ ) because the graphene anode has lower electrical conductivity and WF than those of ITO (Fig. 8a, b). Layer-by-layer assembly of rGO has also been used to precisely control thickness, electrical conductivity, and  $T$  of graphene electrodes [84]. By alternately depositing negatively-charged and positively-charged rGO, a solution-processed graphene electrode was fabricated; it had  $2.5 \text{ k}\Omega/\text{sq}$  at  $T = 75\%$  ( $\sim 15$  layers). Fluorescent OLEDs with rGO anode showed maximum luminance  $\sim 7800 \text{ cd/m}^2$  and luminous efficiency  $\sim 0.1 \text{ cd/A}$  [84]. Although layer-by-layer assembly provides controllability of thickness, electrical, and optical properties of graphene film, the process also yields higher  $R_{sh}$ , lower WF, and lower  $T$  of graphene anode than those of ITO, thereby degrading the luminous efficiencies of OLEDs.

A new way to produce a solution-processed graphene-composite electrode for OLEDs was developed to achieve improved electrical properties; the method entails oxidation of graphite to GO, then use of a small-molecule surfactant (sodium dodecylbenzene sulfonate, SDBS) to stabilize the GO and to achieve high solubility (Fig. 8c) [85]. To increase the electrical conductivity of graphene film, the modified GO solution is reduced using hydrazine. Conventional methods typically result in GO that has

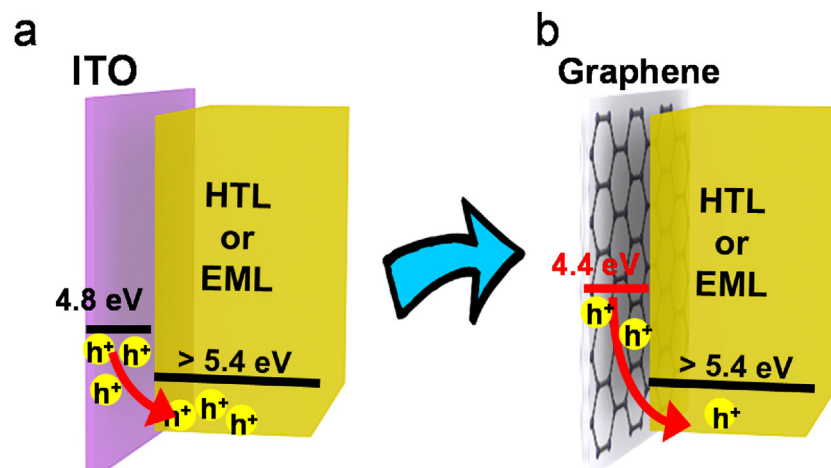


**Fig. 7.** Schematic illustration of energy barrier for hole injection from ITO and pristine graphene to overlying hole transport layer or emitting layer.

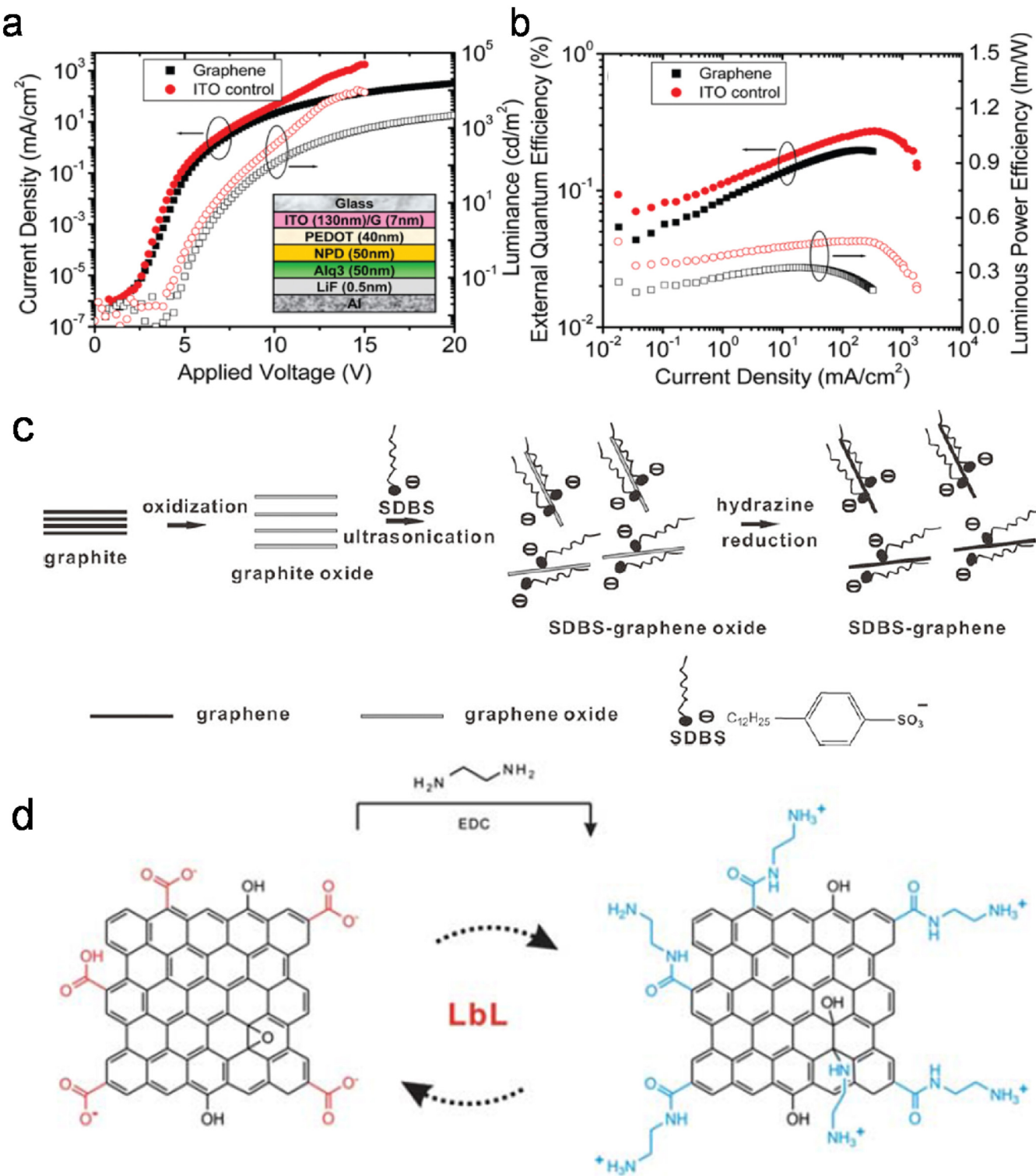


**Fig. 8.** (a) Current density and luminance, and (b) External quantum efficiency as a function of voltage in OLEDs with solution-processed reduced graphene oxide anode and ITO anode. Reproduced from [83] Copyright 2009, American Chemical Society, (c) Schematics of SDBS-graphene synthesis. Reproduced from [85] Copyright 2010, Wiley-VCH, (d) Schematics of layer-by-layer assembly to form multilayered reduced graphene oxide film. Reproduced from [84] Copyright 2011, The Royal Society of Chemistry.

limited size  $\sim 200 \text{ nm}$  to several micrometers [36,37]. The size of resulting surface-functionalized graphene flakes was  $>10 \mu\text{m}$ , which can enhance electrical properties of solution-processed graphene networks. The composite electrode composed of PEDOT:PSS and functionalized graphene has high electrical conductivity ( $\sim 10^5 \text{ S/m}$ ;  $\sim 80 \Omega/\text{sq}$ ) with  $T \sim 79\%$ . Improved electrical conductivity of graphene composite electrode increased

electroluminescent efficiency in fluorescent OLEDs [anode/PEDOT:PSS/NPB/Alq<sub>3</sub>/LiF/Al]  $\sim 3.9 \text{ cd/A}$  over those with solution-processed graphene electrodes. Multilayered graphene film was also fabricated by alternate deposition of positively-charged and negatively-charged GO, and N,N,N-trimethyl-1-dodecanaminium bromide (CTAB) and SDBS were used as cationic and anionic surfactants, respectively, to improve the quality of graphene film

formed from GO dispersions [86] (Fig. 8d). N atoms in the CTAB cause n-type doping of GO during its reduction. After reduction of GO at 1000 °C, multilayered graphene film formed by 13 cycles of deposition showed  $R_{sh} \sim 298 \Omega/\text{sq}$  at  $T=60\%$ . Fluorescent OLEDs were fabricated with the multilayered graphene formed by the layer-by-layer deposition [anode/PEDOT:PSS/NPB/Alq3/Liq/Al], and showed slightly higher current efficiency  $\sim 4.5 \text{ cd}/\text{A}$  than those with solution-processed graphene electrodes.

Solution processing of functionalized rGO has the advantage of being compatible with mass production of graphene electrode, but rGO film still includes numerous surface oxygen-containing functional groups such as hydroxyl, carboxyl, and epoxy which degrade electrical conduction of graphene film. Although methods exist to increase the processability and controllability of graphene film by solution process, OLEDs based on solution-processed graphene anode have low device efficiency due to insufficient electrical conductivity. Therefore, developments of methods to reduce GO or to dope rGO to increase the electrical conductivity of solution-processed graphene electrode are essential for practical mass-production of graphene-based flexible OLEDs.

### 3.3. Surface modifications of graphene

#### 3.3.1. Organic light-emitting diodes

A graphene electrode with high electrical conductivity that is comparable to that of ITO is essential to achieve high efficiency in flexible OLEDs. A CVD method can provide better film quality and electrical conductivity of graphene than those of solution-processed rGO, so flexible OLEDs that use a CVD-grown graphene have been developed for high-efficiency flexible OLEDs. However, because pristine graphene grown by CVD method also has relatively high  $R_{sh} > 300 \Omega/\text{sq}$  and low  $WF \sim 4.4 \text{ eV}$  compared with ITO, OLEDs with pristine graphene cannot provide efficient hole injection from the anode to overlying organic layers. Therefore, for graphene to be useful as an anode in OLEDs, the electrical and electronic properties of pristine graphene should be modified to have lower  $R_{sh}$  and higher  $WF$  than pristine graphene does.

A multi-layered graphene was grown by CVD method using Ni catalyst, then transferred to glass substrate from Si wafer by using a poly(methyl methacrylate) (PMMA) supporter for an anode in OLEDs [87]. The number of graphene layers grown by CVD method

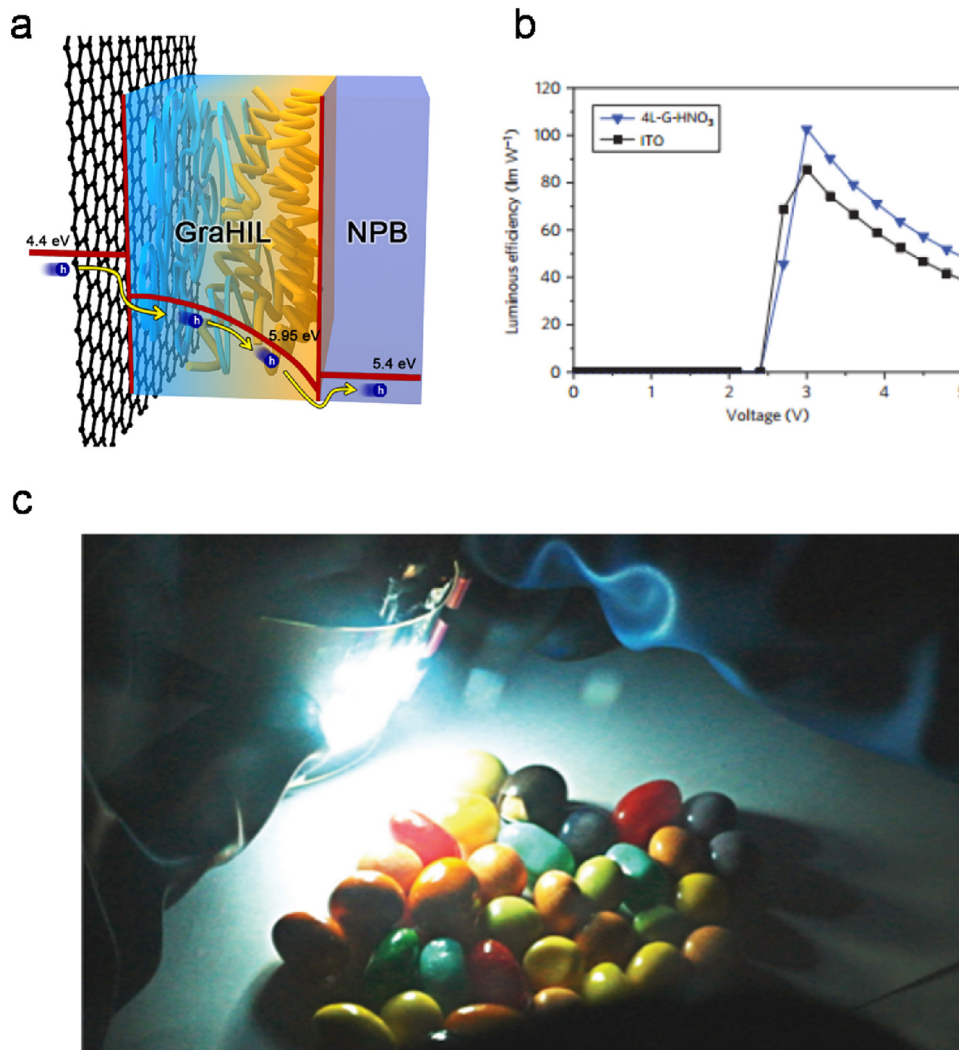


**Fig. 9.** (a) Schematic illustration of hole injection from graphene anode to overlying HTL through self-organized polymeric HIL that develops gradually-increasing ionization potential, (b) Luminous power efficiencies of green phosphorescent OLEDs with graphene anode and ITO anode, (c) Large-area flexible solid-state-lighting device using white OLED on a modified graphene anode. Reproduced from [12] Copyright 2012, Nature Publishing Group.

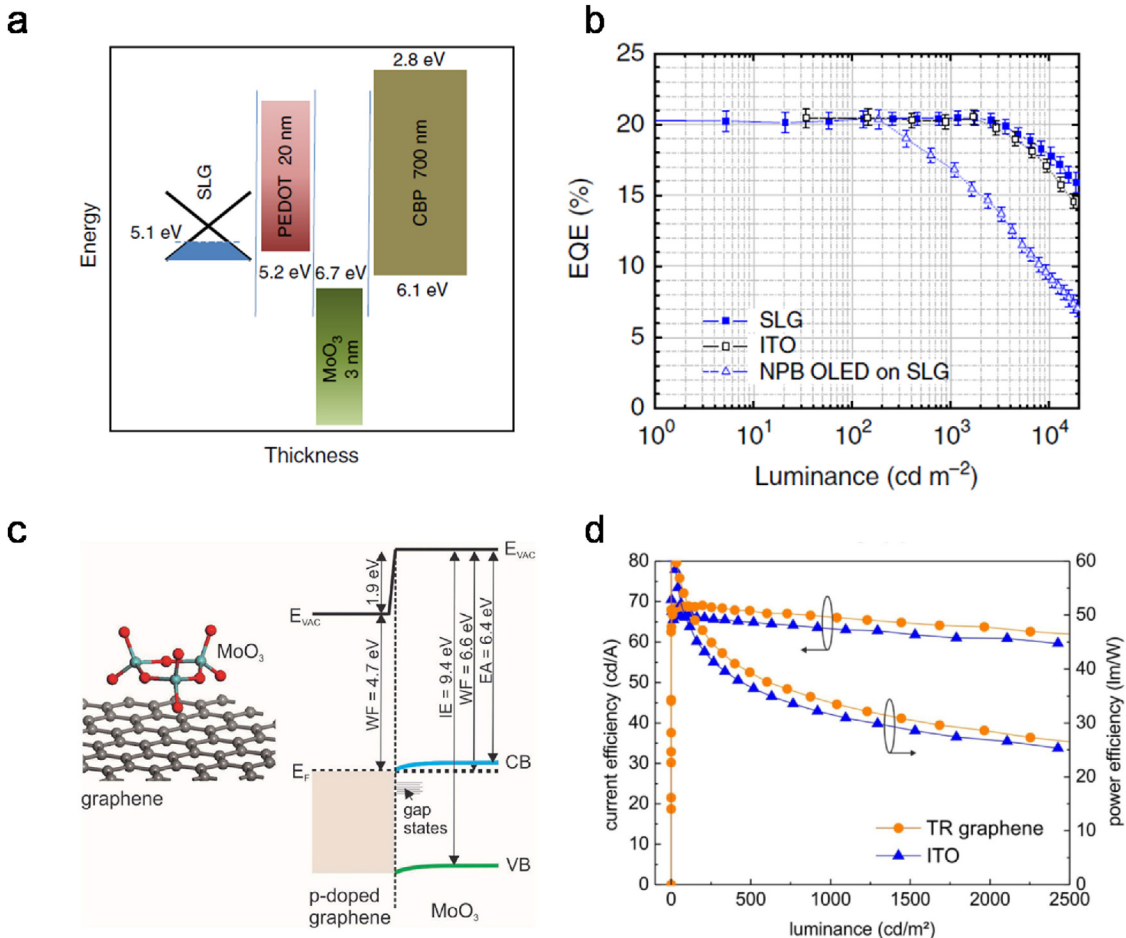


**Fig. 10.** (a) Schematic energy level diagrams of SLG anode/PEDOT:PSS/MoO<sub>3</sub>/CBP, (b) External quantum efficiency of green phosphorescent OLEDs with SLG and ITO. Reproduced from [89] Copyright 2013, Nature Publishing Group, (c) Schematic illustration of graphene and MoO<sub>3</sub> and their energy level alignment, (d) Current and power efficiencies of green phosphorescent OLEDs with tri-layered graphene anode and ITO anode. Reproduced from [90] Copyright 2014, Nature Publishing Group.

was ~20, and the total thickness of the graphene film was ~6–7 nm. It had improved  $R_{sh}$  ~310  $\Omega$ /sq and  $T$  ~85% compared with solution-processed graphene films because CVD-grown graphene does not have numerous defect sites including oxygen-containing functional groups [83–85]. However, phosphorescent OLEDs that use a Ni-catalyzed-CVD-grown multilayered graphene anode [Al/glass/multilayered graphene/V<sub>2</sub>O<sub>5</sub>/NPB/CBP: Ir(ppy)<sub>2</sub>(acac)/Bphen/Bphen: Cs<sub>2</sub>CO<sub>3</sub>/Sm/Au] had still insufficient luminous efficiencies ~0.75 cd/A and 0.38 lm/W, which are much lower than those of typical ITO-based devices. Although a 5-nm-thick layer of V<sub>2</sub>O<sub>5</sub> which can give high WF ~5.4 eV was deposited between anode and HTL (i.e., NPB) to increase the efficiency of hole injection from the graphene anode, the multilayered graphene grown using Ni catalyst had a rough surface which can cause leakage current in the device [87]. Also, still high  $R_{sh}$  of multilayered graphene (>300  $\Omega$ /sq) also could degrade electrical properties and luminous efficiency of OLEDs because the device structure was similar to that of recent work reported by A. Kuruvila et al. which showed high luminous efficiency [88]. Therefore, smooth surface and low  $R_{sh}$  of graphene electrode are crucial prerequisites for practical application of graphene.

Effective surface modification of graphene was firstly achieved by using multi-layered graphene formed by stacking of CVD-grown SLGs [12]. To form high-quality and large-area multilayered graphene films, SLG was grown by CVD using Cu foil as a catalyst, then repeatedly transferred to polyethylene terephthalate (PET)

substrate. Chemical p-type dopants ( $HNO_3$ ,  $AuCl_3$ ) were used to decrease the  $R_{sh}$  of pristine graphene. Four-layered p-doped graphene film had greatly reduced  $R_{sh}$  ~34  $\Omega$ /sq, which is comparable to that of conventional ITO. To reduce the large hole-injection energy barrier between low-WF graphene anode and organic HTL (HOMO energy level ~5.4 eV), we also used a self-organized polymeric interfacial layer on top of the graphene anode. The polymer composition HIL (GraHIL) which consists of PEDOT: PSS and tetrafluoroethylene-perfluoro-3,6-dioxa-4-methyl-7-octenesulfonic acid copolymer (PFI) develops a gradually-increasing ionization potential from the bottom to the top surface, and the surface WF of the film reaches ~5.95 eV (Fig. 9a). When pristine graphene was modified with chemical dopant and GraHIL to have high electrical conductivity and high WF, Ohmic contact formed between graphene and organic HIL, which was demonstrated by using dark-injection space-charge-limited-current measurement. Due to the chemical inertness of graphene, a surface-modified graphene anode could provide higher chemical stability and superior hole injection than those of ITO anode. ITO can be easily etched by acidic polymer dispersion (e.g., PEDOT:PSS) during solution processing, and released metal (In and Sn) species can diffuse into organic films of OLEDs and form charge trapping sites and exciton quenching (or non-radiative recombination) centers that degrade charge injection and transport, and electroluminescent efficiency of OLEDs [44,46]. As a result, flexible phosphorescent OLEDs with the modified graphene anode had significantly

higher luminous efficiencies ( $\sim 98.1 \text{ cd/A}$ ,  $102.7 \text{ lm/W}$ ) than those of ITO anode ( $\sim 81.8 \text{ cd/A}$ ,  $85.60 \text{ lm/W}$ ) (Fig. 9b). Furthermore, graphene-based flexible solid-state lighting devices using fluorescent white OLEDs were fabricated to show a potential application of this graphene electrode (Fig. 9c). This work demonstrated a crucial role of surface modification methods for high electrical conductivity and work function, and that flexible OLEDs using modified graphene anode can compete with devices that use conventional ITO anode. Similar strategy using chemical p-type dopant and interfacial layer to overcome large hole injection energy barrier have also been used to develop efficient flexible OLEDs using CVD-grown SLG anode [89]. Triethyloxonium hexachloroantimonate (OA) which can form charge transfer complex with graphene, was used as chemical p-type dopant; it reduced  $R_{sh}$  of the SLG to  $>200 \Omega/\text{sq}$ . PEDOT:PSS and transition metal oxide ( $\text{MoO}_3$ ) were also used as an interfacial layer on top of the graphene to achieve direct hole injection from graphene anode; because  $\text{MoO}_3$  has very deep LUMO energy level  $\sim 6.7 \text{ eV}$ , holes can be directly injected from OA-doped graphene/PEDOT:PSS into the organic HTL (i.e., 4,40-bis(carbazol-9-yl)biphenyl (CBP)) through the thin  $\text{MoO}_3$  layer (Fig. 10a). By surface modification of pristine graphene, green phosphorescent OLEDs [graphene anode/PEDOT:PSS/ $\text{MoO}_3/\text{MoO}_3$  doped CBP/CBP:Ir(ppy)<sub>2</sub>(acac)/TPBI/LiF/Al] showed high external quantum efficiency (EQE)  $> 20\%$ , which corresponds to  $\sim 80 \text{ cd/A}$  despite the use of only SLG in the OLEDs (Fig. 10b); it also demonstrated the importance of effective modification for graphene-based flexible OLEDs.

A surface modification method using transition metal oxide has been newly proposed to p-dope graphene and reduce the energy barrier for hole injection on graphene anode at the same time [90]. A thin  $\text{MoO}_3$  layer functions as a charge-transfer p-type dopant, which increases WF of graphene by  $\sim 0.25 \text{ eV}$  and reduces  $R_{sh}$  of few-layered CVD-grown graphene to  $<50 \Omega/\text{sq}$ . Furthermore, 5-nm-thick  $\text{MoO}_3$  on the graphene formed a large interface dipole that caused a downward shift of  $\sim 1.9 \text{ eV}$  in the vacuum level, so the energy levels of the graphene anode and the overlying organic HTL (i.e., CBP) match well (Fig. 10c). Phosphorescent green OLEDs with a tri-layered graphene anode modified with transition metal oxide ( $\sim 70 \Omega/\text{sq}$ ) [anode/ $\text{MoO}_3/\text{MoO}_3:\text{CBP}/\text{CBP}/\text{CBP}:\text{Ir}(\text{ppy})_3/\text{TPBI}:\text{Ir}(\text{ppy})_3/\text{TPBI}/\text{LiF}/\text{Al}$ ] showed better luminous efficiencies ( $\sim 60 \text{ cd/A}$ ,  $45 \text{ lm/W}$ ) than those with ITO anode (Fig. 10d). Also, various kinds of transition metal oxides including  $\text{WO}_3$  and  $\text{V}_2\text{O}_5$  can be used in the same way [88]. Deposition of a thin  $\text{WO}_3$  or  $\text{V}_2\text{O}_5$  layer also provides p-type charge-transfer doping and efficient energy level alignment for graphene anode at the same time. As a result, SLG modified with a thin transition metal oxide layer showed  $\sim 50\%$  reduction in  $R_{sh}$  to  $\sim 300 \Omega/\text{sq}$ , and phosphorescent OLEDs using 5-nm-thick  $\text{WO}_3$  or  $\text{V}_2\text{O}_5$  on top of graphene [graphene/transition metal oxide/CBP: $\text{MoO}_3/\text{CBP}/\text{CBP}:\text{Ir}(\text{ppy})_3/\text{TPBI}/\text{LiF}/\text{Al}$ ] had  $\sim 75 \text{ lm/W}$  and  $95 \text{ lm/W}$ , respectively. Because the transition metal oxides can be used as a p-type dopant that reduces high  $R_{sh}$  and alignment of energy level for favorable hole injection from graphene anode, it can be a good option to obtain an air-stable modified graphene anode. However, the rough surface morphology and noticeable

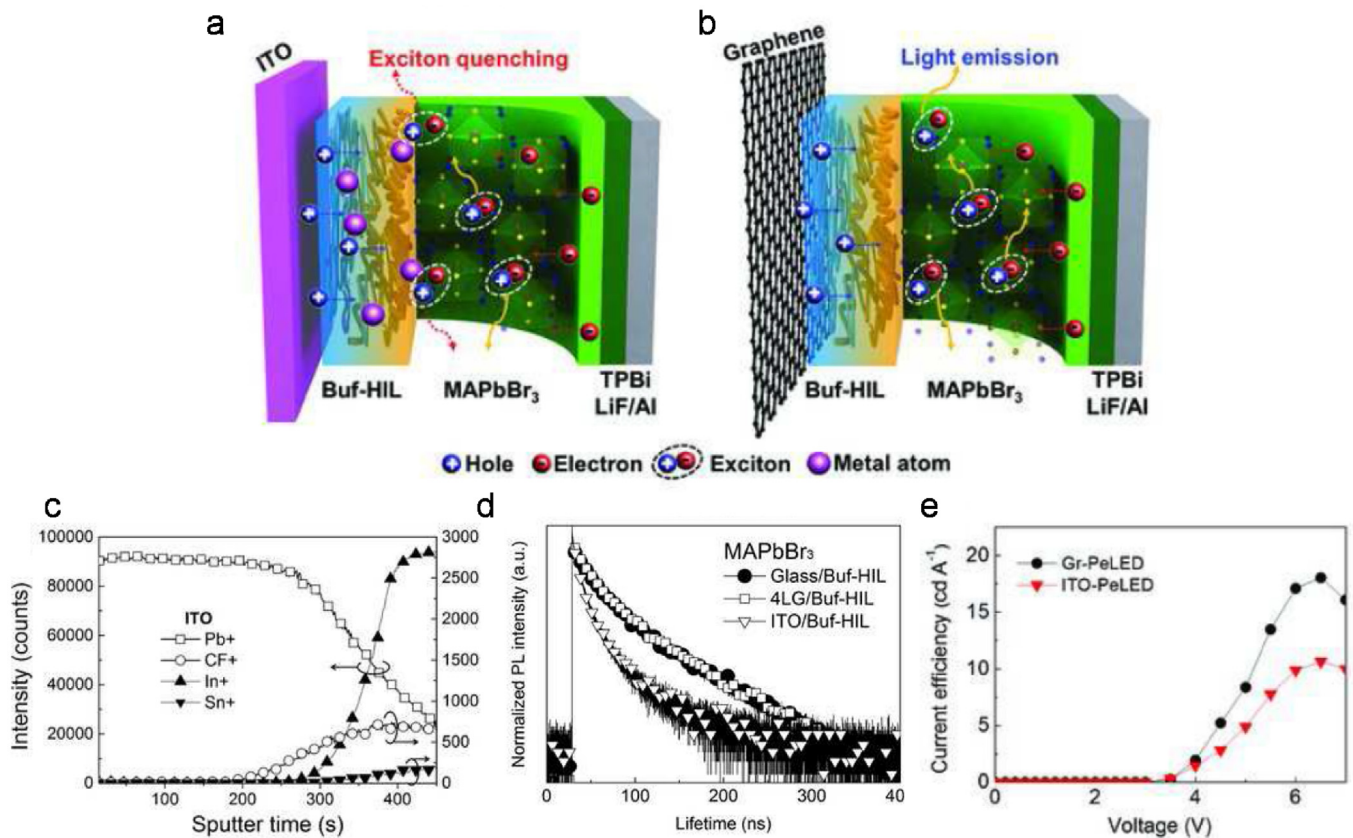


**Fig. 11.** Schematic illustrations of (a) exciton quenching by In and Sn, and (b) blocking of exciton quenching in graphene based LEDs, (c) Depth profile of  $\text{In}^+$  and  $\text{Sn}^+$  in  $\text{MAPbBr}_3$ /polymeric HIL measured by SIMS, (d) Electroluminescent spectra of PeLEDs with graphene and ITO anode, (e) Time-resolved photoluminescence of  $\text{MAPbBr}_3$  on Glass/HIL, four-layered graphene/HIL, and ITO/HIL, where  $\text{Pb}^+$  and  $\text{CF}^+$  represent  $\text{MAPbBr}_3$  and perfluorinated ionomer in polymeric HIL, respectively, (f) Current efficiency of perovskite LEDs with graphene and ITO anode. Reproduced from [91] Copyright 2017, Wiley-VCH.

**Table 1**  
Chemical structure and p-type doping effect depending on p-type chemical dopant materials.

Dopant	Chemical structure	Graphene	R <sub>sh</sub> <sup>a</sup> [Ω/sq]	WF <sup>b</sup> [eV]	Raman shift [cm <sup>-1</sup> ]	Charge concentration [cm <sup>-2</sup> ]	Ref.
Nitric acid		Four-layered CVD-grown (Cu) graphene	212 to 84	4.4 to 4.61	G:1592 to 1596 2D:2679 to 2685	–	[48]
Gold chloride	AuCl <sub>3</sub>	Four-layered CVD-grown (Cu) graphene	87 to 34	4.4 to 5.07	–	–	[12]
Gold chloride	AuCl <sub>3</sub>	Multilayered rapid thermal CVD-grown (Ni) graphene	201 to 149	4.5 to 4.8	G:1589 to 1594	2.4 × 10 <sup>13</sup>	[64]
Iridium chloride	IrCl <sub>3</sub>	Few layered CVD-grown (Cu) graphene	600	4.2 to 4.7	G: +12.5	–	[102]
Molybdenum chloride	MoCl <sub>3</sub>	Few layered CVD-grown (Cu) graphene	720	4.2 to 4.6	G: +6.5	–	[102]
Osmium chloride	OsCl <sub>3</sub>	Few layered CVD-grown (Cu) graphene	700	4.2 to 4.5	G: +5.4	–	[102]
Palladium chloride	PdCl <sub>2</sub>	Few layered CVD-grown (Cu) graphene	520	4.2 to 4.7	G: +8.2	–	[102]
Rhodium chloride	RhCl <sub>3</sub>	Few layered CVD-grown (Cu) graphene	620	~4.2 to ~5.14	G: +7.1	–	[102]
Triethyloxonium hexachloroantimonate (OA)	Et <sub>3</sub> O <sup>+</sup> SbCl <sub>6</sub> <sup>-</sup>	Single-layer CVD-grown (Cu) graphene	~1000 to <200	4.7 to 5.1	G:1591 to 1608 2D:2680 to 2697	2 × 10 <sup>13</sup>	[89].
Molybdenum trioxide	MoO <sub>3</sub>	Few layered CVD-grown (Cu) graphene	<50	increase by ~0.25	–	–	[90]
Tungsten trioxide	WO <sub>3</sub>	Single-layer CVD-grown (Cu) graphene	<300	increase by ~0.2	–	–	[103]
9,10-dibromoanthracene (An-Br)		Mechanically exfoliated graphene	–	–	G: upshift 2D: upshift	–	[104]
Tetracyanoquinodimethane (TCNQ)		Few layered CVD-grown (Cu) graphene	850 to 140	5.0 to 5.2	G: +6 2D: +6.1	2.3 × 10 <sup>13</sup>	[105]
Tetrafluoro-tetracyanoquinodimethane (F4-TCNQ)		Epitaxial graphene on 6H-SiC	–	increase by ~1.3	–	–	[106]
2,3-Dichloro-5,6-dicyanobenzoquinone (DDQ)		Multilayered rapid thermal CVD-grown (Ni) graphene	201 to 190	4.5 to 4.7	G:1589 to 1591	2.0 × 10 <sup>13</sup>	[64]
tetrasodium 1,3,6,8-pyrenetetrasulfonic acid (TPA)		Mechanically exfoliated graphene	–	–	G: upshift 2D: upshift	–	[104]
Bis(trifluoromethanesulfonyl) amide (TFSA)		Five-layered CVD-grown (Cu) graphene	240 to 90	4.4 to 5.1	G: 1588 to 1611 2D: 2676 to 2692	9.9 × 10 <sup>13</sup>	[81,101]
Trifluoromethane sulfonic acid (TFMS)		Four-layered CVD-grown (Cu) graphene	212 to 63	4.4 to 5.23	G: 1572 to 1610 2D: 2676 to 2692	–	[48]

<sup>a</sup> R<sub>sh</sub>: sheet resistance.<sup>b</sup> WF: work function.

decrease in  $T$  caused by deposition of transition metal oxides on graphene must be solved to enable practical applications of graphene anode.

### 3.3.2. Organic-inorganic hybrid perovskite LEDs

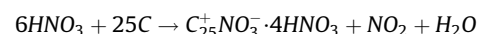
Surface-modified graphene has also been used as the anode in flexible organic-inorganic hybrid perovskite LEDs (PeLEDs) [91]. PeLEDs have high color purity, low fabrication cost, and easily-tunable color. However, organic/inorganic hybrid perovskite intrinsically has small exciton binding energy  $<100$  meV and long exciton diffusion length  $>1\text{ }\mu\text{m}$ , so excitons can be easily dissociated; as a result, electroluminescence (EL) is very weak at room temperature [92–97]. Especially, metal species that have diffused from the ITO anode into the organic layer severely influence excitons formed in the perovskite emitter due to its long exciton diffusion length. In contrast, the graphene anode is chemically inert and therefore does not release any species that can act as exciton quenchers or non-radiative recombination centers; therefore, graphene anodes can increase the EL of organic/inorganic hybrid perovskite substantially (Fig. 11a,b). Four-layer graphene grown by CVD with Cu catalyst was used as a flexible anode, and successively p-type doped with  $\text{HNO}_3$  to reduce  $R_{sh}$  of pristine graphene to  $\sim 84.2\text{ }\Omega/\text{sq}$ . A self-organized polymeric HIL that had high surface-ionization potential  $\sim 6.0\text{ eV}$  was also used to minimize the energy barrier to hole injection from the graphene anode ( $\sim 4.4\text{ eV}$ ) to the perovskite emitting layer that has deep valance-band maximum  $\sim 5.9\text{ eV}$  [4LG/HIL/MAPbBr<sub>3</sub>/2,2'-(1,3,5-benzenetriyl)-tris(1-phenyl-1-H-benzimidazole (TPBi)/LiF/Al]. Metal (In and Sn) species diffused to the perovskite emitting layer through the polymeric layer from ITO anode, which was investigated by time-of-flight secondary ion mass spectrometry (Fig. 11c). Metal species that diffuse into the perovskite emitting

layer clearly form exciton quenching sites or non-radiative recombination centers: PL exciton lifetime was longer in the film with the chemically-inert graphene anode than in the ITO anode (Fig. 11d). As a result, graphene-based flexible perovskite LED showed maximum current efficiency  $\sim 18.0\text{ cd/A}$ , which was much higher than that with ITO anode ( $\sim 10.6\text{ cd/A}$ ) (Fig. 11e). This work shows obvious advantage of chemically inert graphene electrode in perovskite LEDs.

### 3.4. Air-stability for graphene

The shortcomings of pristine graphene such as low electrical conductivity and low WF can be solved by using graphene doping or interfacial layers (Section 3.3), but in ambient condition  $R_{sh}$  of graphene doped by volatile chemical dopants gradually increases over time. Production of flexible electronics will not be practical until this problem is solved [48,56,81,82]. Therefore, the doping stability of graphene in ambient condition is also an essential requirement.

Many p-type dopant materials have been used to reduce  $R_{sh}$  and increase WF, and their chemical structures and doping effects are summarized in Table 1.  $\text{HNO}_3$  is widely used as a p-type dopant for graphitic materials such as graphite, carbon nanotubes and graphene.  $\text{HNO}_3$  forms a charge-transfer complex with carbon materials by withdrawing electrons from graphene according to the reaction [98]:



By forming a charge transfer complex with graphene, doping with  $\text{HNO}_3$  increases carrier concentration in graphene and reduces  $R_{sh}$  of graphene. However, this inorganic molecular dopant tends to gradually increase  $R_{sh}$  of  $\text{HNO}_3$ -doped graphene because

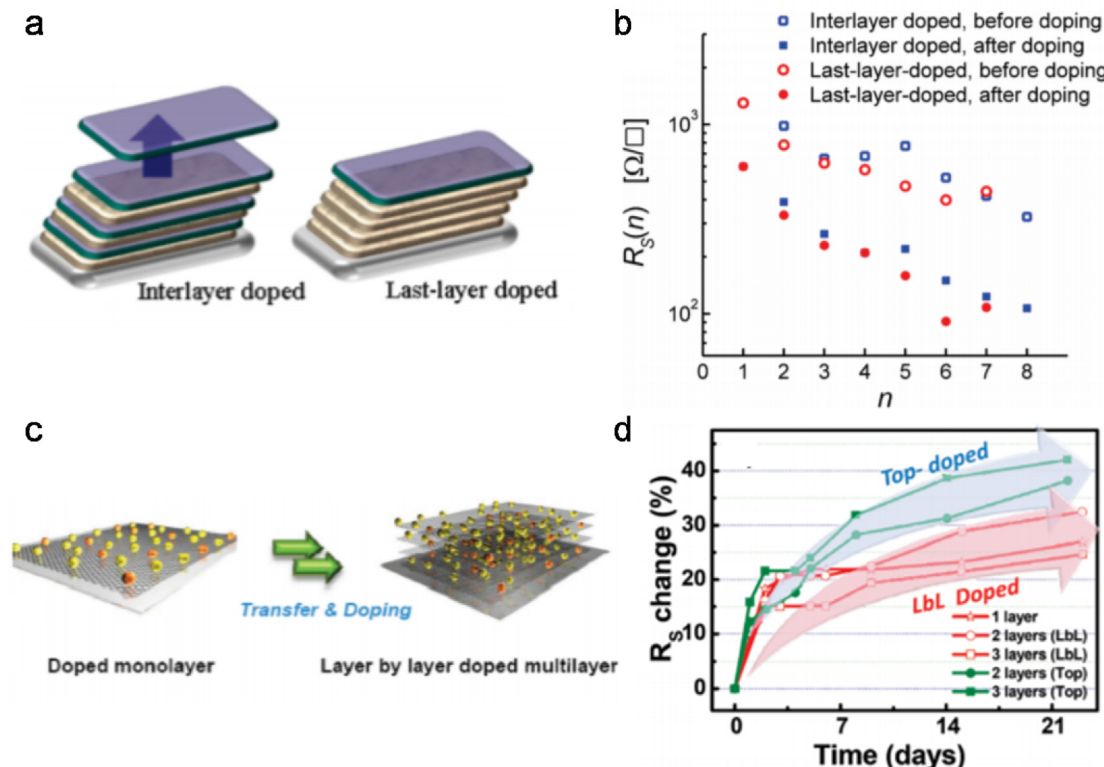


**Fig. 12.** (a) Schematic illustration of interlayer doping and last-layer doping with nitric acid for multilayered graphene, (b) Sheet resistance as a function of the number of graphene layers for interlayer doping and last-layer doping. Reproduced from [82] Copyright 2010, American Chemical Society, (c) Schematic illustration of layer-by-layer doping with gold chloride for multilayered graphene, (d) Sheet resistance change as a function of time for layer-by-layer doping and top-layer doping. Reproduced from [56] Copyright 2010, American Chemical Society.

highly-volatile  $\text{HNO}_3$  evaporates in ambient condition. Layer-by-layer doping methods for multilayered graphene films have been tried to improve doping stability of conventionally-used inorganic p-type dopants such as  $\text{HNO}_3$  and  $\text{AuCl}_3$  in ambient condition [56,82]. CVD-grown SLGs were repeatedly doped after each SLG layer was stacked (i.e., interlayer doping), but it showed only slight change of electrical conductivity in eight-layered graphene film  $\sim 90 \Omega/\text{sq}$ , which is similar to that with conventional  $\text{HNO}_3$  doping (i.e., last-layer doping) (Fig. 12a, b); these results can attribute to intercalation of  $\text{HNO}_3$  in graphene layers into the graphene stacks

during last-layer doping of multilayered graphene, and volatile  $\text{HNO}_3$  could already evaporate before stacking of next layer [82].

$\text{AuCl}_3$  is an effective p-type dopant for a graphene, but is also unstable in ambient conditions. Layer-by-layer doping of multilayered graphene using  $\text{AuCl}_3$  to improve environmental doping stability has also been tested [56]. Stacked four-layered CVD-grown graphene film doped with layer-by-layer method showed significant reduction of  $R_{sh}$  from  $\sim 313 \Omega/\text{sq}$  to  $58 \Omega/\text{sq}$ , but the final resistance was not noticeably different from that obtained using last-layer doping ( $\sim 68 \Omega/\text{sq}$ ).  $\text{AuCl}_3$  dissolved in a solvent

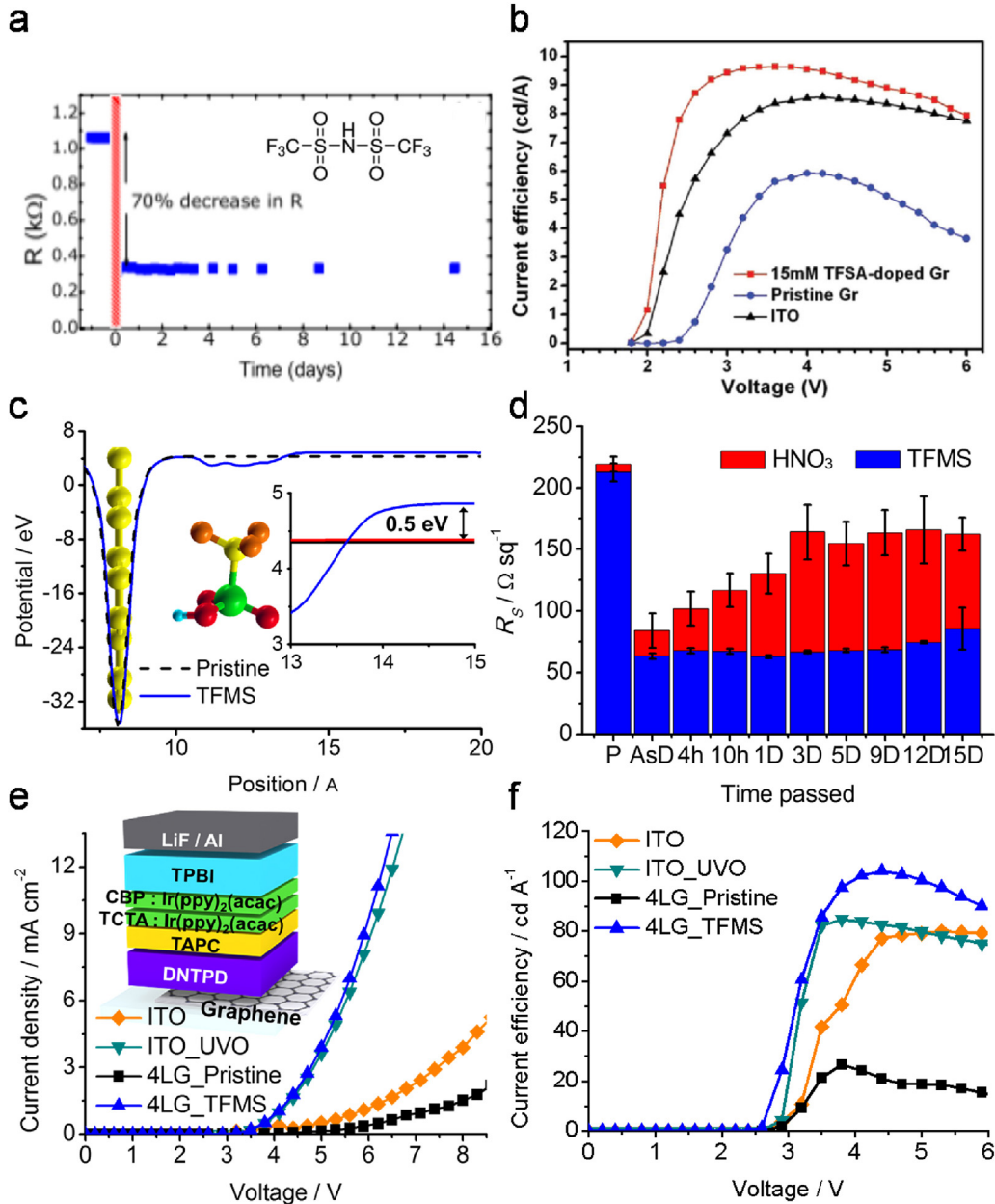
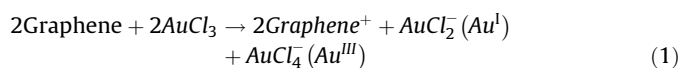


**Fig. 13.** (a) Change in resistance of TFSA-doped graphene as a function of time (inset: molecular structure of TFSA). Reproduced from [81] Copyright 2011, IOP Publishing, (b) Current efficiency of polymer LEDs with TFSA-doped, pristine five-layered graphene, and ITO anode. Reproduced from [101] Copyright 2013, Wiley-VCH, (c) Planar average of electrostatic potential and the most stable adsorption position of TFMS-doped graphene, (d) Change in sheet resistance of TFMS-doped and  $\text{HNO}_3$ -doped graphene over time, (e) Current density, (f) Current efficiency of green phosphorescent OLEDs with ITO, ultra-violet ozone surface-treated ITO, pristine graphene, and TFMS-doped graphene. Reproduced from [48] Copyright 2016, Wiley-VCH.

such as nitromethane, which a poor coordinating solvent, would withdraw electrons from graphene according to following reactions [67,99]:



During these reactions,  $\text{Au}^{III}$  is reduced to  $\text{Au}^I$ , then uncoordinated  $\text{Au}^I$  forms  $\text{Au}^0$ ,  $\text{AuCl}^{III}$ , and  $\text{Cl}^-$ . In the presences of excess  $\text{AuCl}_3$ ,  $\text{Cl}^-$  coordinates according to the reaction:



Two possibilities may explain the increase in  $R_{sh}$  of  $\text{AuCl}_3$ -doped graphene in ambient condition: evaporation of volatile solvent that

has p-doping effect itself, and the hygroscopic nature of  $\text{Cl}^-$  [67,100]. Although the layer-by-layer doping method using  $\text{AuCl}_3$  reduced the change in  $R_{sh}$  of doped multilayered graphene in ambient condition,  $R_{sh}$  still gradually increased over time (Fig. 12c, d). Therefore, practical production of graphene electrode requires development of novel air-stable doping methods that do not use conventional volatile chemical dopants. Additionally, high electrical conductivity and high WF given by single chemical doping are sought as ideal requirements for graphene anode.

S. Tongay et al. reported air-stable p-type chemical doping using bis(trifluoromethanesulfonyl) amide (TFSA,  $[\text{CF}_3\text{SO}_2]_2\text{NH}$ ), which is also used to p-dope carbon nanotubes [81]. The TFSA is an electron-acceptor due to electronegative elements in the molecule, so TFSA showed a p-type doping effect on pristine graphene. This doping method reduced  $R_{sh}$  of SLG by ~70% (to ~129  $\Omega/\text{sq}$ ), but only decreased  $T$  by ~3% (Fig. 13a). TFSA includes hydrophobic

**Table 2**

Chemical structure and n-type doping effect depending on n-type chemical dopant materials.

Dopant	Chemical structure	Graphene	$R_{sh}^a$ [ $\Omega/\text{sq}$ ]	WF <sup>b</sup> [eV]	Raman shift [cm <sup>-1</sup> ]	Dirac Point shift [V]	Charge concentration [cm <sup>-2</sup> ]	Ref.
Hydrazine		Single-layer CVD-grown (Cu) graphene	–	4.27	G: 1581 to 1577 2D: 2664 to 2679	50 to -55	–	[111]
4-(2,3-Dihydro-1,3-dimethyl-1H-benzimidazol-2-yl)-N,N-dimethylbenzenamine (N-DMBI)		Single- and double-layer CVD-grown (Cu) graphene	–	decrease by ~0.2	2D: 2687 to 2682	95 to -140	–	[62]
Decamethylcobaltocene (DMC)		Single- and double-layer CVD-grown (Cu) graphene	–	4.3 to 3.53	G shift: 5 2D shift: -6	–	–	[61]
1,5-naphthalenediamine (Na-NH <sub>2</sub> )		Mechanically exfoliated graphene	–	–	G: downshift 2D: upshift	-98	–	[104]
9,10-dimethylanthracene (An-CH <sub>3</sub> )		Mechanically exfoliated graphene	–	–	G: downshift 2D: upshift	-20	–	[104]
ethylene diamine (EDA)		Single-layer CVD-grown (Cu) graphene	–	–	G: 1589 to 1590	1.4 to -126	$9 \times 10^{12}$	[112]
diethylene triamine (DETA)		Single-layer CVD-grown (Cu) graphene	–	–	G: 1589 to 1593.	1.4 to -166	$1.2 \times 10^{13}$	[112]
triethylene tetramine (TETA)		Single-layer CVD-grown (Cu) graphene	98	–	G: 1589 to 1596	1.4 to -192	$1.4 \times 10^{13}$	[112]
1,1' dibenzyl-4,4'-bipyridinium dichloride (BV)		Multilayered rapid thermal CVD-grown (Ni) graphene	260	4.5 to 4.0	G: 1589 to 1587	–	$2.1 \times 10^{13}$	[64]
Titanium suboxide	$\text{TiO}_x$	Single-layer CVD-grown (Cu) graphene	–	4.68 to 4.33	2D: 2644 to 2632	10 to -76	–	[121]
Cesium carbonate	$\text{Cs}_2\text{CO}_3$	Single-layer CVD-grown (Cu) graphene	~1300 to ~250	4.6 to 3.6	G shift: 18	–	$2.2 \times 10^{13}$	[115]
Zinc oxide	$\text{ZnO}$	Three-layered CVD-grown (Cu) graphene	–	–	G: 1584 to 1593	50 to -60	–	[72]

<sup>a</sup>  $R_{sh}$ : sheet resistance.

<sup>b</sup> WF: work function.

fluoromethane, and therefore maintains doping stability for a long time in ambient condition; e.g., the reduced  $R_{sh}$  of TFSA-doped graphene has been maintained for more than two weeks in air [81]. D. Kim et al. used TFSA to p-dope the graphene anode for polymer LEDs [101]; TFSA was spin-coated on a five-layered graphene anode formed by stacking SLGs grown by CVD; this process reduced  $R_{sh}$  to  $\sim 90 \Omega/\text{sq}$  and retained  $T \sim 88\%$ . PLEDs with TFSA-doped graphene anode showed lower operating voltage and higher luminous efficiencies ( $\sim 9.6 \text{ cd}/\text{A}$ ,  $10.5 \text{ lm}/\text{W}$ ) than those with pristine graphene ( $\sim 5.9 \text{ cd}/\text{A}$ ,  $5.2 \text{ lm}/\text{W}$ ); this difference can attribute to reduced  $R_{sh}$  and the increased WF of TFSA-doped graphene (Fig. 13b). Trifluoromethanesulfonic acid (TFMS,  $\text{CF}_3\text{SO}_3\text{H}$ ) is a strong monoprotic organic acid; T.-H. Han et al. reported air-stable p-type chemical dopant that hugely improves electrical conductivity, WF, and air-stability of graphene at the same time (Fig. 13c) [48]. Solution-processed doping using TFMS greatly reduced  $R_{sh}$  of four-layered graphene by  $\sim 70\%$  to  $\sim 63 \Omega/\text{sq}$ , and increased its WF by  $\sim 0.83 \text{ eV}$ ; in contrast, doping with conventional inorganic acid (i.e.,  $\text{HNO}_3$ ) decreased graphene's  $R_{sh}$  by  $\sim 63\%$  to  $\sim 84 \Omega/\text{sq}$  and increased its WF by only  $\sim 0.21 \text{ eV}$ . TFMS-

doped graphene has maintained its reduced  $R_{sh}$  for more than two weeks in ambient condition (Fig. 13d). In contrast,  $\text{HNO}_3$ -doped graphene showed steep increase in  $R_{sh}$  within 3 d. The non-planar configuration of TFMS enables its acidic proton to bind closely and tightly to graphene with higher binding energy ( $\sim -0.5 \text{ eV}$ ) than that of  $\text{HNO}_3$  ( $\sim -0.3 \text{ eV}$ ), and thereby to increase the p-type doping effect and air-stability of TFMS-doped graphene (Fig. 13c) compared to that of (planar)  $\text{HNO}_3$ . TFMS-doped graphene with increased electrical conductivity ( $\sim 63 \Omega/\text{sq}$ ) and WF ( $\sim 5.23 \text{ eV}$ ) was used to fabricate phosphorescent OLEDs that did not include a specially-developed HIL [anode/N,N'-diphenyl-N,N'-bis-{4-(phenyl-m-tolyl-amino)-phenyl}-biphenyl-4,4'-diamine (DNTPD)/TAPC/TCTA:Ir(ppy)<sub>2</sub>(acac)/CBP:Ir(ppy)<sub>2</sub>(acac)/TPBI/LiF/Al]. This OLED had higher luminous efficiencies ( $\sim 104.1 \text{ cd}/\text{A}$ ,  $80.7 \text{ lm}/\text{W}$ ) and lower operating voltage than those with ITO ( $\sim 84.8 \text{ cd}/\text{A}$ ,  $73.8 \text{ lm}/\text{W}$ ) (Fig. 13e,f). These studies have demonstrated that chemical dopants such as TFSA and TFMS which give stronger binding with graphene and hydrophobic nature provide not only improved electrical conductivity, WF, but also doping stability in ambient conditions.

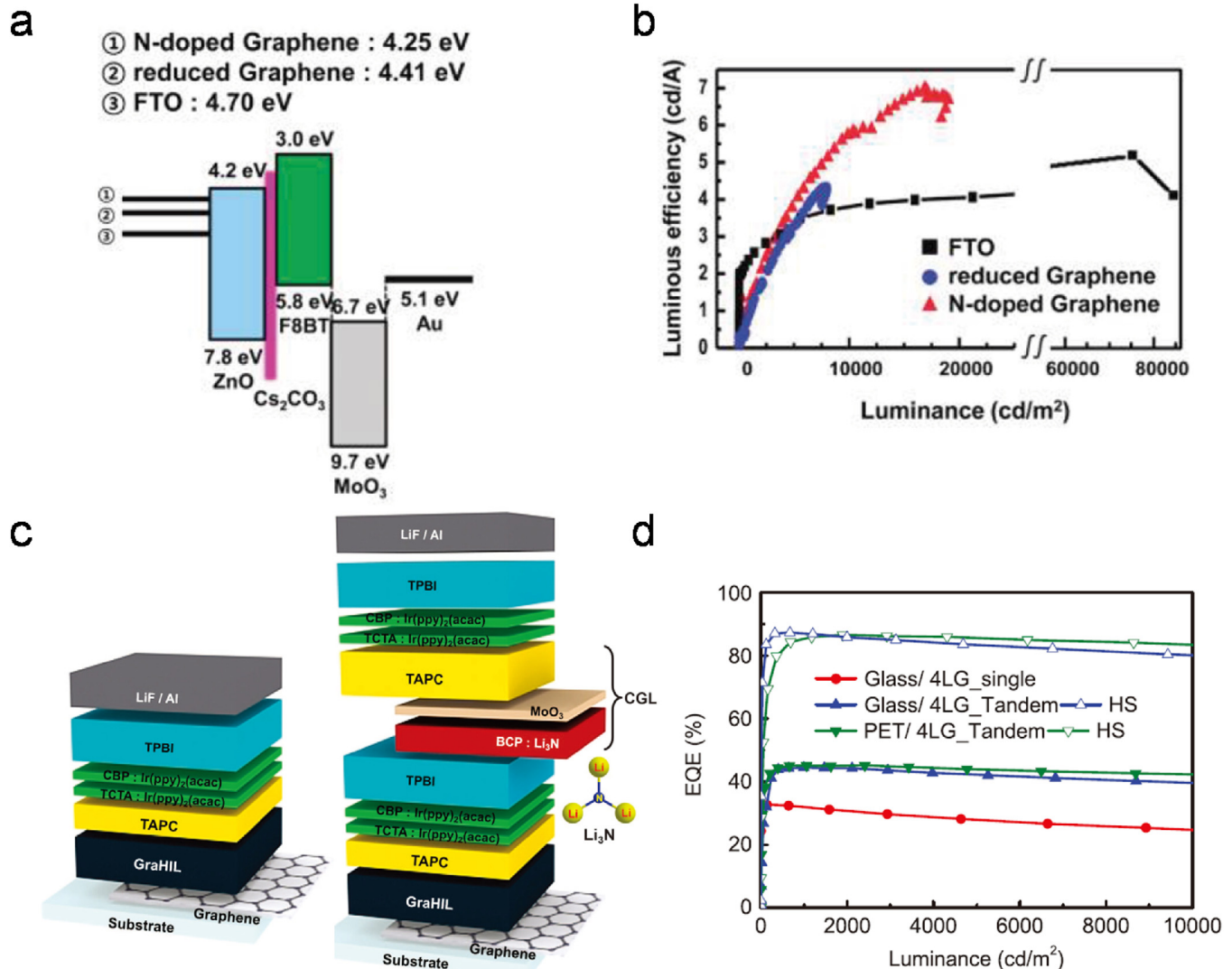


**Fig. 14.** (a) Energy level diagram, and (b) Luminous current efficiency of inverted polymer LEDs with n-doped graphene, reduced graphene, and FTO cathode. Reproduced from [114] Copyright 2012, American Chemical Society (c) Device architecture of standard single and tandem green phosphorescent OLEDs on graphene anode, (d) External quantum efficiencies of single and tandem OLEDs with four-layered graphene anode Reproduced from [79] Copyright 2016, Nature Publishing Group.

### 3.5. Device architectures of OLEDs on graphene

Standard structured OLEDs generally include low-WF metal such as Ca, Ba, or its derivatives such as LiF under a metal cathode. These materials are easily oxidized, and their devices can be chemically unstable in air. Inverted structured OLEDs generally use a metal oxide electron injection or transporting layer (e.g., ZnO, TiO<sub>2</sub>) instead of low-WF metals [107]. Therefore, inverted OLEDs have been developed to improve operational stability of OLEDs. Inverted OLEDs also can be fabricated using graphene as a cathode. To use graphene as a cathode, the graphene must be n-doped to reduce the energy barrier to electron injection into LUMO energy level of the overlying electron-transport layer (ETL).

Various kinds of n-type dopant materials and their doping methods have been developed to control electrical and electronic properties of pristine graphene (Table 2) [61,62,64,104,108–111]. n-Type dopant materials donate electrons to graphene. When ionization potential of dopant is higher than Fermi energy level of graphene, electrons are spontaneously transferred to graphene [57,62,63,108,109]. Also, when dopant material that has low (more negative) reduction potential (i.e., tendency to lose electron) is adsorbed on graphene, dopant is oxidized by reducing graphene [57,64]. Inorganic hydrazine (N<sub>2</sub>H<sub>4</sub>) have been widely used for reduction of GO and n-type dopant for graphene [110,111]. In

hydrazine, NH<sub>2</sub> which is an electron-donating group causes it to bond to graphene; the result is an increase in electron density (n-type doping). In addition, hydrazine introduces nitrogen atoms into graphene; this process can also increase the number of free-electron charge carriers [111]. 4-(1,3-dimethyl-2,3-dihydro-1H –benzimidazol-2-yl (N-DMBI) is an effective n-type dopant for graphene [62,108,109]. Thermal annealing makes N-DMBI release hydrogen atoms and become radical. The radical has very high singly-occupied molecular orbital (SOMO) of –2.36 eV, and thus donates electrons to graphene to yield strong n-type doping [62,108,109]. Similarly, metallocenes that have low ionization energy can be effective n-type dopants for graphene. Decamethylcobaltocene (DMC) has a low ionization energy of 3.3 eV and rich π-electrons that can stably interact with the graphene lattice. Therefore, DMC gives strong n-type doping effect on graphene due to easy electron transfer from DMC to graphene [61]. Aromatic molecules such as 1,5-naphthalenediamine (Na-NH<sub>2</sub>) and 9,10-dimethylnanthracene (An-CH<sub>3</sub>) can also give stable binding by strong π – π interactions of aromatic rings between dopant materials and graphene, and an electron donating group in dopant materials increases electron density in graphene (i.e., n-type doping) [104]. Ethylene amines also act as n-type dopant materials for graphene, and n-type doping of graphene depends on the number of amines because the amine functional group is an

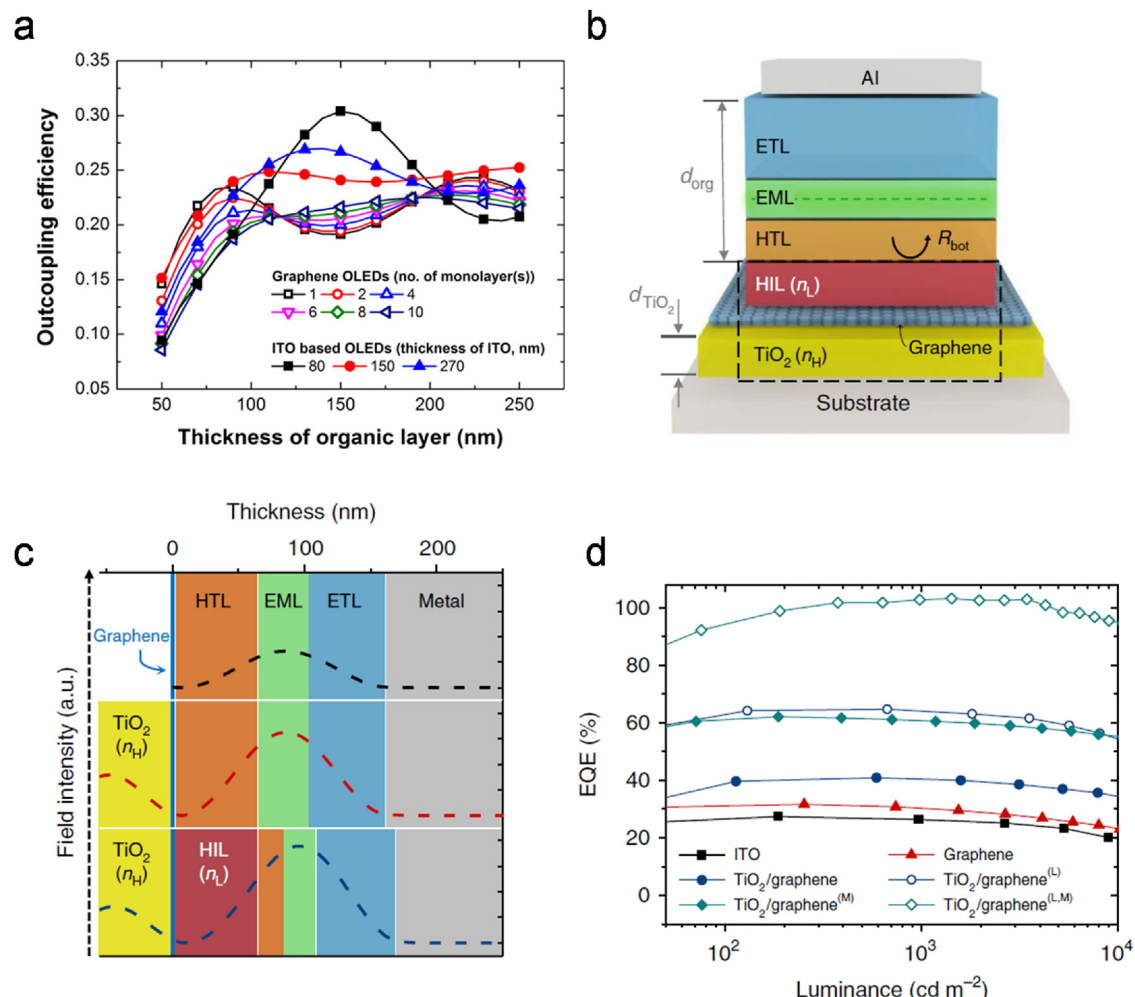


**Fig. 15.** (a) Calculated optical out-coupling efficiencies of OLEDs with graphene and ITO anode. Reproduced from [94] Copyright 2012, Elsevier, (b) Device structure of flexible electrode architecture sandwiching graphene with high-refractive-index TiO<sub>2</sub> and low-refractive-index HIL, (c) Electromagnetic field intensity according to electrode architectures, (d) External quantum efficiency of green phosphorescent OLEDs with graphene, TiO<sub>2</sub>/graphene, and ITO anode (L: hemispherical lens, M: multi-junction device). Reproduced from [80] Copyright 2016, Nature Publishing Group.

electron donor: the amount of electrons donated from dopant molecules increases according in the order ethylene diamine (EDA) < diethylene triamine (DETA) < triethylene tetramine (TETA) [112].

The reduction potential of dopant materials is an important parameter for determining doping type and doping concentration of graphene [64]. 1,1'dibenzyl-4,4'-bipyridinium dichloride (BV) has negative reduction potential ( $-1.12\text{ V}$ ) while p-type dopant has positive reduction potential (e.g.,  $\text{AuCl}_3$ :  $1.51\text{ V}$  [113]), and thus reduction from  $\text{BV}^{2+}$  to  $\text{BV}^0$  is not spontaneous reaction. Therefore,  $\text{BV}^0$  can be used to n-dope graphene.  $\text{BV}^0$  is stabilized by donating electrons to graphene, so electron density in graphene increases. [64] Various kinds of n-type dopant materials and their n-type doping effects are summarized in Table 2.

J. O. Hwang et al. used chemically- and thermally n-doped rGO film as a transparent cathode in inverted polymer LEDs [114]. GO solution was produced using a modified Hummers method, spin-coated on substrate, chemically reduced by exposure to  $\text{N}_2\text{H}_4$  vapor, then thermally annealed at  $750^\circ\text{C}$  in  $\text{H}_2/\text{NH}_3$  gas mixture. A 4-nm-thick n-doped rGO film showed reduced  $R_{sh} \sim 300\ \Omega/\text{sq}$  and  $WF \sim 4.25\text{ eV}$  at  $T = 80\%$  (Fig. 14a). An inverted polymer LED that used the n-doped rGO cathode [graphene/ZnO/Cs<sub>2</sub>CO<sub>3</sub>/F8BT/MoO<sub>3</sub>/Au] also showed lower operating voltage and higher current efficiency ( $\sim 7.0\text{ cd/A}$ ) than did conventional rGO ( $\sim 4.0\text{ eV}$ ) (Fig. 14b). Cesium carbonate (Cs<sub>2</sub>CO<sub>3</sub>) was used to enable effective

charge-transfer n-type doping of graphene for cathode application [115]. n-Type doping of graphene is caused by large  $WF$  difference between alkali metal and graphene. Cs<sub>2</sub>CO<sub>3</sub> is thermally decomposed into metallic Cs during thermal evaporation; as a result, Cs atoms adsorb to graphene. Cs has a much lower  $WF \sim 1.8\text{ eV}$  than does graphene, so electron transfer is effective. [116,117] C. Hartwigsen et al. also identified that 6s electrons in the Cs atom are transferred to  $\pi^*$  states of graphite in study on alkali-graphite intercalation. [118] To increase doping stability, highly-reactive Cs<sub>2</sub>CO<sub>3</sub> was embedded in the organic matrix of the electron-transporting material (bathophenanthroline (Bphen)) on the graphene. When Bphen: Cs<sub>2</sub>CO<sub>3</sub> was co-evaporated on SLG,  $R_{sh}$  and  $WF$  were reduced to  $250\ \Omega/\text{sq}$  and  $\sim 3.6\text{ eV}$  respectively; these changes facilitated electron injection from the graphene cathode into the overlying ETL. Because of the reduced  $R_{sh}$  and  $WF$  of n-doped graphene, inverted phosphorescent OLEDs fabricated on the n-doped graphene cathode [graphene/Bphen:Cs<sub>2</sub>CO<sub>3</sub>/TPBI/CBP:Ir(ppy)<sub>3</sub>/CBP/MoO<sub>3</sub>/Al] showed similar operating voltage and higher luminous efficiencies ( $\sim 40\text{ cd/A}$ ,  $27\text{ lm/W}$ ) than OLEDs with ITO ( $\sim 37\text{ cd/A}$ ,  $24\text{ lm/W}$ ).

Stacking of two EL units on a graphene anode improves the efficiency and minimizes efficiency roll-off in OLEDs [119,120]. The bottom and top EL units emit light simultaneously, so tandem OLEDs can emit the same luminance at lower current density compared with single-unit OLEDs. Because decreased current

**Table 3**  
Summary of electrical and luminous characteristics in LEDs depending on type of graphene electrode, surface modification, and device structure.

Graphene	Dopant/Interlayer	$R_{sh}^a$ [ $\Omega/\text{sq}$ ]	WF <sup>b</sup> [eV]	Type	Max. CE <sup>c</sup> [cd/A]	Max. PE <sup>d</sup> [lm/W]	Max. EQE <sup>e</sup> [%]	Color	Ref.
rGO	-/-	800	-	Fluorescent OLED	-	0.3	0.2	green	[83]
Layer-by-layer assembled multilayered rGO	-/-	2500	-	Fluorescent OLED	0.1	-	-	green	[84]
Functionalized rGO/PEDOT:PSS composite	-/-	80	-	Fluorescent OLED	3.9	-	-	green	[85]
Layer-by-layer assembled multilayered rGO	-/-	298	-	Fluorescent OLED	4.5	-	-	green	[86]
Multilayered CVD-grown (Ni) graphene	$-\text{V}_2\text{O}_5$	310	5.4	Phosphorescent OLED	0.75	0.38	-	green	[87]
Four-layered CVD-grown (Cu) graphene	$\text{HNO}_3$ or $\text{AuCl}_3$ / self-organized polymeric layer	34	5.95	Phosphorescent OLED	98.1	102.7	-	green	[12]
Four-layered CVD-grown (Cu) graphene	$\text{HNO}_3$ / self-organized polymeric layer	84.2	5.95	Perovskite LED (MAPbBr <sub>3</sub> )	18.0	-	3.8	green	[91]
Single-layer CVD-grown (Cu) graphene	OA/ PEDOT:PSS/MoO <sub>3</sub>	200	5.1	Phosphorescent OLED (HL <sup>f</sup> )	80 (250)	- (160)	20 (60)	green	[89]
Tri-layered CVD-grown (Cu) graphene	MoO <sub>3</sub>	70	4.7	Phosphorescent OLED	60	45	-	green	[90]
Single-layer CVD-grown (Cu) graphene	WO <sub>3</sub> $\text{V}_2\text{O}_5$	300	-	Phosphorescent OLED	-	75	-	green	[88]
Five-layered CVD-grown (Cu) graphene	TFSA /PEDOT:PSS	90	5.1	Phosphorescent OLED Fluorescent Polymer LED	9.6	10.5	-	green yellow	[101]
Four-layered CVD-grown (Cu) graphene	TFMS/-	63	5.23	Phosphorescent OLED	104.1	80.7	-	green	[48]
N-doped rGO	Hydrazine and thermal annealing with $\text{NH}_3$ / ZnO	300	4.25	Fluorescent Inverted Polymer LED	7.0	-	-	green	[114]
Single-layer CVD-grown (Cu) graphene	Bphen:Cs <sub>2</sub> CO <sub>3</sub>	250	3.6	Phosphorescent Inverted OLED	40	27	-	green	[115]
Four-layered CVD-grown (Cu) graphene	$\text{HNO}_3$ / self-organized polymeric layer	58.3	5.95	Phosphorescent Tandem OLED (HS <sup>g</sup> )	205.9 (396.4)	-	45.2 (87.4)	green	[79]
Four-layered CVD-grown (Cu) graphene	TiO <sub>2</sub> /HNO <sub>3</sub> -doped/ self-organized polymeric layer	92.5	5.95	Phosphorescent OLED (HS <sup>g</sup> )	168.4 (257.0)	160.3 (250.4)	40.8 (64.7)	green	[80]
				Phosphorescent Tandem OLED (HS <sup>g</sup> )	-	120.8 (183.5)	62.1 (103.2)	green	

<sup>a</sup>  $R_{sh}$ : sheet resistance.

<sup>b</sup> WF: work function.

<sup>c</sup> Max. CE: maximum current efficiency.

<sup>d</sup> Max. PE: maximum power efficiency.

<sup>e</sup> Max. EQE: maximum external quantum efficiency.

<sup>f</sup> High refractive glass and lens.

<sup>g</sup> Hemispherical lens.

density and exciton population in tandem OLEDs can effectively reduce triplet-triplet annihilation and triplet-polaron annihilation, this stacking of EL units can significantly increase current efficiency and external quantum efficiency, and minimize efficiency roll-off.

T.-H. Han et al. developed tandem device architecture for flexible OLEDs on graphene anode [79]. This design was achieved by including Li<sub>3</sub>N that is low-temperature evaporable n-type dopant for organic materials in charge-generation layer (CGL) [2,9-dimethyl-4,7-diphenyl-1,10-phenanthroline (BCP):

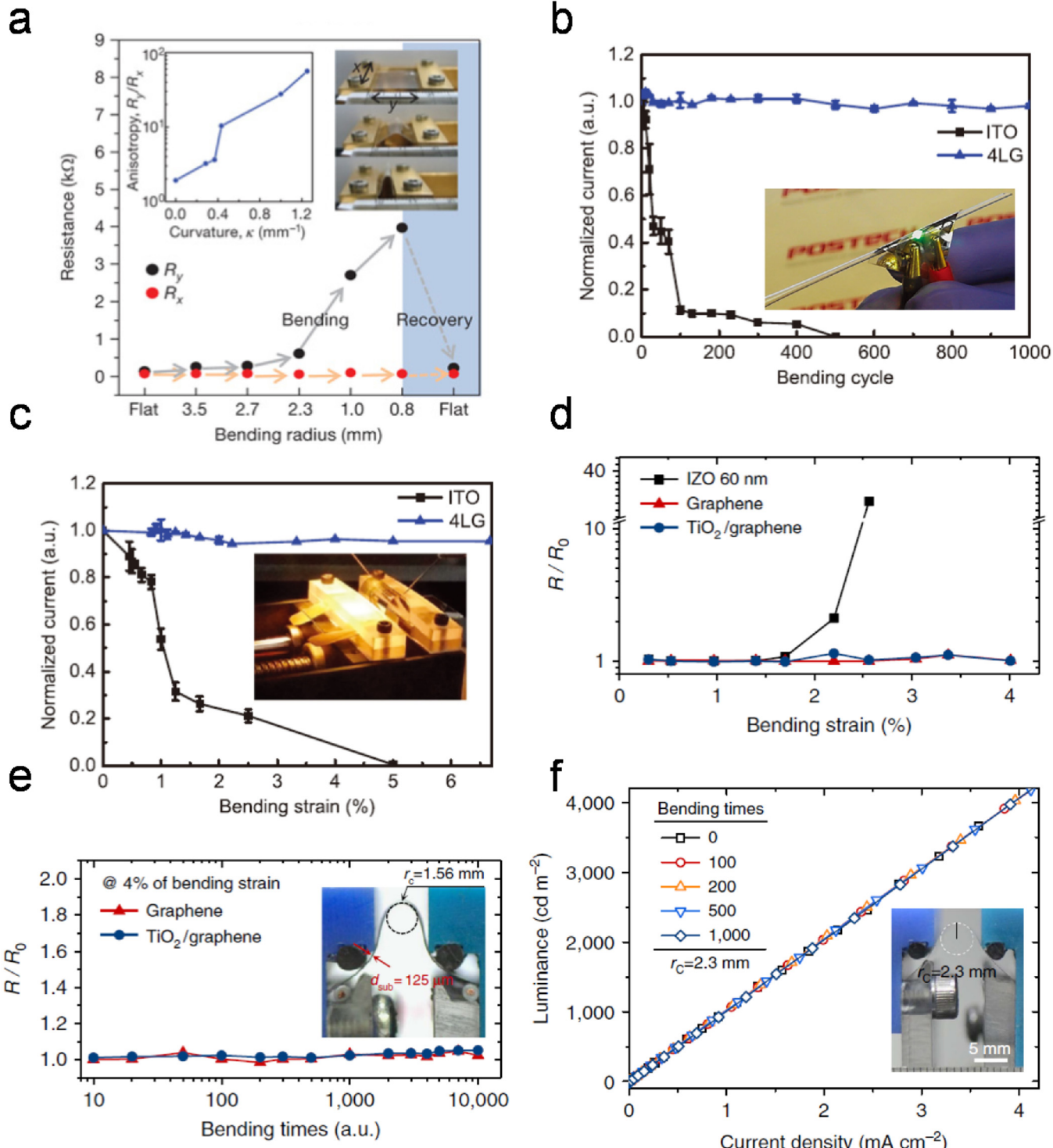


**Fig. 16.** (a) Effect of bending radius on electrical resistance of graphene on PDMS/PET substrate. Reproduced from [39] Copyright 2009, Nature Publishing Group, Normalized current density of flexible tandem OLEDs with graphene anode as a function of (b) Bending cycles with ~1.33% strain and (c) bending strain. Reproduced from [79] Copyright 2016, Nature Publishing Group, (d) Change in resistance of IZO, graphene, and TiO<sub>2</sub>/graphene as a function of bending strain, (e) Luminance versus current density characteristics according to bending cycles with radius of curvature ~2.3 mm, (f) Change in resistance of graphene and TiO<sub>2</sub>/graphene as a function of bending cycles with ~4% strain. Reproduced from [80] Copyright 2016, Nature Publishing Group.

$\text{Li}_3\text{N}/\text{MoO}_3/\text{TAPC}$ . This architecture was developed to effectively stack EL units and to enhance compatibility with plastic substrates of flexible OLEDs (Fig. 14c). Flexible tandem OLEDs with graphene anode had very high device efficiencies ( $\sim 205.9 \text{ cd/A}$ , 45.2%) and minimized efficiency roll-off ( $\sim 6.6\%$  decrease to emit  $10,000 \text{ cd/m}^2$ ) compared with those of single OLEDs ( $\sim 120.8 \text{ cd/A}$ , 32.7%, and 32.6% decrease to emit  $10,000 \text{ cd/m}^2$ ). Furthermore, introduction of a hemispherical lens that increases light out-coupling from the device increased its efficiencies to  $\sim 396.4 \text{ cd/A}$  and 87.4%, with efficiency roll-off of only  $\sim 3.8\%$  to emit  $10,000 \text{ cd/m}^2$  (Fig. 14d). The studies on device architecture of graphene-based OLEDs that improve device efficiency and stability should continue for practical application of flexible OLEDs.

### 3.6. Optical outcoupling of OLEDs on graphene

Light outcoupling is one of the most important factors that determine efficiency in OLEDs. The outcoupling efficiency of OLEDs is generally limited close to 30% when internal quantum efficiency is close to 100%. The low outcoupling efficiency is mainly due to waveguided light losses between layers and confined light at the substrate/air interface due to large difference in refractive indices of layers in OLEDs ( $n_{\text{org}} \sim 1.75$ ,  $n_{\text{ITO}} \sim 1.8$ ,  $n_{\text{sub}} \sim 1.4$ ) [122]. Understanding light outcoupling of graphene-based OLEDs is one of the most important topics to improve electroluminescent efficiency in flexible OLEDs. J. Wu et al. demonstrated that OLEDs with graphene anode have comparable optical performances to control devices on ITO [83]. For a given OLED structure [ITO (130 nm) or graphene (7 nm)/PEDOT:PSS/NPB/Alq<sub>3</sub>/LiF/Al], the fraction of photons that outcouple into air from devices with a graphene anode was comparable with that fraction in devices with ITO, and angular emission profiles of both types of OLEDs were nearly Lambertian. However, the fraction of power emitted as a function of wavelength and normalized wave vector differed: OLEDs with a thin graphene electrode had lower light loss to waveguide mode than did OLEDs with ITO anode. Theoretical analysis using the classical electromagnetic model of light outcoupling from green phosphorescent OLEDs that use graphene or ITO anode [anode/CBP: mCP: Ir(ppy)<sub>3</sub>/Al] suggested that outcoupling efficiency varies with thickness of anode and organic layers in OLEDs [94,123]. Because ITO has higher refractive index ( $1.8 \leq n \leq 2.1$ ) than typical organic materials ( $1.7 \leq n \leq 1.8$ ), the reflectance of the anode, and the weak microcavity interference in the device can be simply adjusted by varying ITO thickness. OLEDs with the ITO electrode are subject to a weak microcavity effect, so their outcoupling efficiencies change significantly with ITO thickness (Fig. 15a), and OLED with 70-nm-thick ITO gives high outcoupling efficiency  $\sim 30\%$ . However, an OLED with 150 nm-thick ITO anode that has comparable electrical conductivity with graphene showed similar outcoupling efficiency ( $\sim 25\%$ ) to an OLED with three- or four-layered graphene ( $\sim 24\%$ ). Although OLEDs that use graphene electrode cannot easily use the cavity resonance effect because of difficulty in controlling thickness of graphene, the ultimate limit of the total extracted light (defined as the sum of air-, waveguide-, and glass-confined-modes) was much higher in an OLED with the graphene anode than on a OLED with an ITO anode [94]. Therefore, the improved light-extraction structure can significantly increase out-coupling efficiency of an OLED that has a graphene anode [80,94].

OLEDs that exploit microcavity resonance can achieve very high luminous efficiency. This effect can be achieved by using an electrode architecture that is composed of graphene sandwiched between a transition metal oxide with high refractive index and a polymeric layer with low refractive index; this structure can form a dielectric mirror (Fig. 15b) [80]. High-refractive TiO<sub>2</sub> ( $n \sim 2.5$ ) and low refractive polymeric HIL (GraHIL,  $n \sim 1.42$ ) composed of

PEDOT:PSS and perfluorinated ionomer were used to sandwich a multilayered graphene anode [80]. The GraHIL develops a WF that increases gradually towards the overlying organic layer, and thereby facilitates hole injection from the graphene anode to the overlying layer by providing a good energy-level alignment. Furthermore, the synergetic interplay of high- $n$  and low- $n$  layers can greatly increase the microcavity resonance effect, and reduce light loss caused by surface plasmon polaritons (SPP) in OLEDs. Although design of first-order cavity increases the Purcell effect and reduces waveguide mode light loss, a recombination zone near the metal cathode increases SPP. The coupling of SPP tends to increase when a high- $n$  layer is used. However, inclusion of low- $n$  layer can redistribute relative powers towards a smaller in-plane wave vector, so SPP is reduced [80]. Simulated out-coupling efficiency of an OLED that uses the stacked electrode reaches  $\sim 44\%$  (Fig. 15c). Indeed, an OLED based on TiO<sub>2</sub>/graphene/GraHIL showed significantly higher luminous efficiency ( $\sim 40.8\%$ ,  $160.3 \text{ lm/W}$ ,  $168.4 \text{ cd/A}$ ) than those with graphene/GraHIL ( $\sim 31.7\%$ ,  $112.6 \text{ lm/W}$ ,  $119.0 \text{ cd/A}$ ). Moreover, a tandem OLED based on TiO<sub>2</sub>/graphene/GraHIL stacked electrode provided very high external quantum efficiency  $\sim 62.1\%$  (103.2% and  $183.5 \text{ lm/W}$  with a half-ball lens) (Fig. 15d). Therefore, precise design of graphene-based device architecture can greatly increase electroluminescent efficiencies of flexible OLEDs.

Overall, the described modifications of pristine graphene to achieve low  $R_{\text{sh}}$  and high WF, and precise design of device architecture directly influence the electroluminescent efficiencies of LEDs that use the graphene electrode (Table 3).

### 3.7. Device Bending stability of OLEDs on graphene

C. Lee et al. firstly measured intrinsic mechanical properties of defect-free monolayer graphene by using nano-indentation in atomic force microscopy [32]. Mechanically-exfoliated SLG has mechanical properties that exceed those of any materials ever measured. It has 200 times higher breaking strength (42 N/m) than steel, and the corresponding Young's modulus and intrinsic stress at 25% strain are  $\sim 1 \text{ TPa}$  and 130 GPa, respectively. K. S. Kim et al. reported large-scale graphene growth of multilayered graphene grown using Ni film as a metal catalyst, and measured electrical properties upon bending and stretching of graphene film transferred to flexible and stretchable PET substrates [39]. The reported excellent bending stability for flexible electronic applications; the electrode had  $R_{\text{sh}}$  that remained stable up to 2.3-mm of bending radius, which corresponds to 6.5% of bending strain, and the original  $R_{\text{sh}}$  was completely recovered after bending up to 0.8 mm, which corresponds to bending strain of 18.7%, (Fig. 16a) [39]. H. Chang also tested bendability of graphene composite electrode composed of SDBA-modified reduced graphene and PEDOT:PSS [85]. It showed only 5% increase in  $R_{\text{sh}}$  after 1000 bending cycles, and did not crack; in contrast, a conventional ITO on PET substrate showed 500-times increase in  $R_{\text{sh}}$  after only 13 bending cycles [85].

Practical applications of flexible electronics require guaranteed tolerance to mechanical strain. Flexible OLEDs with graphene anode show excellent stability under bending [79]. Two EL units were stacked on a graphene anode to increase device efficiency of flexible OLEDs (Section 3.5). In bending tests with  $\sim 1.33\%$  of bending strain, the current density of the flexible tandem OLED that uses graphene anode has remained stable after 1000 cycles without significant change in electrical properties, whereas current density of the device with ITO anode has dropped quickly, and the device completely failed at  $\sim 500$  cycles ( $\sim 1.33\%$  bending strain) (Fig. 16b). Influences of bending strain and radius of curvature on electrical properties of devices were also quantified to investigate electromechanical properties of the flexible tandem

OLED with the graphene anode. During gradual reduction in the bending radius, OLEDs with the graphene anode did not show notable decrease in current density until 6.7%, whereas in the device with the ITO anode, the current density drastically decreased (Fig. 16c). These differences in the electromechanical properties of OLEDs can attribute to easy crack formation in the ITO anode at bending strain >1% [11,42].

One novel flexible electrode architecture [80] uses graphene sandwiched between a high-refractive-index  $\text{TiO}_2$  layer and low-refractive-index HIL to increase the weak microcavity effect in flexible OLEDs (Fig. 15b,c). Although the metal oxide layer is usually regarded as brittle, the electrode that contains  $\text{TiO}_2$  layer under a graphene anode also shows excellent mechanical properties under bending stress.  $\text{TiO}_2$  film on PET substrate can withstand 4% strain without developing cracks; this increase in resistance of  $\text{TiO}_2$  to cracking can attribute to crack-deflection toughening (Fig. 16d) [124]. Therefore,  $\text{TiO}_2$ /graphene has maintained its  $R_{sh}$  after 10,000 bending cycles with 4% bending strain (Fig. 16e). As a result, a high-efficiency OLED that uses a flexible electrode (i.e.,  $\text{TiO}_2$ /graphene/GraHIL) showed excellent mechanical stability, and did not show decrease in efficiency after 1000 bending cycles (radius of curvature ~2.3 mm) (Fig. 16f). These results demonstrate that graphene-based OLEDs have great potential as next-generation flexible displays or light sources with high efficiency and without sacrifice of mechanical flexibility.

#### 4. Flexible solar cells with graphene

##### 4.1. Graphene as an electrode for organic solar cells

OSCs are promising power-supply devices owing to their light weight, flexibility and low fabrication cost based on ease of large-area processability. Basic operating mechanism of OSCs can be explained largely with three steps: 1) charge generation in a photo-active layer, 2) charge transport, and 3) charge collection into electrodes. A device has power conversion efficiency  $PCE = V_{OC} \times J_{SC} \times FF$ , where  $V_{OC}$  is open-circuit voltage,  $J_{SC}$  is proportional to integrated external quantum efficiency (EQE) as a function of wavelength. EQE can be expressed as,

$$\eta_{EQE} \propto \eta_{Abs} \eta_{CS} \eta_{CC}$$

where  $\eta_{Abs}$  is absorption efficiency,  $\eta_{CS}$  is charge separation efficiency, and  $\eta_{CC}$  is charge collection efficiency [125]; it depends on the number of charges generated after light absorption by a light absorber and the number of charges to be collected both by an anode and a cathode. The charge collection efficiency is strongly influenced by parasitic resistances such as series resistance and shunt resistance, which also affect FF; high series resistance and low shunt resistance cause low FF. Therefore, high  $T$  and electrical conductivity of a transparent conducting electrode are essential factors to achieve high charge generation rate and charge collection efficiency for high  $J_{SC}$  and FF, which together lead to high PCE. For these reasons, graphene is regarded as a suitable electrode of OSCs owing to its high  $T$  and sufficient electrical conductivity. Furthermore, the flexibility of graphene makes it compatible with flexible OSCs. However, practical application of graphene electrodes requires improvement of several characteristics such as electrical conductivity, uniform interlayer formation, and doping stability (Section 2). Here, we review progress in development of graphene electrodes for OSCs.

##### 4.2. Solution-processed graphene electrodes for organic solar cells

Initial research on development of OSCs with graphene electrodes used solution-processed graphene, because it can be

obtained easily by reducing GO synthesized using Hummer's method [36]. Although the various functionalities formed by the method allow GO to disperse well in solvents, the heterogeneous electronic structure with mixed  $sp^2$  and  $sp^3$  hybridizations reduces its electrical conductivity [126]. Therefore, the functionalities must be removed.

G. Eda et al. removed functionalities on GO by a combination of hydrazine vapor and thermal annealing (200 °C) [127]. The lowest  $R_{sh}$  of rGO film was  $\sim 10^5 \Omega/\text{sq}$  with  $T$  of 65%. Treatment of thionyl chloride ( $\text{SOCl}_2$ ) with rGO reduced  $R_{sh}$  of rGO film by a factor of 5; the resulting OSCs [rGO/PEDOT:PSS/P3HT:PCBM/Al] had  $PCE \sim 0.1\%$ . J. Wu et al. reduced GO either by vacuum annealing at high temperature (1100 °C) or by a combination of a hydrazine treatment and Ar annealing at 400 °C [128]; the resulting rGO had  $R_{sh} \sim 10^5 \Omega/\text{sq}$ , and a [rGO/CuPc/C<sub>60</sub>/BCP/Ag] device had  $PCE = 0.4\%$  under AM 1.5G simulated solar illumination at 85 mW/cm<sup>2</sup>.

Although rGO can withstand mechanical stress, demonstration of flexible OSCs that use rGO has been a difficult task because the flexible plastic substrates cannot endure the reduction process, which demands temperature greater than their glass transition temperature. This limitation of rGO application to plastic substrate was overcome by E. Kymakis et al. using a laser to reduce GO [129]; the laser-reduced GO (LrGO) had  $R_{sh} = 1.6 \text{ k}\Omega/\text{sq}$  and  $T = 70\%$  with the thickness of 16.4 nm. This method is practical for preparing an electrode *in situ* in one step without the conventional reduction process that requires high temperature and chemical reducing agents. A device [LrGO/PEDOT:PSS/P3HT:PCBM/Al] that used an LrGO electrode achieved  $PCE = 1.1\%$ .

A different approach by Yin et al. is to fabricate flexible OSCs that use an rGO electrode prepared by obtaining rGO on  $\text{SiO}_2/\text{Si}$  first, then transferring the rGO to PET [129]; the complete films were 10–21 nm thick, and had  $10^4 \leq R_{sh} \leq 10^3 \Omega/\text{sq}$  and  $55 \leq T \leq 88\%$ . However, [rGO/PEDOT:PSS/P3HT:PCBM: $\text{TiO}_2/\text{Al}$ ] devices had low  $0.28 \leq PCE \leq 0.78\%$ .

The general low  $PCE$  and especially the low  $FF$  of devices based on rGO can be attributed to the high  $R_{sh}$ , which impairs collection of charges generated in the photo-active layer. Although H. Feng et al. dramatically decreased  $R_{sh}$  of rGO to  $\sim 350 \Omega/\text{sq}$  by using  $\text{NaNH}_3$  as a reducing agent, the resulting rGO had high defect density, and therefore does not seem to be appropriate for application as an electrode in OSCs [130]. The defects can degrade the operation of OSCs by reducing charge-collection efficiency. In conclusion, rGO seems inappropriate as an electrode of OSCs due to its low electrical conductivity, low  $T$ , and high defect density.

##### 4.3. CVD-grown graphene electrode for organic solar cells

CVD-grown graphene has high quality with low density of defects, high electrical conductivity and high  $T$ , and therefore can be expected to efficiently transmit light to a photo-active layer and collect charge carriers as an electrode of OSCs and to yield higher  $J_{SC}$ ,  $FF$  and  $PCE$  than can be obtained using an rGO electrode. Moreover, achievement in large-scale demonstration of CVD-grown graphene by roll-to-roll process increased the feasibility of its use in practical applications [34]. However, raising the  $PCE$  of graphene devices up to that of ITO devices has been difficult due to several problems with graphene, including difficulty of forming a uniform interfacial layer, lower electrical conductivity than ITO, and unstable doping.

###### 4.3.1. Uniform formation of interlayers on graphene

Graphene is hydrophobic, but interfacial layer materials are generally based on hydrophilic solvents, so formation of a uniform interlayer on graphene has been a challenging task. The hydrophobicity causes formation of dewetted regions, which can provide paths for short currents, which degrade  $PCE$ , so the

interfacial layer must uniformly and completely cover the electrode. Several approaches to achieve this goal have been proposed.

Initially, UV-ozone or oxygen-plasma treatment to make the graphene surface hydrophilic by inducing formation of hydroxyl and carbonyl groups on it [73,131]. However, this approach damages the chemical structure of graphene, and thereby decreases its electrical conductivity [49], whereas efficient device operation requires relatively high conductivity in the electrode.

Other approaches to deposit a uniform interfacial layer on graphene can be largely categorized into three groups: 1) insertion of an interlayer between graphene and the charge-transporting layer, 2) engineering of an interfacial layer material, and 3) development of deposition processes.

**4.3.1.1. Introduction of surface-modifying layer or chemical treatment.** Deposition of a uniform charge transport layer on graphene can be achieved by changing its surface property by introducing an additional surface-modifying layer, or by chemical treatment to make the graphene hydrophilic.

Y. Wang et al. introduced pyrene buanoic acid succidymidyl ester (PBASE) on graphene electrodes and developed OSCs [graphene/PBASE/PEDOT:PSS/P3HT:PCBM/LiF/Al] that had  $PCE = 1.71\%$ , which is higher than those of devices that used pristine graphene (0.21%) or UV-ozone-treated graphene (0.74%) [73]. The increased  $PCE$  of the device using the PBASE-deposited graphene electrode was partly attributed to its improved hydrophilicity, which allowed PEDOT:PSS to effectively wet the surface.

H. Park et al. co-polymerized PEDOT with poly(3,4-ethylenedioxythiophene)-block-poly(ethylene glycol) doped with perchlorate (PEG(PC)) to render the polymer (PEDOT:PEG(PC)) soluble in organic solvent (nitromethane), so the polymer was successfully deposited on hydrophobic graphene surface by spin-coating [68];

however, additional deposition of PEDOT:PSS on PEDOT:PEG(PC) was necessary, because it is not capable alone as an HTL due to its low  $WF$ (4.3 eV) that causes a large energy difference ( $\sim 1.2$  eV) with the HOMO (5.5 eV), of the donor, tetraphenyldibenzoperiflanthene (DBP), in the photo-active layer. The device [graphene/PEDOT:PEG(PC)/PEDOT:PSS/DBP/C<sub>60</sub>/BCP/Al] achieved  $PCE = 2.9\%$ , whereas an otherwise-identical device that used ITO had  $PCE = 3.2\%$ .

Y. M. Lee et al. presented a way of using an engineered biotemplate of M13 viruses to overcome the problem of interfacial layer deposition on graphene [132]. The viruses were used to nondestructively functionalize graphene to render it hydrophilic. WO<sub>3</sub> was grown along the viral bodies by biomimetication from sodium tungstate precursor, then PEDOT:PSS was applied by spin coating. A [graphene/virus-templated WO<sub>3</sub>/PEDOT:PSS/PTB7:PC<sub>71</sub>BM/TiO<sub>x</sub>/Al] device achieved  $PCE = 5.30\%$  which is much higher than those of otherwise-identical devices that did not use the template ( $PCE = 0.39\%$ ).

Y. Wang et al. used a thermally evaporated 2-nm-thick MoO<sub>3</sub> layer to achieve effective wetting of PEDOT:PSS on graphene [133]. A [graphene/MoO<sub>3</sub>/PEDOT:PSS/P3HT:PCBM/LiF/Al] device achieved  $PCE = 2.5\%$ , whereas the device without the MoO<sub>3</sub> layer had  $PCE = 0.12\%$ .

**4.3.1.2. Solution engineering of interlayer materials.** Engineering interfacial charge extraction layer materials and depositing it directly on graphene without further chemical treatment or introduction of an extra surface-modifying layer on graphene can be a simple and efficient way to develop OSCs based on graphene electrodes.

H. Kim et al. overcame the poor film formation of PEDOT:PSS on graphene by using a mixture of PEDOT:PSS, isopropyl alcohol (IPA) and tetrafluoroethylene-perfluoro-3,6-dioxa-4-methyl-7-octene-sulphonic acid copolymer (a perfluorinated ionomer) to produce

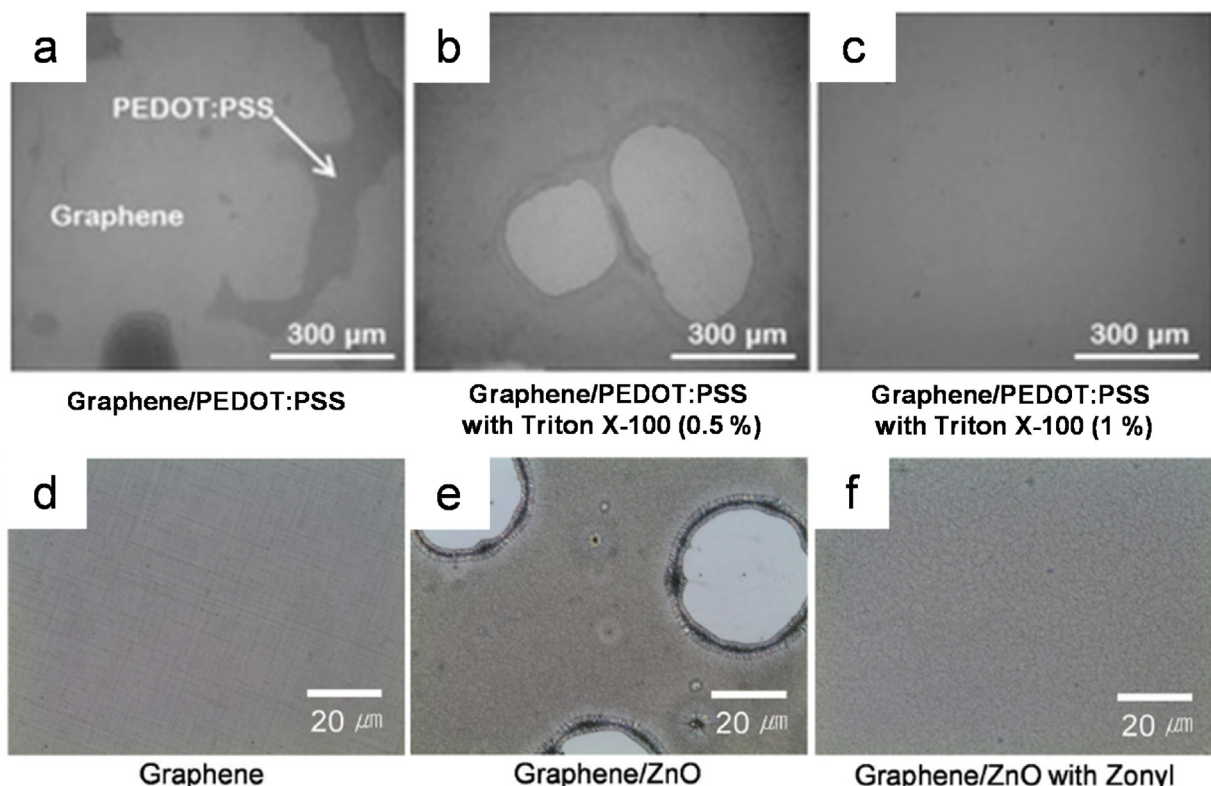


**Fig. 17.** Optical microscopic images of (a) Pristine PEDOT:PSS on graphene, (b) PEDOT:PSS with 0.5% of Triton X-100 and (c) PEDOT:PSS with 1% of Triton X-100. Reproduced from [69] Copyright 2015, Elsevier. Optical microscopic images of (d) Graphene, (e) ZnO on graphene, and (f) ZnO with Zonyl on graphene. Reproduced from [72] Copyright 2016, Wiley-VCH.

a gradient hole-extraction layer (GraHEL) [20]. The high surface ionization potentials of the GraHIL and of the GraHEL improve the energy-level alignment at the interface between anode and organic layer. The GraHEL is used to effectively extract holes generated in the photo-active layer without potential loss in solar cells, whereas the GraHIL is used to facilitate hole injection from anode to overlying organic layer by reducing the energy barrier between anode and EML. The composition of GraHIL is made of low conductive Clevios Al4083 and PFI to make less conductive and thus reduce leakage current while composition of GraHEL is made of more conductive Clevios PH and PFI to make more conductive and thus reduce contact resistance [12,20,134]. Pristine PEDOT:PSS had high contact angle on graphene surface, whereas a mixture of PEDOT:PSS and IPA, and the GraHEL both completely wetted the graphene surface. However, after spin-coating, only the GraHEL fully covered the graphene because the GraHEL contained a perfluorocarbon-based ionomer, which has low hydrophilicity. A [graphene/GraHEL/P3HT:PCBM/LiF/Al] device achieved  $PCE = 2.83\%$ .

H. Park et al. used poly(thiophene-3-[2-(2-methoxyethoxy)ethoxy]-2,5-diyl)(RG1200) as a HTL on graphene instead of PEDOT:PSS [135]. RG1200 is dissolved in organic solvent (ethylene glycol monobutyl ether), and can therefore form directly on graphene without any additional process. A [graphene/RG1200/DBP/C<sub>60</sub>/BCP/Al] device achieved  $PCE = 2.72\%$ , whereas a device that used only PEDOT:PSS had resistor-like current-voltage characteristics.

Surfactants can also be used to make a uniform charge transport layer on graphene. J.-B. Lee et al. used a solution of nonionic small-molecule surfactant (polyethylene glycol p-(1,3,3-tetramethylbutyl)-phenyl ether) (Triton X-100) in aqueous PEDOT:PSS to achieve good wetting on graphene [69]. As the amount of Triton X-100 was increased to 1%, the contact angle of the solution on graphene decreased. PEDOT:PSS with 1% Triton X-100 formed uniform thin films, whereas pristine PEDOT:PSS and PEDOT:PSS with 0.5% of Triton X-100 left dewetted regions (Fig. 17a–c). A [graphene/PEDOT:PSS:Triton X-100/P3HT:PCBM/Ca/Al] device achieved  $PCE = 3.19\%$ .

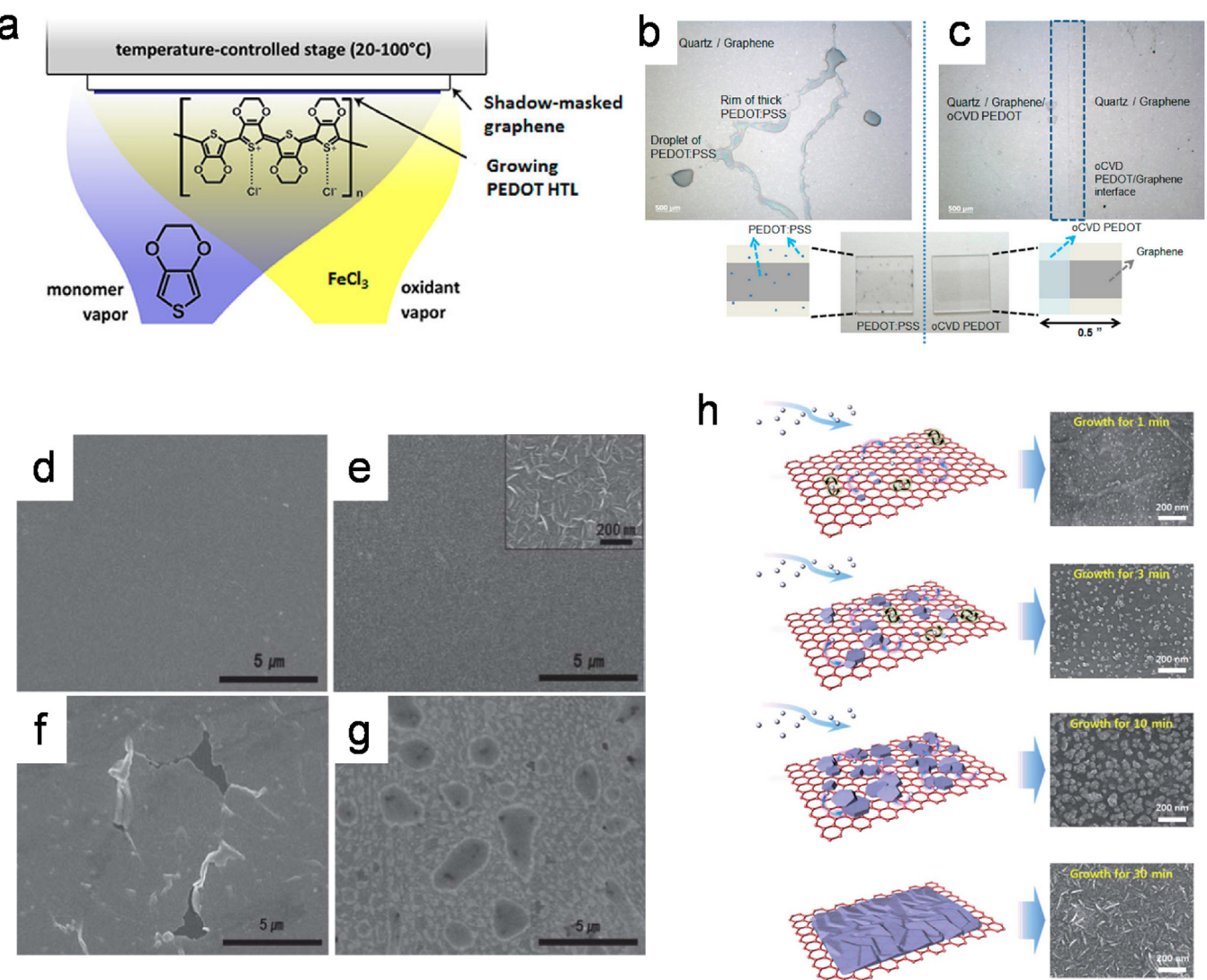


**Fig. 18.** (a) oCVD process for vapor printing PEDOT on graphene by vaporizing EDOT monomer and oxidant agent  $\text{FeCl}_3$ . (b) Spin-cast PEDOT:PSS on graphene yielding agglomeration of PEDOT:PSS and dewetted region. (c) Uniform and full covered PEDOT vapor printed on graphene. Reproduced from [70] Copyright, 2012 American Chemical Society. FE-SEM images of (d) only graphene and ZnO thin film prepared by (e) MPCVD (inset: magnified FE-SEM image), (f) sputtering, and (g) sol-gel method on graphene layer. (h) Schematics of ZnO thin film growth on graphene by MPCVD as a function of time and corresponding FE-SEM images at each step. Reproduced from [137] Copyright, 2012 The Royal Society of Chemistry.

H. Kim et al. developed inverted OSCs that use ZnO as the ETL which precursor solution was composed of hydrophilic alcohol-based solvents (1:1 ratio of 2-methoxyethanol and methanol). Addition of a fluorosurfactant (Zonyl) into the precursor solution achieved uniform formation of a ZnO layer on the graphene surface; this success was attributed to the amphiphilic chemical structure of the additive (Fig. 17d-f) [72]. A [graphene/ZnO with Zonyl/PTB7:PC<sub>71</sub>BM/MoO<sub>3</sub>/Ag] device that used this modified ZnO ETL on graphene achieved  $PCE = 7.51\%$ , which was identical to that of a device that used ITO. In both of these studies [69,72] the uniformly-formed interfacial layer doped graphene without introducing extra dopants. The doping mechanism and its effects are presented in Section 4.3.2.2.

**4.3.1.3. Development of deposition process.** H. Park et al. developed oxidative chemical vapor deposition (oCVD) method to directly deposit PEDOT on graphene, and thereby overcame the difficulty of

forming aqueous PEDOT:PSS on hydrophobic graphene by spin-coating [70]. Specifically, oCVD synthesizes conducting polymer chains from vapor-phase (3,4-ethylenedioxythiophene) monomer with FeCl<sub>3</sub> as an oxidizing agent. Therefore, a thin film of PEDOT is deposited on a graphene surface at substrate temperature of 120 °C (Fig. 18a). Vapor-printed PEDOT coated the graphene uniformly, whereas PEDOT:PSS cast by spin-coating had dewetted regions (Fig. 18b, c). A [graphene/vapor printed PEDOT/DBP/C<sub>60</sub>/BCP/Al] device had  $PCE = 3.01\%$ ; an otherwise-identical device using ITO anode had  $PCE = 3.20\%$ .

K.-S. Shin et al. developed a way to deposit ZnO ETL by mist pyrolysis CVD (MPCVD) for inverted OSCs based on a graphene cathode (Fig. 18d) [136]. ZnO film deposited by MPCVD on graphene was clean and uniform, whereas ZnO film prepared by sputtering and sol-gel process showed numerous cracks and dewetted regions (Fig. 18e-h). Raman spectra of graphene with MPCVD-grown ZnO had a low D peak, which indicates that damage

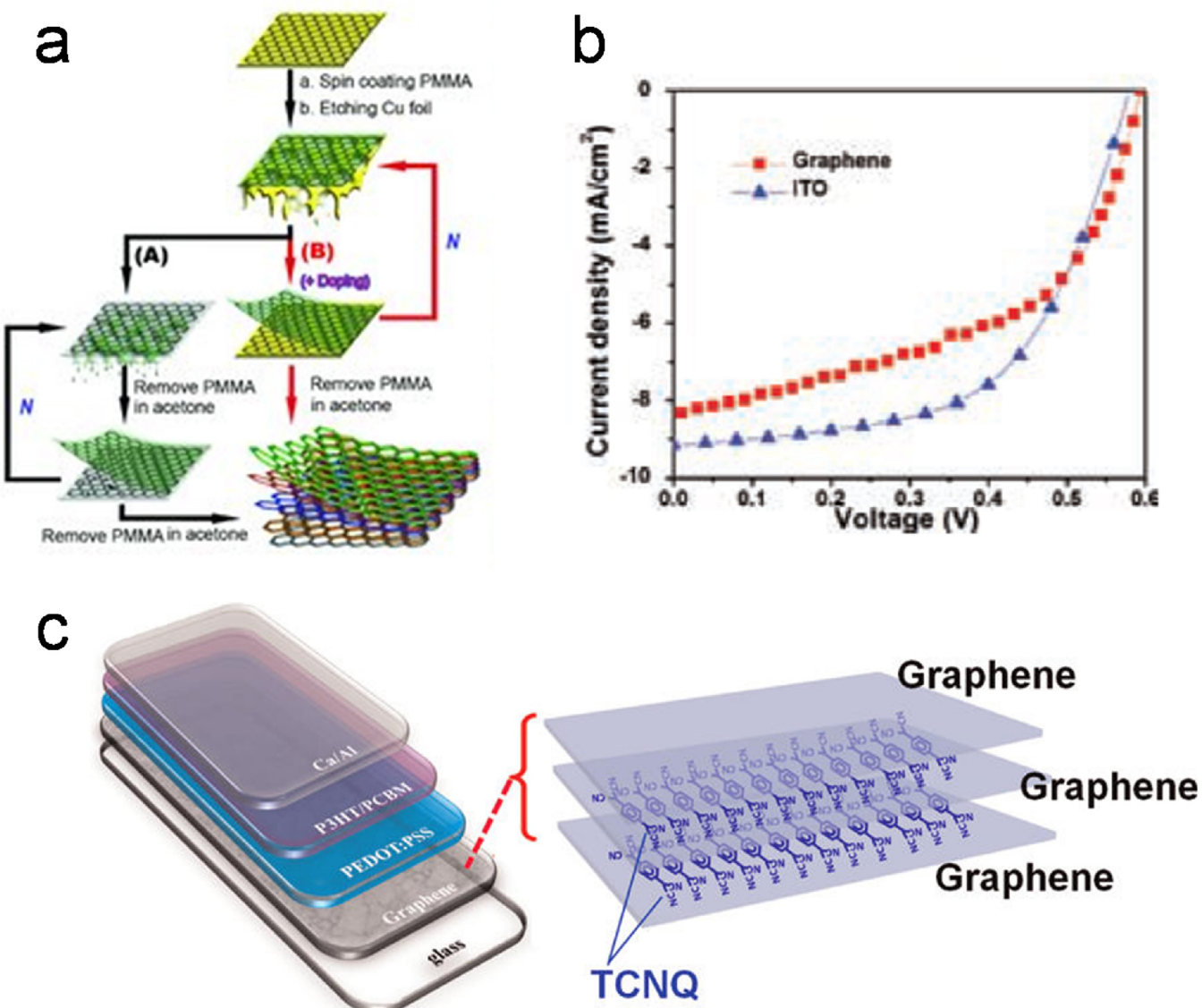


**Fig. 19.** (a) Schematic of comparison between conventional wet transfer method (route A) and layer-by-layer doping transfer method (route B). (b)  $J-V$  characteristics of devices using layer-by-layer doped graphene electrode and ITO electrode. Reproduced from [139] Copyright, 2011 Wiley-VCH. (c) Schematic of layer-by-layer doped graphene by embedded TCNQ between (right) and device configuration using it as an anode (left). Reproduced from [105] Copyright, 2012 American Chemical Society.

is negligible; graphene with sputtered ZnO had a high D peak. A [graphene/MPCVD-grown ZnO/P3HT:PCBM/MoO<sub>3</sub>/Ag] device prepared using this method had  $PCE = 1.55\%$ .

#### 4.3.2. Graphene doping for an electrode of OSCs

Doping of graphene electrodes to increase the electrical conductivity and tune WF is also very important for achieving high efficiency of OSCs because the  $FF$  is critically dependent on the sheet resistance of electrodes, and  $V_{OC}$  is also quite dependent on the interface energetics between the graphene electrode and the adjacent organic layer. Therefore, charge-transfer doping of graphene is more suitable for OSCs to avoid degrading its electrical conductivity. Here, we introduce various doping methods for development of OSCs based on these factors.

**4.3.2.1. Conventional doping method.** S. Lee et al. studied the doping effect of HNO<sub>3</sub> and SOCl<sub>2</sub> on graphene and the photovoltaic characteristics when using the graphene as electrodes [138]. The electrodes were composed of multilayer graphene films synthesized using a Ni catalyst; pristine graphene had  $R_{sh} \sim 850 \Omega/\text{sq}$ , but after doping the  $R_{sh}$  was significantly reduced to  $\sim 450 \Omega/\text{sq}$ . Effective doping of graphene was confirmed by Raman spectra that showed an increase in the intensity ratio of the G and 2D peaks ( $I_{2D}/I_G$ ) in both cases compared to pristine graphene. Also, change in WF after the doping was measured using Kelvin probe. Also, WF of pristine graphene (4.6 eV) increased to 4.9 eV after HNO<sub>3</sub> doping and to 5.1 eV after SOCl<sub>2</sub> doping. Doped graphene was applied as an electrode in the devices; as a result of the reduced  $R_{sh}$ , HNO<sub>3</sub> doping increased the  $FF$  from 52.5 to 55.2, and SOCl<sub>2</sub> doping increased the  $FF$  to 59.1. However,  $V_{OC}$  did not change despite the change in WF after doping; this can be attributed to energy-level pinning by PEDOT:PSS due to Ohmic contact between graphene and PEDOT:PSS.

Y. Wang et al. introduced a direct layer-by-layer transfer method that can minimize the effect of impurities caused by PMMA residue [139]. Unlike the conventional layer-by-layer transfer method in which each graphene layer should be supported by a PMMA layer, which must be removed after each transfer step, the direct method requires only one coating of a PMMA supporting layer on the first graphene/Cu foil layer, because the PMMA-coated graphene after Cu foil etching can be directly transferred onto the next graphene/Cu foil (Fig. 19a). After etching the Cu foil, the same stacking process can be done N times, and the PMMA layer can be removed once (route B). Organic solvents (usually acetone) cannot completely remove the PMMA residues. However, this process can avoid the PMMA residue between stacked graphene layers. During the individual transfer process, HCl is used to dope each layer; after the PMMA is removed, HNO<sub>3</sub> is used to dope the graphene. After doping, the graphene had  $R_{sh} \sim 80 \Omega/\text{sq}$  with  $T \sim 90\%$  at 550 nm. OSCs based on the electrode achieved  $PCE$  of  $\sim 2.5\%$ , which is slightly lower than  $PCE$  of the device based on ITO ( $PCE = 3\%$ ) (Fig. 19b).

C.-L. Hsu et al. used vacuum-deposited tetracyanoquinodimethane (TCNQ) as a p-dopant and evaporated Au as a supporting layer instead of PMMA for layer-by-layer doping of graphene [105]. The process can avoid use of chemical solvent (e.g. acetone) and polymeric resists (PMMA). The TCNQ (T) was deposited between graphene (G) layers (i.e., G/T/G...) by gas phase diffusion at 200 °C for 8 h.  $R_{sh}$  of graphene decreased as the number of embedded TCNQ layers increased; undoped graphene had average  $R_{sh} \sim 839 \Omega/\text{sq}$ , whereas G/T/G/T/G/T/G film had  $R_{sh} \sim 182 \Omega/\text{sq}$  mainly due to increase in hole carrier concentration. WF of the electrode increased from 5.0 eV to 5.2 eV. The device with G/T/G/T/G electrode optimized the trade-off between  $R_{sh}$  and  $T$ , and therefore showed the highest  $PCE = 2.58\%$  (Fig. 19c).

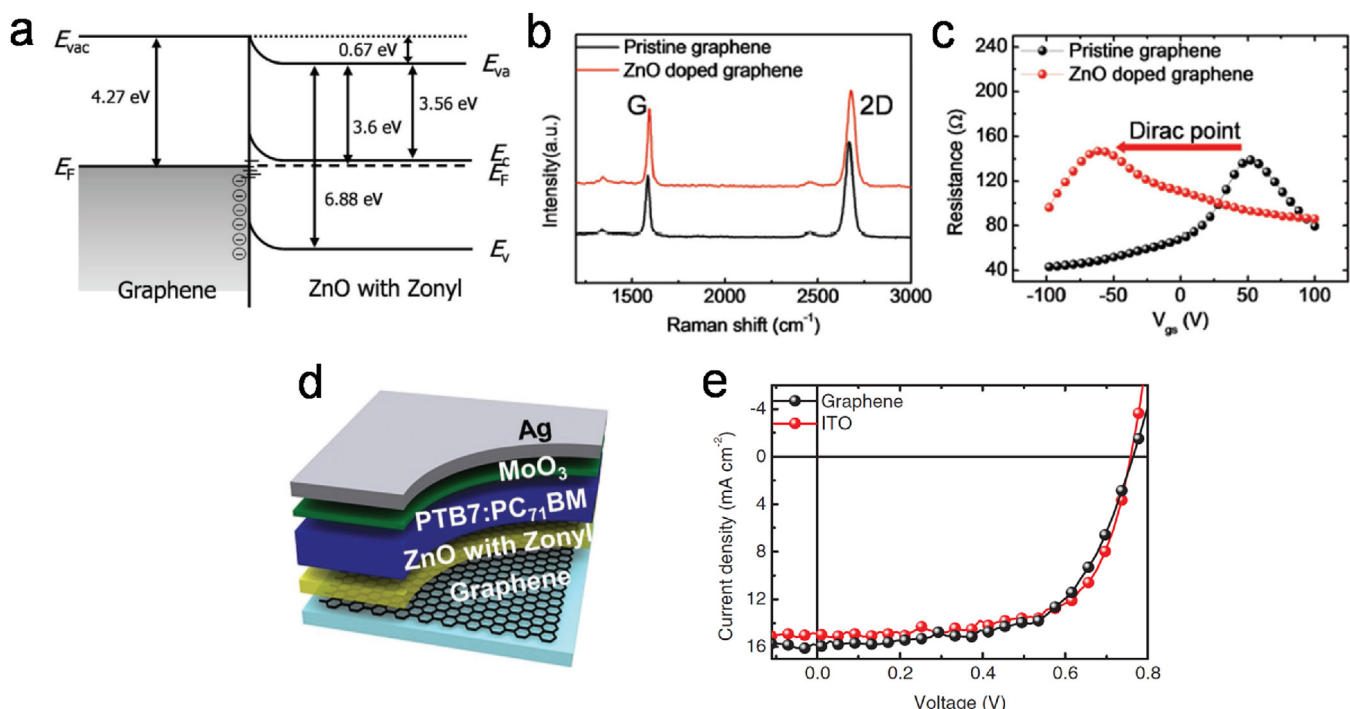


**Fig. 20.** (a) Energy-band diagram of graphene/ZnO with Zonyl, (b) Raman spectra of pristine graphene and ZnO-doped graphene, (c) Resistance of GFETs representing negative shift of Dirac point by use of ZnO-doped graphene, (d) Device configuration of inverted OSC using the graphene as a cathode and (e)  $J$ - $V$  characteristics of graphene and ITO device. Reproduced from [72] Copyright, 2016 Wiley-VCH.

Although the complicated layer-by-layer doping processes described above have reduced  $R_{sh}$ , it is still not sufficient for organic device applications. Therefore, to achieve lower  $R_{sh}$ , we may need to develop both more-promising chemical doping materials and stable doping and transfer processes at the same time.

**4.3.2.2. On-fabrication doping method.** Chemical dopants for conventional doping have demerits such as strong acidity and volatility. The acidity can impede the fabrication process, and the volatility can decrease the doping stability. These problems complicate development of large-scale or industrial-scale processes. Layer-by-layer doping may have the advantage of achieving stable doping, but is labor intensive. The problems can be overcome by on-fabrication doping using a HTL or an ETL that must be placed on the electrode of OSCs.

H. Kim et al. developed on-fabrication doping method where graphene can be doped on-site by a ZnO ETL that was modified by adding small amount of fluorosurfactant (Zonyl) to form a complete layer on hydrophobic graphene (Section 4.3.1.2) [72]. ZnO has a higher Fermi level than graphene, so electrons move from ZnO to graphene, which becomes n-doped. Although Fermi-level alignment causes band bending between graphene and the ZnO, pinned contact forms, which facilitates charge transfer according to Bardeen model [140], so charge extraction and charge collection are efficient. n-Doping of graphene by the modified ZnO caused decreased intensity ratio of 2D/G in Raman spectra, and a shift of the Dirac point in graphene field-effect transistors (GFETs) (Fig. 20a, b). Also, photoemission spectroscopic studies also supported the n-doping effect representing shift in energy level of graphene/modified ZnO system. A device that used a graphene electrode had  $V_{OC} = 0.766$  V,  $J_{SC} = 15.87$  mA cm $^{-2}$  and  $FF = 61.8$ , and a device that used an ITO electrode had  $V_{OC} = 0.759$  V,  $J_{SC} = 14.91$  mA cm $^{-2}$  and  $FF = 66.4$ . Both devices had  $PCE = 7.51\%$ . The higher  $J_{SC}$  in the graphene device was attributed to the higher  $T$  of graphene electrode than ITO leading to higher exciton-generation rate in the photo-active layer, but the lower  $FF$  in the graphene device was attributed to higher  $R_{sh}$  and charge traps in PMMA residue on graphene.

J.-B. Lee et al. used a PEDOT:PSS layer as a p-dopant for the graphene electrode of an OSC that has a standard structure [69]. The doping effect is signaled by a change in  $R_{sh}$  (Fig. 21a). Pristine graphene had average  $R_{sh} \sim 300 \Omega/\text{sq}$ , but after deposition of PEDOT:PSS with Triton-X (Fig. 21b, red column)  $R_{sh}$  decreased to  $<200 \Omega/\text{sq}$ . In contrast, the little change and the large variation in average  $R_{sh}$  of graphene/PEDOT:PSS compared to those of pristine graphene can be attributed to the non-uniform coverage of the pristine PEDOT:PSS on graphene; this non-uniformity may impede

efficient p-doping of graphene (Fig. 21b, green column). Also, the Dirac point shift of graphene to positive voltage after deposition of PEDOT:PSS with Triton X-100 indicated that the graphene had been p-doped (Fig. 21c). The device based on the graphene electrode doped by PEDOT:PSS with Triton X-100 had higher  $PCE$  (3.19%) than did a device that used HNO<sub>3</sub> doped graphene electrode (1.98%).

On-fabrication solid-state doping can reduce the time and cost of the process, and may achieve stable doping by capping graphene with solid-state thin film. Therefore, this method is among the most efficient for fabrication of OSCs based on graphene electrodes. Previous studies have reported numerous graphene electrode-based devices fabricated in a variety of ways (Table 4).

#### 4.3.3. Flexible OSCs that use flexible graphene electrodes

One of the merits of graphene electrode is mechanical stability under bending. L. Arco et al. demonstrated flexible OSCs that use flexible graphene electrodes on PET substrates. The conductance of PET/graphene film decreased little as a function of bending angle, and the conductance recovered when bending angle was decreased. In contrast, the conductance of PET/ITO film gradually decreased as bending angle increased, then decreased suddenly at bending angle  $>128^\circ$  (Fig. 22a, b), [150]. The conductance of the PET/ITO device was not recovered after the bending angle was reduced; this failure can be attributed to cracks in ITO. When the electrodes were applied to solar cells, graphene-based devices endured until bending angle of  $138^\circ$  without significant degradation of J-V characteristics, but the device using ITO electrode failed at bending angle of only  $60^\circ$  (Fig. 22c, d). The graphene device did not show any microcracks, whereas the ITO device showed numerous cracks after bending (Fig. 22e).

S. Lee et al. also compared mechanical stability of flexible OSCs that use graphene and ITO electrodes on PET substrate [146]. The graphene devices endured bending until the distance between ends of the device was reduced from 15.2 (laid flat) to 11.2 mm, whereas a device based on ITO failed when the distance reached 14 mm.

H. Park et al. also demonstrated flexible OSCs [graphene/PEDOT:PSS/MoO<sub>3</sub>/PTB7:PC<sub>71</sub>BM/Ca/Al] that achieved  $PCE = 6.1\%$  [151]; device characteristics were not degraded by flexing (Fig. 23). Studies reviewed in this section on development of OSCs that use flexible graphene electrodes demonstrated in common the mechanical superiority of graphene over ITO.

#### 4.4. Perovskite solar cells using graphene electrode

Solar cells that use organic-inorganic hybrid perovskites as a light harvester have achieved  $PCE > 20\%$  [152,153]. With the

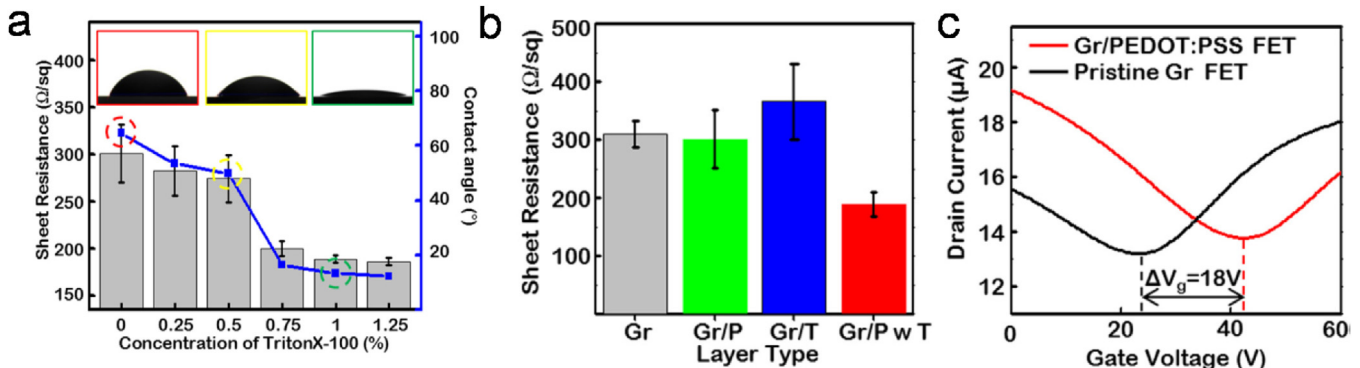


**Fig. 21.** (a) Change in sheet resistance of graphene and contact angle of PEDOT:PSS as a function of Triton X-100 concentration. (b) Sheet resistance of graphene, graphene/PEDOT:PSS, graphene/Triton X-100, and graphene/PEDOT:PSS with Triton X-100. (c) Drain current of GFETs representing positive shift in Dirac point using PEDOT:PSS doped graphene. Reproduced from [69] Copyright 2015, Elsevier.

**Table 4**

Summary of information about graphene electrodes and OSCs that used the electrodes.

Electrode	Dopant	R <sub>sh</sub> <sup>a</sup> [Ω/sq]	Optical Transmittance [%]	Substrate	Device configuration	PCE <sup>b</sup> [%]	Ref.
CVD-grown (Cu) graphene anode	–	210–1350	72–91 @ 550 nm	Glass	G <sup>c</sup> /PBASE <sup>d</sup> /PEDOT:PSS /P3HT:PCBM/LiF/Al ITO/PEDOT:PSS /P3HT:PCBM/LiF/Al G/WPF-6-oxy-F <sup>e</sup> /P3HT:PCBM/PEDOT:PSS/Al ITO/WPF-6-oxy-F /P3HT:PCBM/PEDOT:PSS/Al	1.71	[73]
ITO anode	–	–	–		ITO/PEDOT:PSS	3.10	
CVD-grown (Ni) graphene cathode	–	520–850	85–90 @ 450 nm	Glass	G/WPF-6-oxy-F <sup>e</sup> /P3HT:PCBM/PEDOT:PSS/Al ITO/WPF-6-oxy-F /P3HT:PCBM/PEDOT:PSS/Al	1.23	[141]
ITO cathode	–	–	–		ITO/PEDOT:PSS /P3HT:PCBM/TiO <sub>x</sub> /Al	2.23	
CVD-grown (Ni) graphene anode	–	~606	~87 @ 515 nm	Glass	G/PEDOT:PSS /P3HT:PCBM/TiO <sub>x</sub> /Al	2.60	[142]
ITO anode	–	–	–		ITO/PEDOT:PSS /P3HT:PCBM/TiO <sub>x</sub> /Al	3.80	
CVD-grown (Ni) graphene anode	–	~3.5 k	89 @ 550 nm	PET <sup>f</sup>	G/PEDOT:PSS /CuPc <sup>g</sup> / <sub>60</sub> /BCP <sup>h</sup> /Al	1.18	[143]
ITO anode	–	–	–		ITO/PEDOT:PSS /CuPc/ <sub>60</sub> /BCP/Al	1.27	
CVD-grown (Cu) graphene anode	AuCl <sub>3</sub>	~300 (Before doping)	91.2 @ 550 nm	Glass	G/PEDOT:PSS /CuPc/ <sub>60</sub> /BCP/Ag	1.63	[131]
ITO anode	–	–	–		ITO/PEDOT:PSS /CuPc/ <sub>60</sub> /BCP/Ag	1.77	
CVD-grown (Cu) graphene anode	–	~250	~95 @ 550 nm	Glass	G/PEDOT:PSS /CuPc/ <sub>60</sub> /BCP/Ag	0.85	[144]
CVD-grown (Cu) graphene anode	–	374	84.2 @ 400–600 nm	Glass	G/PEDOT:PSS /P3HT:PCBM/Ca/Al	1.17	[145]
ITO anode	–	–	–		ITO/PEDOT:PSS /P3HT:PCBM/Ca/Al	3.43	
CVD-grown (Cu) graphene anode	–	1.2–2.2 k	75–82	Glass	G/Au/PEDOT:PSS /P3HT:PCBM/LiF/Al	1.24	[136]
ITO anode	–	–	–		ITO/PEDOT:PSS /P3HT:PCBM/LiF/Al	3.10	
CVD-grown (Cu) graphene anode	–	~300	~92 @ 550 nm	Glass	G/vapor printed PEDOT /DBP/ <sub>60</sub> /BCP/Al	3.01	[70]
ITO anode	–	–	–		ITO/PEDOT:PSS /DBP/ <sub>60</sub> /BCP/Al	3.20	
CVD-grown (Cu) graphene anode	–	278	82.6 @ 550 nm	PEN <sup>i</sup>	G/ZnO/P3HT:PCBM/MoO <sub>3</sub> /Ag	1.55	[137]
CVD-grown (Ni) graphene anode	HNO <sub>3</sub>	~450	90 @ 400–1400 nm	PET	G/PEDOT:PSS /P3HT:PCBM/Ca/Al	2.54	[146]
CVD-grown (Cu) graphene anode	SOCl <sub>2</sub>	(After doping)	91.8 @ 550 nm	Glass	G/PEDOT:PEG(PC) <sup>k</sup> /PEDOT:PSS/DBP/ <sub>60</sub> /BCP/Al	2.60	[68]
ITO anode	–	~300	–		ITO/PEDOT:PEG(PC) /PEDOT:PSS/DBP/ <sub>60</sub> /BCP/Al	2.9	
CVD-grown (Cu) graphene anode	–	~300	92 @ 550 nm	Glass	G/RG1200 /DBP/C60/BCP/Al	3.2	[147]
ITO anode	–	–	–		ITO/RG1200 /DBP/C60/BCP/Al	2.72	
CVD-grown (Cu) graphene cathode	–	~300	92 @ 550 nm	PEN	G/ZnO/PTB7:PC <sub>71</sub> BM /MoO <sub>3</sub> /Ag	2.78	
ITO cathode	–	–	–		G/ZnO/PTB7:PC <sub>71</sub> BM /MoO <sub>3</sub> /Ag	7.1	[148]
CVD-grown (Cu) graphene anode	–	–	~95 @ 550 nm	Glass	G/v-WO <sub>3</sub> <sup>l</sup> /PEDOT:PSS /PTB7:PC <sub>71</sub> BM/TiO <sub>x</sub> /Al	7.6	
CVD-grown (Cu) graphene anode	HCl, HNO <sub>3</sub> (LBL <sup>m</sup> doping)	~80 (After doping)	~90 @ 550 nm	Glass	G/MoO <sub>3</sub> /PEDOT:PSS /P3HT:PCBM/LiF/Al	5.30	[149]
ITO anode	–	–	–		ITO/PEDOT:PSS /P3HT:PCBM/LiF/Al	2.5	[139]
CVD-grown (Cu) graphene anode	TCNQ <sup>n</sup> (LBL doping)	278 (After doping)	92.2 @ 550 nm	Glass	G/PEDOT:PSS /P3HT:PCBM/Ca/Al	3.0	
ITO anode	–	–	–		ITO/PEDOT:PSS /P3HT:PCBM/Ca/Al	2.58	[105]
CVD-grown (Cu) graphene anode	PEDOT:PSS :Triton X-100 (On-fab. <sup>o</sup> doping)	56.3 (After doping)	–	PET	G/PEDOT:PSS:Triton X-100 /P3HT:PCBM/Ca/Al	4.10	
CVD-grown (Cu) graphene cathode	ZnO:Zonyl (On-fab. doping)	~300 (Before doping)	~92 @ 550 nm	Glass	G/ZnO:Zonyl /PTB7:PC <sub>71</sub> BM/MoO <sub>3</sub> /Ag	3.19	[69]
ITO cathode	–	–	–		ITO/ZnO:Zonyl /PTB7:PC <sub>71</sub> BM/MoO <sub>3</sub> /Ag	7.51	
						7.51	[72]

<sup>a</sup> R<sub>sh</sub>: sheet resistance.<sup>b</sup> PCE: power conversion efficiency.<sup>c</sup> G: Graphene.<sup>d</sup> PBASE: pyrene buanoic acid succidymidyl ester.<sup>e</sup> WPF-6-oxy-F: poly[(9,9-bis((6'-(N,N,N-trimethylammonium) hexyl)-2,7-fluorene)-alt-(9,9-bis(2-(2-(2-methoxyethoxyethoxy) ethyl)-9-fluorene))dibromide.<sup>f</sup> PET: polyethylene terephthalate.<sup>g</sup> CuPc: Copper phthalocyanine.<sup>h</sup> BCP: bathocuproine.<sup>i</sup> DBP: tetraphenylbenzoperiflanthene.<sup>j</sup> PEN: polyethylene naphthalate.<sup>k</sup> PEDOT:PEG(PC): poly(3,4-ethylenedioxythiophene)-block-poly(ethylene glycol) doped with perchlorate.<sup>l</sup> v-WO<sub>3</sub>: virus-templated WO<sub>3</sub>.<sup>m</sup> LBL: layer-by-layer.<sup>n</sup> TCNQ: tetracyanoquinodimethane.<sup>o</sup> On-fab.: On-fabrication.

surprising improvement, research on development of flexible perovskite solar cells (PeSCs) that use graphene electrodes have been developed [154–157]. However, the low glass transition temperature of plastic substrates has limited the available device configuration to low- $T$  processed planar heterojunction (PHJ) PeSCs [158]. H. Sung et al. developed highly efficient PHJ PeSCs based on CVD-grown graphene electrode, but did not report flexible devices [159]. A thin MoO<sub>3</sub> layer deposited on graphene made it hydrophilic and caused p-type doping, which increased its WF. Deposition of a 2-nm-thick MoO<sub>3</sub> layer reduced the contact angle of PEDOT:PSS on graphene from 90.4° to 30.0° (Fig. 24a); concurrent change in  $R_{sh}$  from  $>2\text{ k}\Omega/\text{sq}$  to  $\sim 500\text{ }\Omega/\text{sq}$  after deposition of MoO<sub>3</sub> suggested doping of graphene. A [graphene/MoO<sub>3</sub> (2 nm)/PEDOT:PSS/CH<sub>3</sub>NH<sub>3</sub>PbI<sub>3</sub>/C<sub>60</sub>/BCP/LiF/Al] device had PCE = 17.1% which is slightly lower than PCE of the device with ITO/MoO<sub>3</sub> (1 nm) (18.8%) (Fig. 24c, d).

J. Yoon et al. developed flexible PHJ PeSCs with basically the same device structure except for the substrate; PEN was chosen as the plastic substrate (Fig. 25a) [155]. The mechanical stability of the devices was investigated under bending to various radii. Because of graphene's mechanical durability, the normalized PCE of a flexible graphene device was maintained with little change, but that of the flexible ITO device decreased (Fig. 25b). Normalized PCE as a function of bending cycles showed a similar trend to that in the bending-radius test (Fig. 25c). Furthermore, the perovskite layer on flexible graphene was not damaged significantly by bending, but a crack formed on brittle ITO and propagated into the perovskite layer (Fig. 25d, e); this result indicates that mechanical stability of an electrode in PeSCs can strongly affect the overlying layers, and thereby influence the long-term stability of the device.

## 5. Field-effect transistor using graphene

### 5.1. Requirement of materials for FETs

Improvements in metal-oxide semiconductor FETs have driven enormous development in the electronics industry [160]. In general, FETs are thin-film transistors, in which a semiconducting channel is deposited on top of a dielectric layer, which has electrical contact with a gate electrode. Source and drain electrodes also contact the channel, through which charge flows from source to drain. If voltage is not applied to the gate, minimal current flows through the channel; this is the “off” state. When voltage is applied to the gate, charges are induced at the interface of channel and dielectric, so current flows through the channel; this is the “on” state. The ratio of the current flowing during the “on” and “off” states is the “on/off ratio”, which determines the switching characteristics of FETs.

To achieve outstanding electrical properties for practical application, four requirements must be satisfied: i) to provide efficient charge injection from electrode to channel, energy-level mismatch between electrode WF and the valence or conduction band of channel should be minimized; ii) to develop the high-speed switching devices, the semiconductors should have enough carrier mobility, i.e., should not contain impurities, which trap charge carriers; iii) to have high on/off ratio, they should have an appropriate bandgap; iv) for high-degree of integration to develop electronic devices with outstanding electronic properties, each element in the FETs should have elaborate patterningability. Graphene can be used in various elements of flexible FETs due to its outstanding electrical, and mechanical properties. In this section, we consider use of graphene as the electrode or channel in FETs.

$R_{sh}$  of pristine SLG obtained using conventional wet transfer was  $\sim 270\text{ }\Omega/\text{sq}$ , and multi-layer stacking of SLG and additional HNO<sub>3</sub> doping resulted in  $R_{sh} < 50\text{ }\Omega/\text{sq}$  (Fig. 26a) [34], which is low enough for electrode application. Nevertheless, to achieve FETs

with superior electrical characteristics, the electrical properties of graphene should be improved. To improve the charge injection from electrode to channel in FETs, the  $\sim 4.4\text{ eV}$  WF of graphene should be modified to minimize the energy level mismatch between graphene and adjacent layers. At low temperature (1.6 K), both holes and electrons in graphene can have high  $\mu > 10^5\text{ cm}^2\text{ V}^{-1}\text{ s}^{-1}$ . Even at higher temperature,  $\mu$  is still high enough ( $>5 \times 10^4\text{ cm}^2\text{ V}^{-1}\text{ s}^{-1}$ ) for the graphene to be used in switching and logic devices; therefore, graphene is a promising candidate as a flexible channel material in high-speed FETs (Fig. 26b) [33]. However, pristine graphene has a zero bandgap, so FETs that have graphene as a channel have insufficient on/off ratio. For graphene to be applicable as a channel in FETs, a bandgap must be induced in it. Approaches to generate a bandgap in the electronic structure of graphene include physical and chemical treatments (i.e., oxidation [49,161,162], hydrogenation [163–166], substitutional doping [53,167], and nanoribbon formation [61,168–173]. Here, various FET demonstrations that use graphene as electrode and channel will be reviewed.

### 5.2. Graphene as an electrode for FETs

To use graphene electrodes for FETs, various synthesis strategies (e.g., rGO [174–176], CVD [22,177,178]) have been tested. rGO is prepared by dipping into a suspension of reduced graphene. Oxygen plasma of a hydrophobic Cytop™ fluoropolymer layer (5 nm) can be used to confine the electrode pattern. After plasma treatment, rGO suspension adheres selectively to the hydrophilic region, and forms electrodes. FETs are obtained by depositing pentacene on top of the rGO electrodes. FETs with rGO electrode had  $\mu = 0.03\text{ cm}^2\text{ V}^{-1}\text{ s}^{-1}$  [174].

Spin casting and pyrolysis can also be used to produce rGO electrodes. Repeated spin-casting yielded a 60-nm-thick GO film; pyrolysis of this film to remove oxygen-related functional groups left 20-nm-thick rGO electrodes. The rGO was patterned by depositing a sacrificial Al layer, treatment with oxygen plasma, then chemically etched to remove the Al. FETs were demonstrated by spin-coating of poly(3-hexylthiophene) (P3HT) on patterned rGO electrodes; these devices had hole mobility  $\mu_{\text{hole}} = 0.04\text{ cm}^2\text{ V}^{-1}\text{ s}^{-1}$  (Fig. 27a) [175]. However, rGO bears substantial numbers of defects, which substantially lower the conductivity of the electrodes, and thereby degrade the electrical properties of FETs.

To develop FETs based on a graphene electrode with an insignificant number of defects, CVD has been used to synthesize high-quality graphene electrodes [22,177–181]. Graphene was synthesized by CVD from CH<sub>4</sub> gas precursor with H<sub>2</sub> and Ar on Ni catalyst at  $>900\text{ }^\circ\text{C}$ , then patterned by depositing a sacrificial Ni layer, treating with oxygen plasma, then etching away the Ni layer to form electrodes. FETs were obtained by transferring the patterned electrode to substrate that had been treated with octadecyltrichlorosilane (OTS), then depositing a pentacene layer (60 nm) as a channel. FETs based on graphene electrode even showed superior electrical characteristics to a device with conventional Au electrodes [177]. A similar approach to achieve graphene electrode based FETs uses graphene synthesized by CVD on Cu foils, with CH<sub>4</sub>, and H<sub>2</sub> as the gas precursor [178]. However, the CVD process to synthesize graphene uses explosive gases (e.g., CH<sub>4</sub>, H<sub>2</sub>), and the method also requires transfer process of the graphene to the target substrate; this step slows the production of FETs. A novel strategy to solve these disadvantages uses coal tar pitch (CTP) as the carbon precursor (Fig. 27b) [22]. CTP was spin-cast on Si substrate, then a patterned Ni layer was deposited as a catalyst for graphene synthesis. Subsequent annealing under vacuum formed a patterned graphene electrode directly; by avoiding further patterning or transfer steps, this method can substantially increase productivity. FETs based on graphene

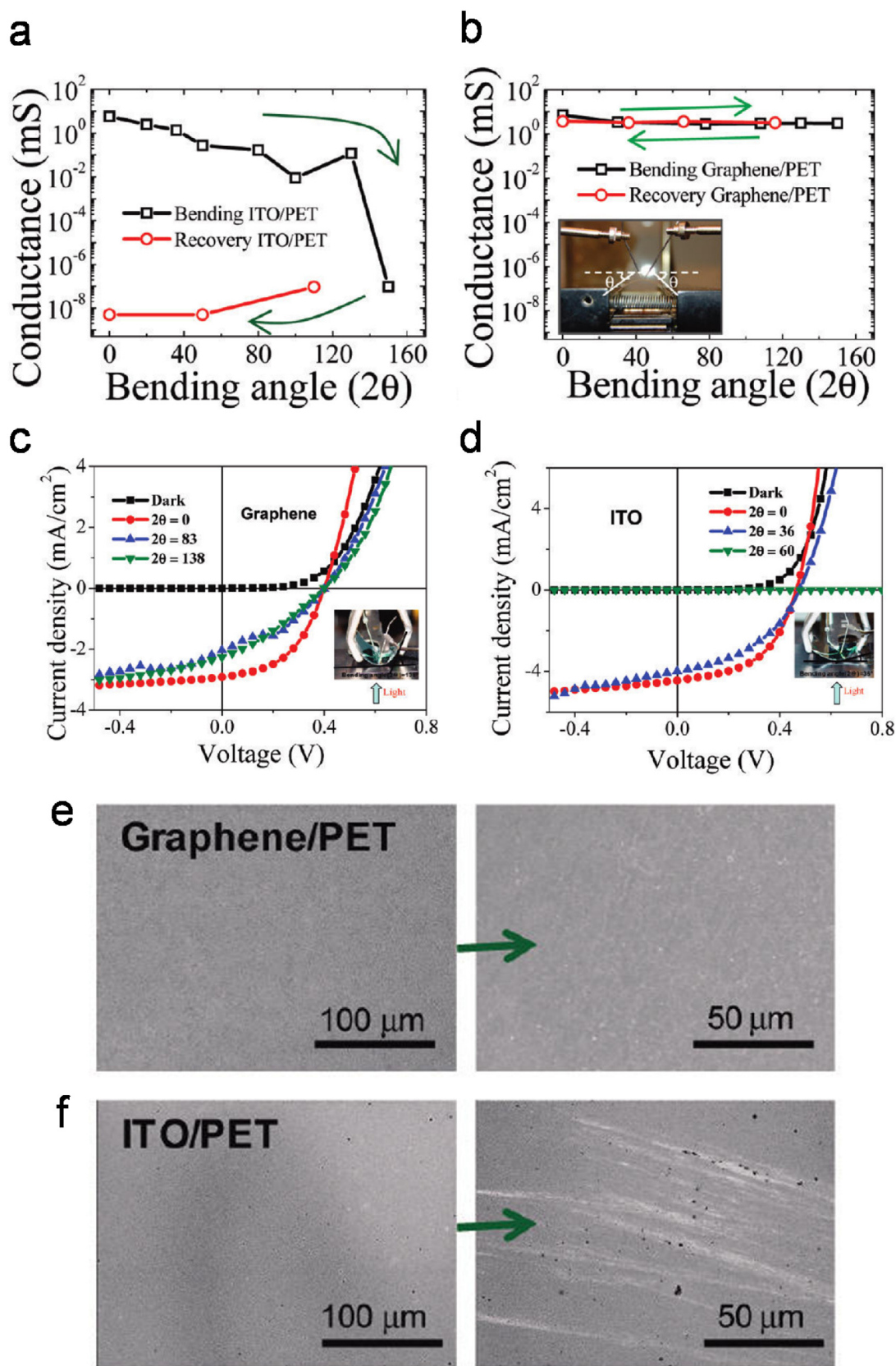


**Fig. 22.** Conductance of (a) PET/ITO and (b) PET/graphene films as a function of bending angle.  $J$ - $V$  characteristics of OSCs using (c) Graphene and (d) ITO electrodes by changing bending angle. SEM images of OSCs using (e) Graphene electrode and (f) ITO electrode on PET after being bent with the condition in (c) and (d). Reproduced from [143] Copyright 2010, American Chemical Society.

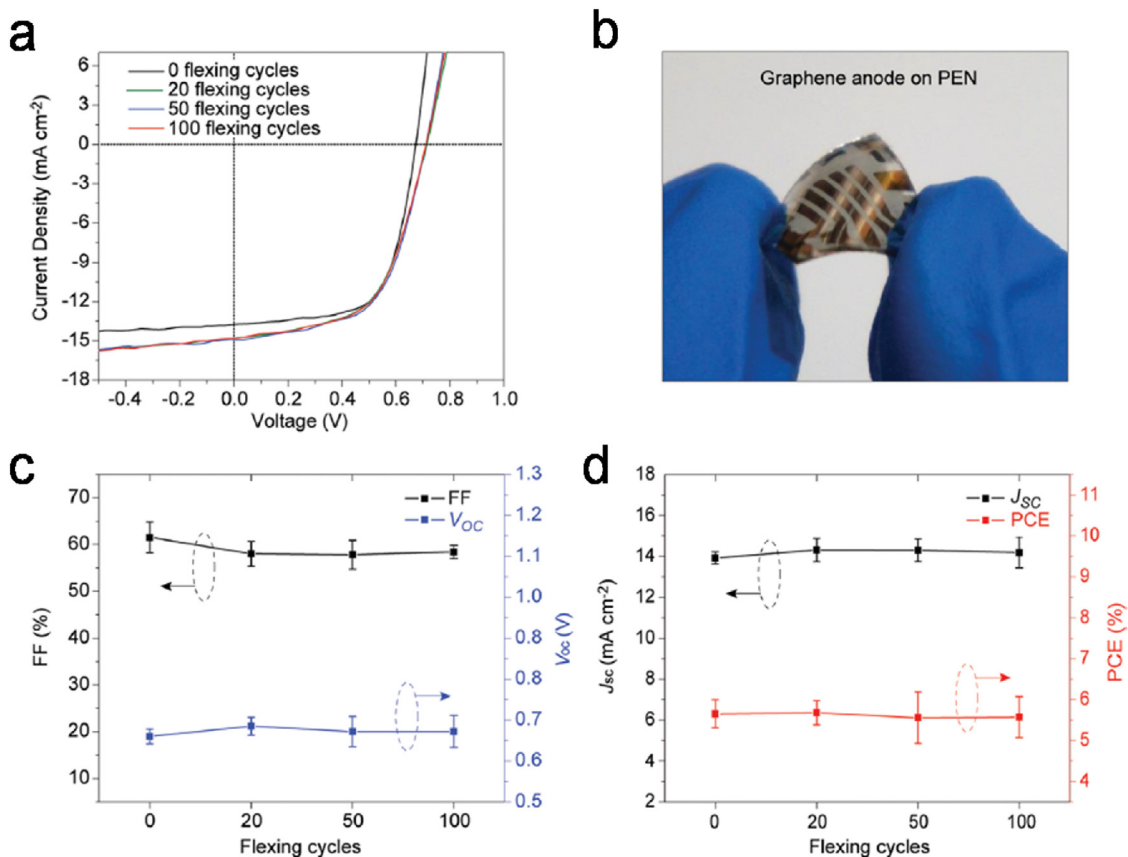


**Fig. 23.** (a)  $J$ - $V$  characteristics of flexible OSCs after repeated flexing cycle. (b) Image of flexible OSC device. Change in parameter of (c) FF and  $V_{oc}$  and (d)  $J_{sc}$  and PCE as a function of flexing cycles. Reproduced from [148] Copyright, 2014 American Chemical Society.

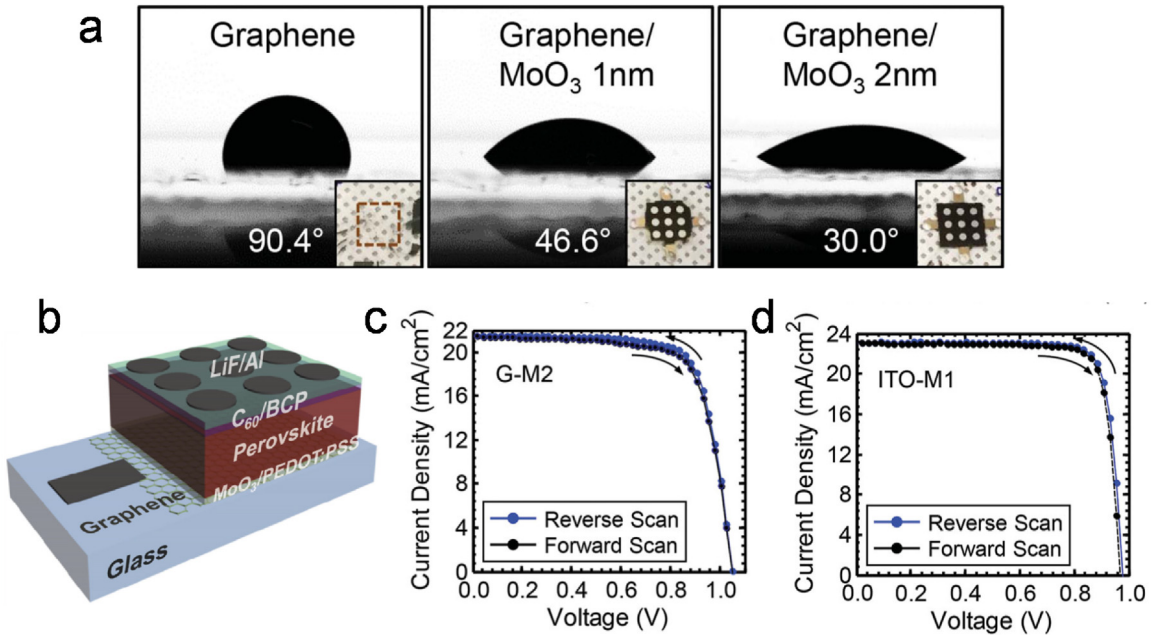


**Fig. 24.** (a) Contact angle of PEDOT:PSS on graphene and graphene with deposited MoO<sub>3</sub>. (b) Device structure using graphene electrode.  $J$ - $V$  characteristics of devices based on (c) graphene/MoO<sub>3</sub> (2 nm) and (d) ITO/MoO<sub>3</sub> (1 nm). Reproduced from [154] Copyright 2016, Wiley-VCH.

electrode were obtained by depositing a pentacene layer as a channel; they had higher  $\mu$  than did conventional FET devices with Au electrodes.

To improve the electrical characteristics of FETs, the WF of the electrode should be tailored to increase charge injection between electrodes and adjacent semiconducting layers. The energy-level

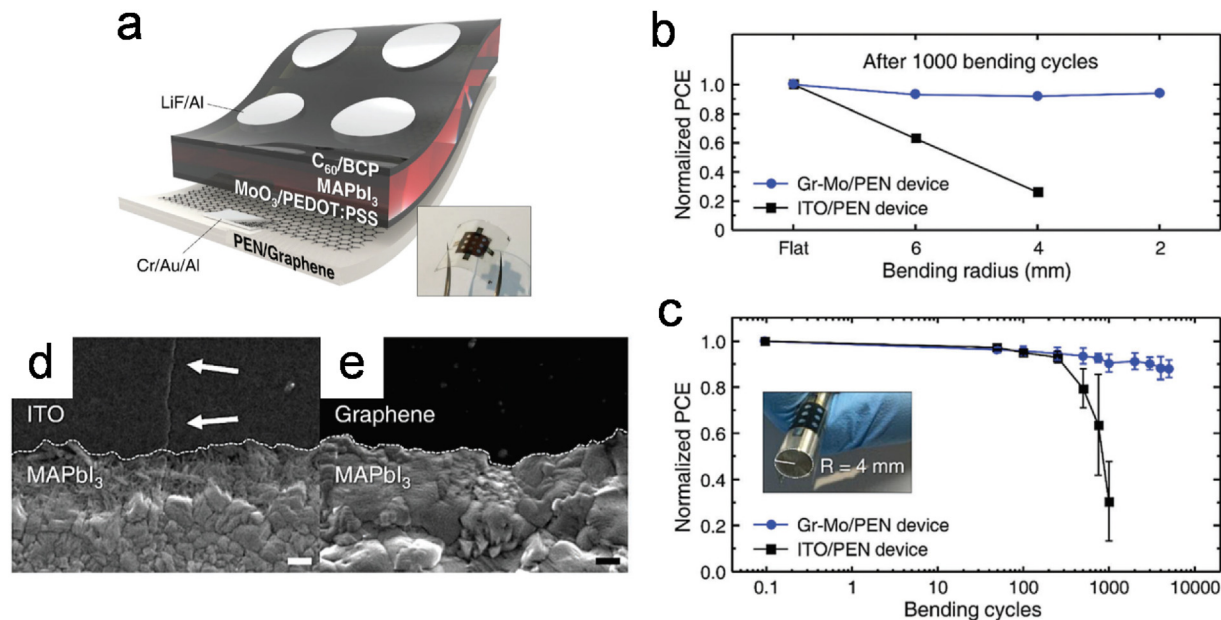


**Fig. 25.** (a) Schematic of flexible device structure using graphene electrode on PEN substrate (inset: image of real device). Change in normalized PCE of graphene and ITO devices as a function of (b) Bending radius and (c) Bending cycles. Cross-sectional SEM images of (d) ITO/MAPbI<sub>3</sub> that has a crack and (e) Graphene/MAPbI<sub>3</sub>. Reproduced from [155] Copyright 2017, The Royal Society of Chemistry.

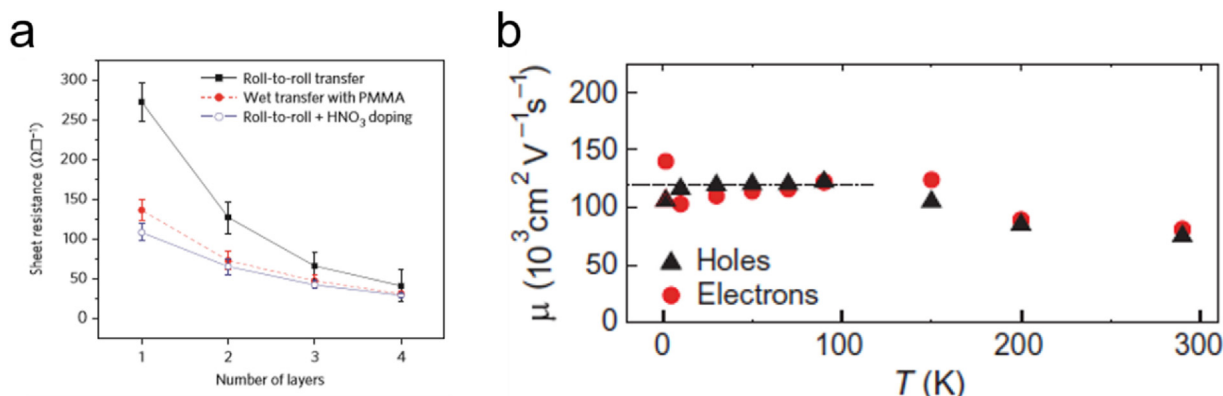


**Fig. 26.** (a) Sheet resistance change of graphene films with various transfer process according to the number of graphene layers. Reproduced from [34] Copyright 2010, Nature Publishing Group. (b) Charge mobility of graphene as a function of temperature. Reproduced from [33] Copyright 2015, American Association for the Advancement of Science.

difference between the electrodes and semiconductor forms a barrier to inject charge from metal to semiconductors, and thereby impede the FET's electrical characteristics. Various research on FETs based on a graphene electrode has modified the WF to reduce this barrier [179–181].

Another method to fabricate FETs with graphene electrodes is to float graphene with supporting polymers, and transfer it on an overturned substrate to a polymer layer between substrate and graphene (Fig. 28a). Three types of polymers (i.e. poly(vinyl-pyridine) (PVP), polybutadiene (PBu), and poly(vinyl chloride) (PVC)) have been used as the supporting layer; transferred graphene exhibited n-type doping on PVP, dedoping on PBu, and p-type doping on PVC. WF of the transferred graphene was 4.35 eV on PVP, 4.61 eV on PBu, and 4.8 eV on PVC. The WF on the PVC-intercalated graphene showed the smallest injection barrier (0.51 eV) among the three doped graphene electrodes, and FETs using PVC-supported graphene electrodes exhibited the most improved electrical transport characteristics in FETs (Fig. 28b) [179].

Application of a SAM is a simple method to control the work function of graphene electrodes in FETs. SAM can be easily patterned by using a photoresist as a blocking layer. Application of amine ( $-\text{NH}_2$ ) functional groups to the SAM induced intensive n-type doping characteristics: NH<sub>2</sub>-SAM treated graphene electrode had WF = 3.9 eV, which is 0.6 eV smaller than that of graphene on pristine SiO<sub>2</sub>. FETs based on graphene electrode were obtained by depositing N,N'-ditridecyl-3,4,9,10-perylenetetracarboxylic diimide. Due to the reduced electron injection barrier from NH<sub>2</sub>-SAM, FETs with n-type doped graphene electrode had superior electrical characteristics to those of FETs with graphene electrode on SiO<sub>2</sub> substrate (Fig. 28c-d) [180]. WF of rGO films can be directly modified by SAM treatment. rGO films have various oxygen-related functional groups (e.g., hydroxyl, epoxy, carboxyl), which induce formation of alkylsilanes by simple dipping in SAM solutions. rGO with a SAM that contained fluorinated alkyl groups had WF ~ 5.51 eV, and that of rGO with a SAM that contained NH<sub>2</sub> groups had WF ~ 4.31 eV; these results indicate that simple dipping in SAM solution can control the WF of rGO over a wide range (Fig. 28e-f).

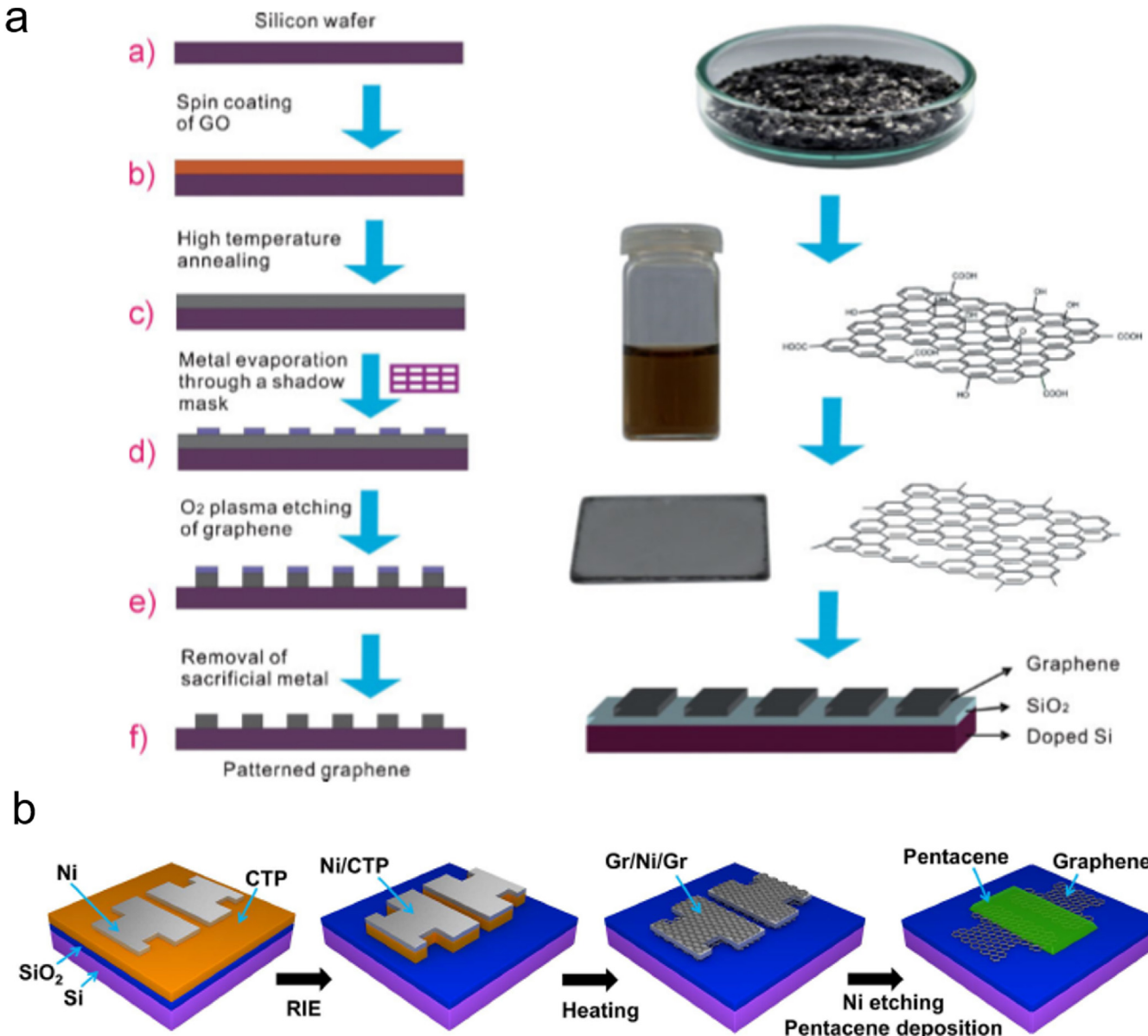


**Fig. 27.** Schematic illustration of (a) patterning process of rGO electrodes. Reproduced from [175] Copyright 2009, Wiley-CVH, and (b) fabrication process of FETs with CVD grown graphene using coal tar pitch. Reproduced from [22] Copyright 2015, Nature Publishing Group.

The SAM-doped rGO was used as source and drain electrodes in organic FETs that used poly[(9,9-dioctylfluorenyl-2,7-diyl)-co-bithiophene]. The FETs showed p-channel behavior, and FETs that had an electrode based on rGO doped with fluorinated alkyl, which has the highest WF, showed higher  $\mu$  and on/off ratio than the other FETs did [176].

Simple thermal annealing also can modify the WF of a graphene electrode [181]. Thermal treatment of graphene induces spontaneous charge transfer between graphene electrode and underlying silicon substrate; as a result the WF of graphene increases from 4.6 eV to 4.75 eV. The hole-injection energy barriers were 0.7 eV from pristine graphene to pentacene layer, and 0.6 eV from thermally-annealed graphene to pentacene layer.

These reports have proved that WF control of graphene electrode substantially improves the electrical properties of FETs. However, the reports have mainly focused on improving electrical properties of graphene. Before applications of

graphene electrode based FETs can be practical, research must be conducted to improve electrical properties and stability of modified graphene.

### 5.3. Graphene as channel for FETs

Graphene has a unique electronic structure in which valence bands and conduction bands meet at the Dirac point, so graphene has no bandgap. To achieve FETs with high on/off ratio for practical switching applications as channel elements, a bandgap must be induced in graphene. To accomplish this change, various methods have been tested, including oxidation [49,161,162], hydrogenation [163–166], substitutional doping [53,167], and graphene nanoribbon (GNR) formation [61,168–173].

Oxidation opens a bandgap in graphene [49,161,162]. UV-ozone treatment converts sp<sup>2</sup>-hybridized bonds in the pristine graphene to sp<sup>3</sup>-hybridized bonds, and induces oxygen-related chemical

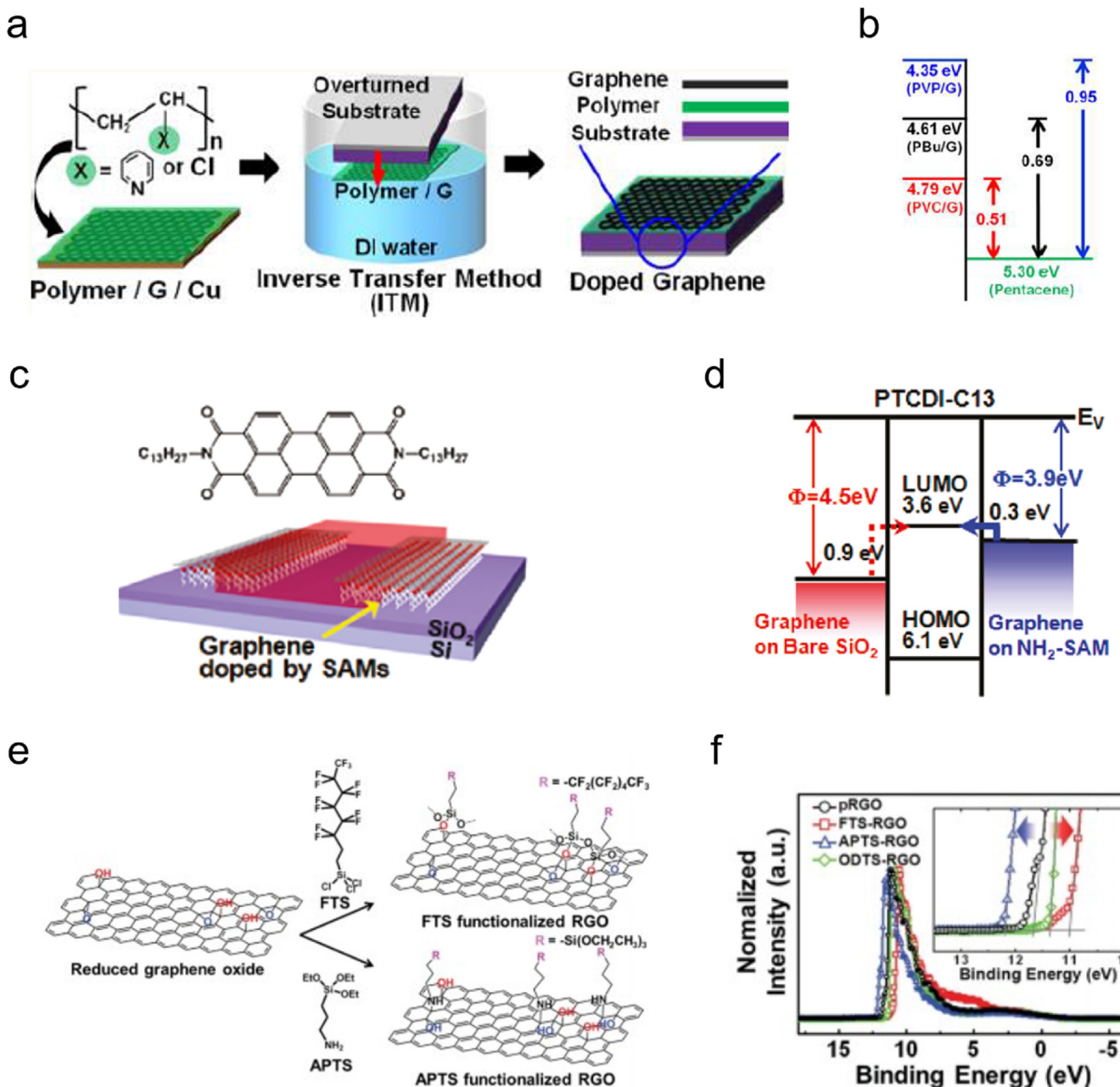


**Fig. 28.** Schematic diagram of (a) inverse transfer methods with various supporting polymers, (b) energy-level diagram of inversely transferred graphene and pentacene. Reproduced from [179] Copyright 2014, American Chemical Society (c) FETs with SAM-doped graphene electrodes, (d) energy-level diagram of bare, and NH<sub>2</sub>-SAM doped graphene electrode and PTCI-C13. Reproduced from [180] Copyright 2011, American Chemical Society, and (e) SAM functionalization of rGO with alkylsilanes and their chemical structures, (f) Ultraviolet photoelectron spectroscopy (UPS) of various SAM-treated rGO. Reproduced from [176] Copyright 2013, Wiley-VCH.

bonds, which induce open a bandgap in electronic structure of graphene and increase its  $R_{sh}$  and surface ionization potential [49]. Oxygen-plasma treatment also opens a bandgap in electronic structure of graphene; this process also disrupts sp<sup>2</sup> hybridization bonds between carbon atoms. Graphene with a bandgap obtained by O<sub>2</sub>-plasma treatment has been used as the channel in FETs [161]. O<sub>2</sub>-plasma treatment for <3.6 s yielded Ohmic characteristics, but treatment for >3.6 s resulted in non-linear behaviors, which indicate that a finite bandgap has formed.

Hydrogenation can also induce a bandgap in the electronic structure of graphene [182]. Methods include hydrogen plasma treatment, reaction with hydrogen silsesquioxane, and exposure to deuterium beams [165,166]. Hydrogen plasma treatments in vacuum condition at room temperature produces hydrogenated

graphene, which has been used successfully as the channel in FETs. Increased exposure time causes large coverage of hydrogenated graphene; hydrogen coverage saturated at ~25%. The hydrogenation increased a bandgap from 2.1 eV to 3.9 eV, which is high enough for FETs to have high on/off ratio. FETs that used hydrogenated graphene with a bandgap of ~3.9 eV on a dielectric of 100-nm-thick SiO<sub>2</sub> had on/off ratio >10<sup>3</sup> (Fig. 29a-c) [164].

Substitutional doping with heteroatoms also can induce a bandgap in graphene [53,167] by disrupting the symmetry of its lattice. Nitrogen-doped graphene prepared by CVD with CH<sub>4</sub> as graphene precursor, NH<sub>3</sub> as a dopant precursor, and Cu foil as the catalyst had significantly reduced electrical conductivity compared to pristine graphene. FETs produced using the Nitrogen-doped graphene had much higher on/off ratio (~840) than FETs produced

using pristine graphene; this difference indicates that barriers had formed between metal and graphene (Fig. 29d–e) [53].

A finite bandgap in graphene can be induced by GNR formation. Mechanically-exfoliated graphene sheets on  $\text{SiO}_2$  substrate were patterned by e-beam lithography and oxygen plasma treatment to yield GNRs with widths of 10–100 nm and lengths of 1–2  $\mu\text{m}$  [168]. FETs with GNRs were obtained by depositing Cr/Au (3/50 nm) (Fig. 30a). Contrary to bulk graphene film, GNRs with several-nanometer width showed a bandgap, which increased as the width of the GNRs decreased [168]. However, GNRs obtained using e-

beam lithography were wider than 10 nm, which is too wide to have sufficient bandgap for practical switching devices. Furthermore, e-beam lithography requires high production cost and long processing time.

Another lithographic attempt to generate a bandgap in graphene uses electro-hydrodynamic nanowire printing (Fig. 30b) [61,169,173]. This method has advantages of scalability, fast processing, low cost, and excellent patterning. Individually-controlled polyvinyl carbazole nanowires were printed on CVD-grown graphene as a patterned mask to protect the underlying

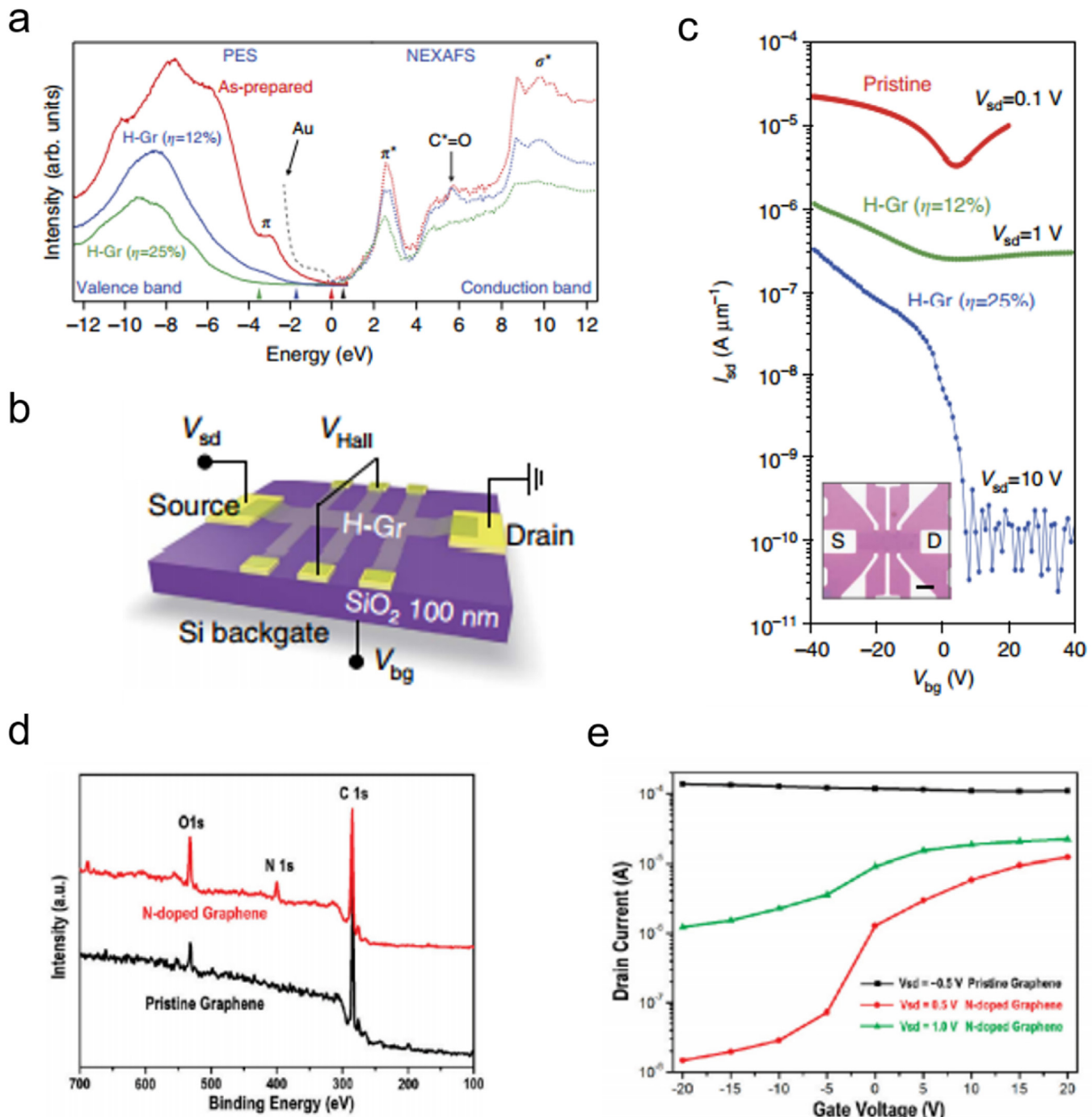


**Fig. 29.** (a) Synchrotron radiation X-ray photoemission spectroscopy and near-edge X-ray absorption fine structure spectroscopy of as-prepared and hydrogenated graphene, (b) Schematic diagram of FETs with hydrogenated graphene, (c) Current-voltage characteristics of FETs with pristine and hydrogenated graphene. Reproduced from [164] Copyright 2016, Nature Publishing Group. (d) X-ray photoelectron spectroscopy (XPS) spectra of pristine and N-doped graphene, (e) Current-voltage characteristics of FETs with pristine and N-doped graphene. Reproduced from [53] Copyright 2009, American Chemical Society.

graphene from oxygen plasma. The narrowest GNRs obtained were 9 nm. FETs that used the GNRs were fabricated by depositing an Au electrode on the nanowire-patterned graphene. Notably, this GNR fabrication method enabled exceptionally longer channel length ( $\geq 50 \mu\text{m}$ ) than conventional FETs with GNRs (less than several micrometers). At room temperature, FETs with the GNR had on/off ratio  $\sim 70$ , which indicates that a sufficient bandgap had been generated (Fig. 30c) [169].

Simple solution-processed chemical methods to produce GNRs have been demonstrated. Graphene that had been exfoliated from graphite was dispersed in a solution of poly(m-phenylenevinylene-co-2,5,-dioxy-p-phenylenevinylene) in 1,2-dichloroethane (Fig. 30d) [170]. GNRs were concentrated in the supernatant after centrifugation. Their widths ranged from  $\sim 50 \text{ nm}$  to  $< 10 \text{ nm}$  (Fig. 30e). FETs with GNR channel were fabricated by depositing Pd as source/drain metal contacts. The on/off ratio increased rapidly as the width of GNRs decreased; FETs with GNR  $< 10 \text{ nm}$  wide had on/off ratio  $> 10^5$ , which indicates is sufficient bandgap to be practical in switching devices. Bandgaps [eV] of GNRs with various

width [nm] can be estimated using as  $E_{\text{bandgap}} = 0.8/\text{width}$ , which adequately describes the on/off ratio increase with decrease of GNR width. This formula suggests that GNRs with width  $< 10 \text{ nm}$  have bandgap  $\sim 0.3 \text{ eV}$  (Fig. 30f–g).

Another GNR synthesis strategy can achieve uniform edges [171], and bottom-up synthesis on Au substrate can also yield precise edge structures [172]. By subliming 10,10'-dibromo-9,9'-bianthryl on Au substrate, precursors polymerized by forming radicals. Thermal treatment of the polymerized precursor on the Au surface caused repeated C-C coupling and dehydrogenation, so GNRs formed (Fig. 30h). GNRs obtained by this bottom-up synthesis were transferred to  $\text{SiO}_2$  substrate. PMMA was spin-cast on GNRs synthesized on Au/mica substrate. Delaminating the mica, then etching away the Au with HF yielded floating PMMA-supported GNR films. Rinsing, transferring the GNRs/PMMA film to a dielectric substrate and removing the PMMA yielded GNRs on the substrate. FETs with these GNRs were demonstrated by depositing patterned Pd on GNRs. FETs with negligible hysteresis were achieved by post-treatment, including annealing and

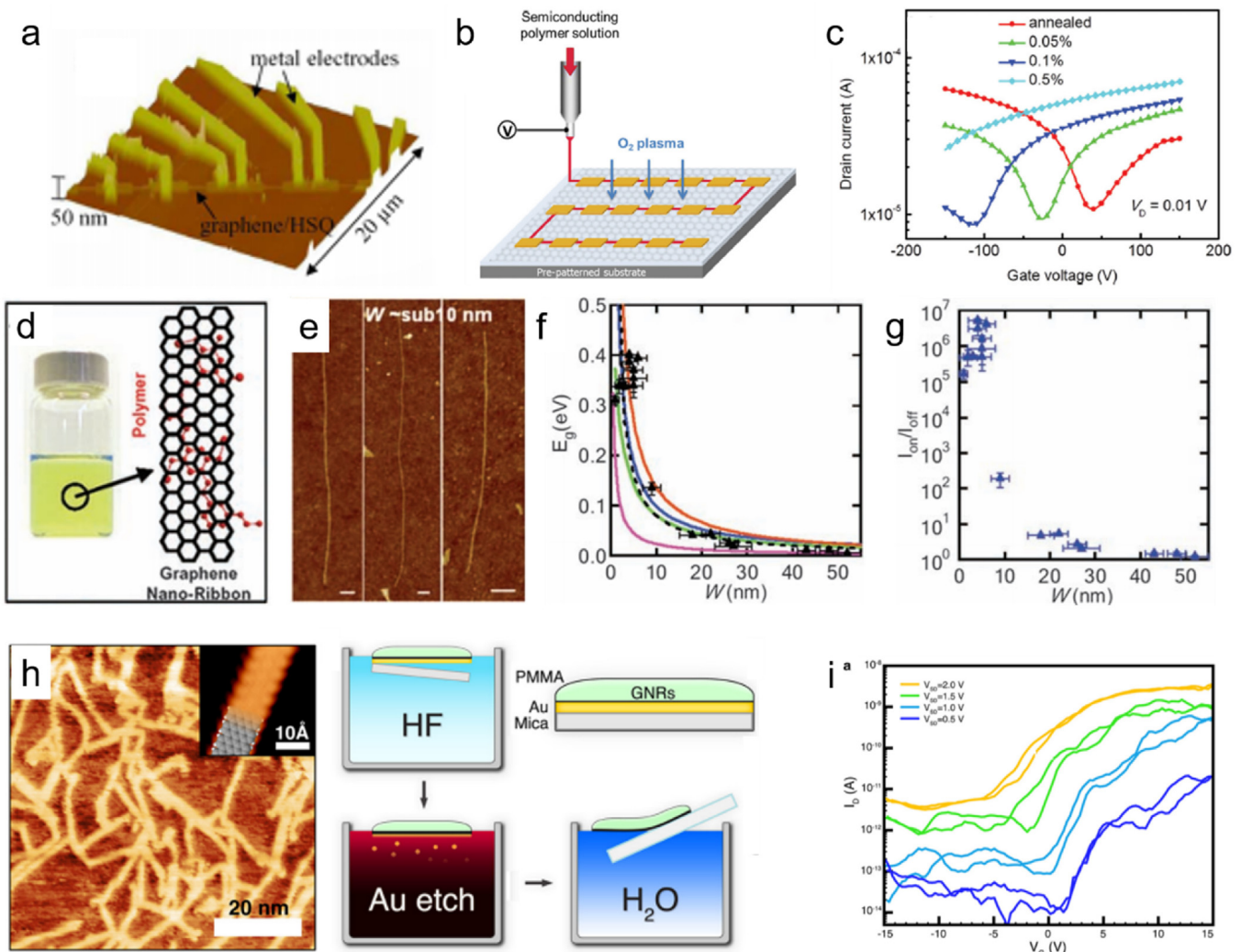


**Fig. 30.** (a) Atomic force microscopy image of GNRs with etching mask. Reproduced from [168] Copyright 2007, American Physical Society (b) Schematic illustration of the FETs with GNR using electro-hydrodynamic nanowire printing and  $\text{O}_2$  plasma treatment, (c) Current-voltage characteristics of FETs with various GNRs. Reproduced from [61] Copyright 2015, Wiley-CVH (d) Photograph of GNR suspended solution (left), and schematics of GNRs demonstrated from suspension (e) GNRs with heights  $< 2 \text{ nm}$ . (Scale bars: 100 nm) (f) Calculated energy gap for GNRs with various width, (g) On/off ratio of FETs with various GNR widths. Reproduced from [170] Copyright 2008, American Association for the Advancement of Science (h) Scanning tunneling microscopy image of GNRs on Au substrate (inset: high-resolution image of GNRs with low-temperature STM) (left), and schematic illustration of GNR transfer on target substrate (right), (i) Current-voltage characteristics of FETs with the bottom-up synthesized GNRs. Reproduced from [171] Copyright 2013, American Physical Society.

hexamethyldisilazane passivation. The FET with GNRs had on-off ratio  $\sim 3.6 \times 10^3$  at  $1\text{ V}_{SD}$  (Fig. 30i).

## 6. Flexible encapsulation using graphene

### 6.1. Requirements of encapsulant for flexible electronics

Although organic electronics have been advancing to replace inorganic electronics [5,6,183–188], organic molecules are susceptible to oxygen and moisture, so organic devices should be passivated to prevent degradation of organic materials in device. The most widely-used method to encapsulate organic electronics is to use hollow glass encapsulant with UV-curable epoxy resin, but this approach must be done under  $\text{N}_2$  atmosphere, and requires getters to trap the trace  $\text{O}_2$ ,  $\text{H}_2\text{O}$  and other reactive gases [189]. Several other encapsulation technologies have been proposed; these include using atomic layer deposition (ALD) to lay down an inorganic film [190,191], and coating an organic layer [192]. ALD is a self-limiting surface reaction, and provides a nearly pinhole-free atom-thick coating, and therefore provides outstanding barrier properties [193]. However, ALD entails high processing cost due to the necessity of high vacuum and long processing time [183]. Especially, conventional glass encapsulation and layers produced using ALD are brittle, and therefore are not suitable as flexible

encapsulation methods. Organic polymers have also been evaluated as encapsulants of OLEDs [192]. Organic polymers can form barriers without reducing the flexibility of organic electronics, but these polymers have poor barrier capacity, and direct contact between the barrier solution and the organic device can result in contamination, which can severely degrade the devices.

Flexible encapsulation for organic electronics should meet several requirements: i) outstanding barrier properties comparable to conventional inorganic film or glass encapsulation, ii) roll-to-roll processability for low processing cost, and iii) contamination-free process.

### 6.2. Flexible encapsulation using graphene

Graphene has outstanding barrier properties against gas and liquid due to its densely-packed lattice structure [194–196]. Molecular permeation characteristic of GO produced using Hummer's method has been investigated (Fig. 31a–b) [195]. A 0.5- $\mu\text{m}$ -thick GO film did not allow any leakage of He, whereas a 12- $\mu\text{m}$ -thick PET film allowed a large amount of He leakage. The 12- $\mu\text{m}$ -thick PET film was 1000 times more permeable than the GO-film; this difference indicates that GO film has superior barrier characteristics. Graphene grown by CVD with Cu or Ni film also has barrier properties (Fig. 31c–e) [196]. In contrast to pristine Cu film,

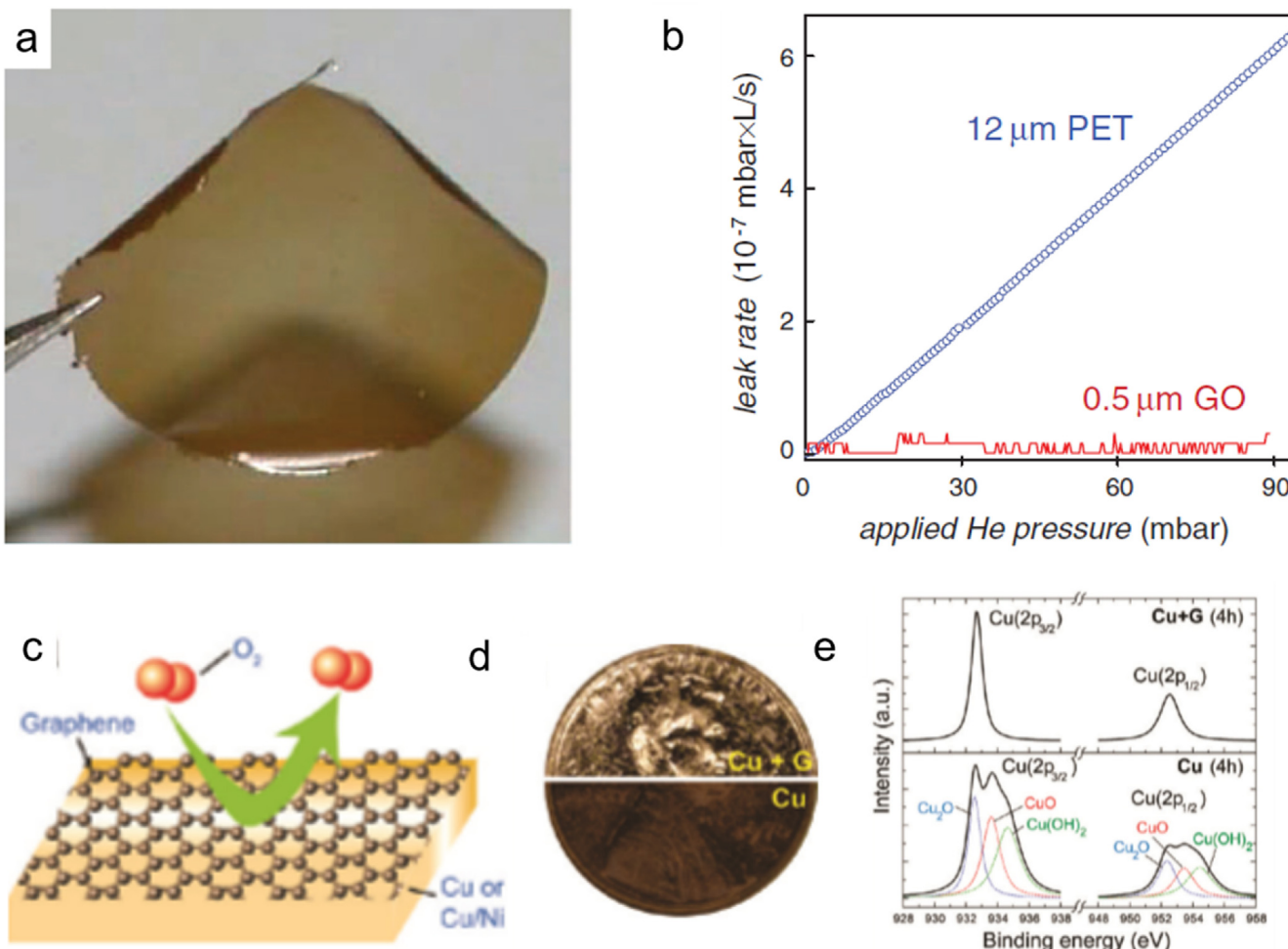


**Fig. 31.** (a) Photograph of prepared GO film, (b) He-leak measurement of PET and 0.5- $\mu\text{m}$ -thick GO film. Reproduced from [195] Copyright 2012, American Association for the Advancement of Science (c) Schematics describing the barrier properties of graphene, (d) Photograph of graphene coated (upper), and uncoated (lower) after  $\text{H}_2\text{O}_2$  exposure, (e) XPS spectra of graphene/Cu, and Cu after annealing in air. Reproduced from [196] Copyright 2011, American Chemical Society.

Cu film coated with grown graphene maintained its metallic properties under reactive  $H_2O_2$  treatment. Also in contrast to pristine Cu, which showed various oxygen-related peaks in XPS spectra, graphene-protected Cu showed no oxygen-related XPS spectra; this result indicates that CVD-grown graphene offers an excellent barrier film on metals.

Due to their promising barrier properties, graphene and GO have been used to encapsulate organic materials based devices [23,197–199]. Solution-processed GO and rGO were used to encapsulate OPVs [198]. Gas-barrier properties of GO and rGO films were examined by measuring the  $T$  change of P3HT. Deposited GO film can prevent photo-oxidation, which causes increase in  $T$ . As thickness of GO film increased from 10 nm to 20 nm,  $T$  change was reduced; this trend indicates that the barrier properties improved. Thermal annealing at 150 °C converted GO to rGO, and thereby further improved the barrier properties, even though the thickness of barrier film was decreased to 15 nm. This increase occurred because thermal annealing restored the graphene lattice and decreased the interlayer spacing between the rGO layers (Fig. 32a–c). In ambient conditions, rGO-passivated OPVs were more stable than GO-passivated OPVs. After 50 h, GO- and rGO- encapsulated OPVs had ~20% higher PCE than OPVs without encapsulation (Fig. 32d); this result proves that GO and rGO films can provide a gas barrier on organic electronics.

Flexible OPVs that are based on flexible PI substrate, and that are passivated with CVD-grown graphene have been demonstrated [197]. CVD-grown graphene has been used for top electrode and passivation layer at the same time. Absence of an additional capping layer led to the development of ultra-thin OPVs with excellent tolerance to bending. By adding one or more layers of graphene, the stability in ambient conditions was dramatically improved, and the PCEs of the OPVs were almost maintained for >70 d. Water vapor transmission rate (WVTR) of CVD-grown graphene on PET film decreased as the number of graphene layers increased (Fig. 32e) [199]. PET film with six-layer graphene had WVTR = 0.48 g m<sup>-2</sup> d<sup>-1</sup>. These encapsulation films were used in pentacene-based FETs to investigate the barrier characteristics (Fig. 32f). Under UV/ozone treatment, pentacene layers were stably maintained without oxidation. At 60 °C and 60 % relative humidity, pentacene layers passivated with the graphene-based encapsulant showed less decrease of  $\mu$  than non-encapsulated FETs did. Moreover, the barrier properties on encapsulated FETs remained stable after 500 bending cycles (Fig. 32g). However, direct deposition of graphene encapsulation films on organic layers can cause contamination, which can degrade the electrical characteristics of organic devices. Direct scooping of floating graphene to encapsulate the organic electronics exposes underlying organic layer faces to highly-concentrated moisture, which causes severe degradation.

Free-standing CVD-grown graphene films on PET have been used to encapsulate polymer LEDs [23]. LEDs on PET substrate were laminated with repeatedly-stacked CVD-grown graphene and polydimethylsiloxane (PDMS) insulator (Fig. 32h). As the number of stacked graphene layers increased, the half-luminescence lifetimes ( $L_{50}$ ) increased (Fig. 32i). Bare PET and PET with PDMS film had  $L_{50} < 20$  h, but PET with PDMS and six layers of graphene had  $L_{50} > 70$  h. Ca test were also performed to investigate the barrier properties of the encapsulants (Fig. 32j). PET film with PDMS and six layers of graphene showed the lowest WVTRs; this result confirms the outstanding barrier properties of the flexible encapsulant composed of PDMS with six-layered CVD-grown graphene. Flexible encapsulation was successfully demonstrated by using the graphene-PDMS based barrier film on large-area flexible polymer LEDs (Fig. 32k).

## 7. Conclusion and outlook

This work has reviewed recent progress in graphene-based flexible electronics, including flexible LEDs, SCs and FETs, and has also considered use of graphene as an encapsulant. Graphene can provide various advantages for flexible electronics; these include high  $T$ , high electron mobility, and mechanical robustness. Therefore, graphene has been evaluated for use as various components in flexible electronics. However, several disadvantages of graphene must be solved before it can be used in practical flexible electronics. Pristine graphene's relatively high  $R_{sh}$  limits current in devices at a given applied bias, and its inappropriate WF (~4.4 eV) can form a large energy barrier to charge injection in FETs and LEDs, and can lead to voltage loss in SCs. Pristine graphene has no bandgap, so it is not appropriate for use as a channel in FETs. Various ways to modify the electrical properties of pristine graphene have been developed; these include development of synthesis methods and chemical or physical modifications of graphene. Development of large-scale graphene production by CVD has significantly increased the feasibility of graphene-based flexible electronic devices compared with graphene film formed by mechanical or chemical exfoliation of graphite. Various methods to dope graphene have been used to achieve desirable  $R_{sh}$  and WF for improved charge conduction in devices, or to open the band gap of graphene for use as a channel in FETs. These methods have increased luminous efficiency in LEDs, PCE in SCs, and on-off ratio in switching devices. Various methods have been introduced to form a finite band gap in graphene; these include such as oxidation, hydrogenation, and GNR formation. Interfacial layers on graphene electrode also substantially increase the electrical or luminous properties of devices by reducing the large energy barrier to charge injection from the graphene electrode in flexible electronics. Graphene has also been shown to be an effective flexible encapsulant due to its densely-packed structure and outstanding impermeability to gas molecules.

Further development of graphene-based flexible electronics requires development of (1) a method to synthesize high-quality graphene that is free of defects and is composed of large single-crystal domains, and (2) a graphene-transfer process to obtain smooth surface of graphene film and to form defect-free, residue-free graphene film on desired substrates. Study on graphene doping to increase electrical conductivity and work function should be continued. At the same time, development of an interfacial layer on graphene may provide a way to alter electrical properties of pristine graphene without sacrificing its unique properties, and to align energy levels to facilitate charge carrier injection from graphene to overlying functional layers. New strategies to obtain defect-free and high-quality graphene and development of engineering methods to improve properties of graphene would facilitate development of next-generation flexible electronics. Importantly, enhancement of mechanical properties of graphene is more required for stretchable electronics. However, only 6% stretching was allowed without change in  $R_{sh}$  of graphene because the strong carbon networks which give high stiffness and elastic modulus limit dissipation of strain energy [39]. To overcome the limited stretchability of graphene itself, various approaches to increase stretchability of graphene have been developed to make it suitable for stretchable applications that demand durability for stretching to 20–30% [200]; stacking graphene layers [201], making composite with metal nanowires [42,202], and using pre-strained substrates [39] have been suggested. Therefore, to make use of graphene feasible in next-generation stretchable and wearable electronics, new ways to improve stretchability of graphene-based electrodes or encapsulants must be developed.

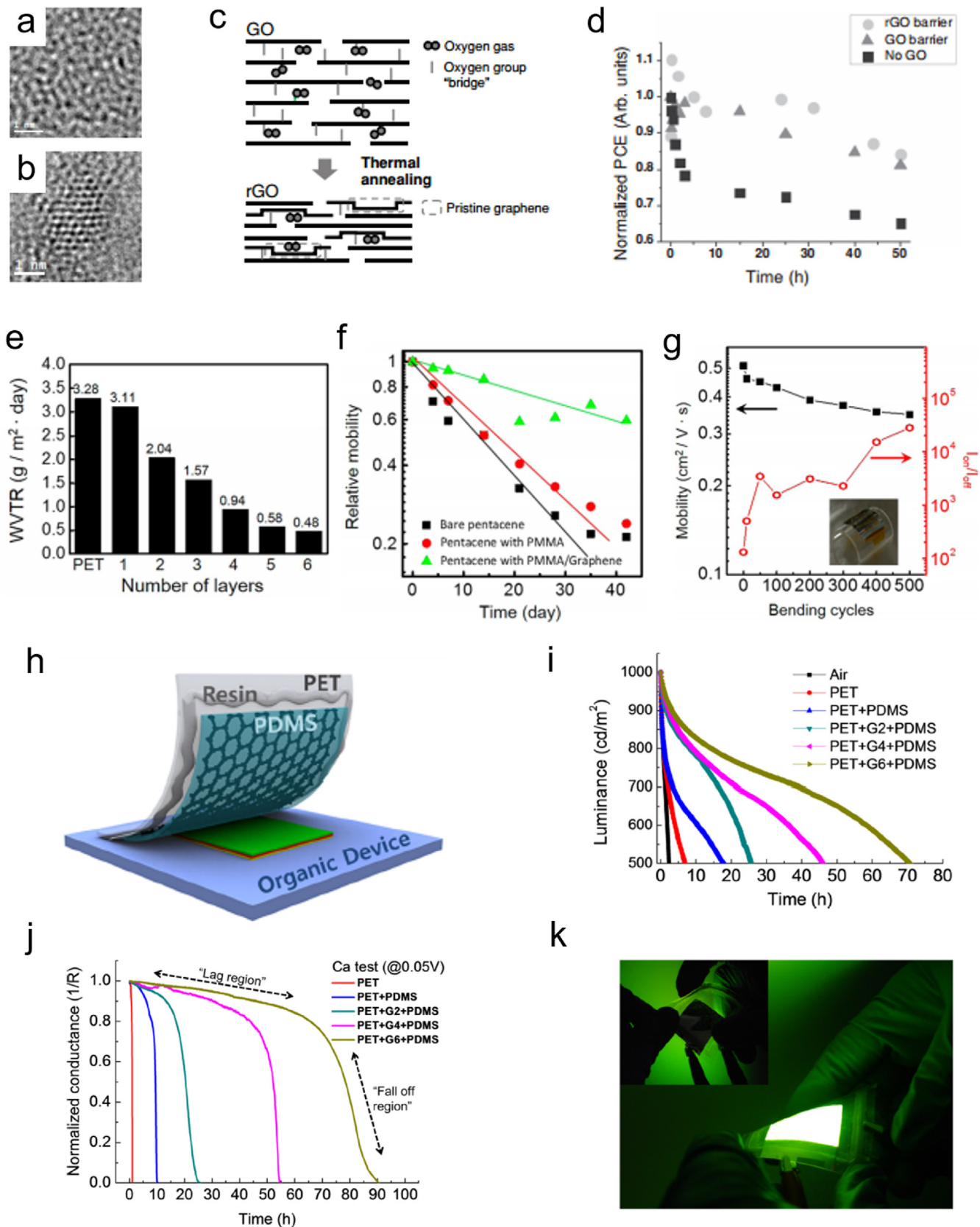


**Fig. 32.** High-resolution transmission electron microscopy images of (a) GO, and (b) rGO films, (c) Schematic illustration of O<sub>2</sub> permeation through GO (upper) and rGO (lower) film, (d) Normalized PCE changes of OSCs encapsulated with GO, rGO in ambient. Reproduced from [198] Copyright 2014, Wiley-CVH (e) WVTR of graphene film according to the number of transferred graphene layer on PET (f) Carrier mobility changes of FETs with bare pentacene, PMMA passivated pentacene, and PMMA/Graphene passivated pentacene at 60 °C and 60 % relative humidity. (g) Carrier mobility and on/off ratio changes of PMMA/graphene passivated FETs under bending cycles. Reproduced from [199] Copyright 2015, American Chemical Society (h) Schematic illustration of PDMS/graphene/PET encapsulated organic device, (i) Luminance change of OLEDs encapsulated with various passivation films in ambient condition, (j) Normalized conductance change of various passivation films, measured using a Ca test, (k) Photograph demonstrating large-area flexible encapsulation of OLEDs (emitting area: 3 cm × 3 cm). Reproduced from [23] Copyright 2016, American Chemical Society.

## Acknowledgements

This research was supported by the Nano Material Technology Development Program through the National Research Foundation of Korea (NRF) funded by the Ministry of Science, ICT & Future Planning (MSIP, Korea) (NRF-2014M3A7B4051747). Also, this work was supported by the National Research Foundation of Korea (NRF) grant funded by the Korea government (Ministry of Science, ICT & Future Planning) (NRF-2016R1A3B1908431).

## References

- [1] J.-H. Ahn, B.H. Hong, *Nat. Nanotechnol.* 9 (2014) 737–738.
- [2] F. Bonaccorso, Z. Sun, T. Hasan, A.C. Ferrari, *Nat. Photon.* 4 (2010) 611–622.
- [3] S.J. Kim, K. Choi, B. Lee, Y. Kim, B.H. Hong, *Annu. Rev. Mater. Res.* 45 (2015) 63–84.
- [4] S.R. Forrest, M.E. Thompson, *Chem. Rev.* 107 (2007) 923–925.
- [5] J.A. Rogers, T. Someya, Y. Huang, *Science* 327 (2010) 1603–1607.
- [6] T. Sekitani, T. Someya, *Adv. Mater.* 22 (2010) 2228–2246.
- [7] A. Kumar, C. Zhou, *ACS Nano* 4 (2010) 11–14.
- [8] I. Hamberg, C.G. Granqvist, *J. Appl. Phys.* 60 (1986) R123–R160.
- [9] C.G. Granqvist, *Sol. Energy Mater. Sol. Cells* 91 (2007) 1529–1598.
- [10] K.A. Sierras, N.J. Morris, S.N. Kukureka, D.R. Cairns, *Wear* 267 (2009) 625–631.
- [11] D.R. Cairns, R.P. Witte, D.K. Sparacinc, S.M. Sachsmann, D.C. Paine, G.P. Crawford, R.R. Newton, *Appl. Phys. Lett.* 76 (2000) 1425–1427.
- [12] T.-H. Han, Y. Lee, M.-R. Choi, S.-H. Woo, S.-H. Bae, B.H. Hong, J.-H. Ahn, T.-W. Lee, *Nat. Photon.* 6 (2012) 105–110.
- [13] E.C.-W. Ou, L. Hu, G.C.R. Raymond, O.K. Soo, J. Pan, Z. Zheng, Y. Park, D. Hecht, G. Irvin, P. Drzaic, G. Gruner, *ACS Nano* 3 (2009) 2258–2264.
- [14] Z. Yu, Q. Zhang, L. Li, Q. Chen, X. Niu, J. Liu, Q. Pei, *Adv. Mater.* 23 (2011) 664–668.
- [15] M. Cai, Z. Ye, T. Xiao, R. Liu, Y. Chen, R.W. Mayer, R. Biswas, K.-M. Ho, R. Shinar, J. Shinar, *Adv. Mater.* 24 (2012) 4337–4342.
- [16] M. Schaefer, F. Nüesch, D. Berner, W. Leo, L. Zuppiroli, *Adv. Funct. Mater.* 11 (2001) 116–121.
- [17] D. Li, E.-J. Borkent, R. Nortrup, H. Moon, H. Katz, Z. Bao, *Appl. Phys. Lett.* 86 (2005) 42105.
- [18] H. Yang, L. Yang, M.-M. Ling, S. Lastella, D.D. Gandhi, G. Ramanath, Z. Bao, C.Y. Ryu, *J. Phys. Chem. C* 112 (2008) 16161–16165.
- [19] K. Kim, S.-H. Bae, C.T. Toh, H. Kim, J.H. Cho, D. Whang, T.-W. Lee, B. Özyilmaz, J.-H. Ahn, *ACS Appl. Mater. Interfaces* 6 (2014) 3299–3304.
- [20] H. Kim, S.-H. Bae, T.-H. Han, K.-G. Lim, J.-H. Ahn, T.-W. Lee, *Nanotechnology* 25 (2014) 14012.
- [21] C. Mattevi, F. Colléaux, H. Kim, Y.-H. Lin, K.T. Park, M. Chhowalla, T.D. Anthopoulos, *Nanotechnology* 23 (2012) 344017.
- [22] H.-K. Seo, T.-S. Kim, C. Park, W. Xu, K. Baek, S.-H. Bae, J.-H. Ahn, K. Kim, H.C. Choi, T.-W. Lee, *Sci. Rep.* 5 (2015) 16710.
- [23] H.-K. Seo, M.-H. Park, Y.-H. Kim, S.-J. Kwon, S.-H. Jeong, T.-W. Lee, *ACS Appl. Mater. Interfaces* 8 (2016) 14725–14731.
- [24] A.K. Geim, K.S. Novoselov, *Nat. Mater.* 6 (2007) 183–191.
- [25] J.A. Rogers, *Nat. Nanotechnol.* 3 (2008) 254–255.
- [26] K.S. Novoselov, A.K. Geim, S.V. Morozov, D. Jiang, Y. Zhang, S.V. Dubonos, I.V. Grigorieva, A.A. Firsov, *Science* 306 (2004) 666–669.
- [27] Y. Zhang, Y.-W. Tan, H.L. Stormer, P. Kim, *Nature* 438 (2005) 201–204.
- [28] M.I. Kattnelson, *Mater. Today* 10 (2007) 20–27.
- [29] K.S. Novoselov, Z. Jiang, Y. Zhang, S.V. Morozov, H.L. Stormer, U. Zeitler, J.C. Maan, G.S. Boebinger, P. Kim, A.K. Geim, *Science* 315 (2007) 1379–1379.
- [30] Z. Jiang, Y. Zhang, H.L. Stormer, P. Kim, *Phys. Rev. Lett.* 99 (2007) 106802.
- [31] R.R. Nair, P. Blake, A.N. Grigorenko, K.S. Novoselov, T.J. Booth, T. Stauber, N.M. R. Peres, A.K. Geim, *Science* 320 (2008) 1308–1308.
- [32] C. Lee, X. Wei, J.W. Kysar, J. Hone, *Science* 321 (2008) 385–388.
- [33] L. Banszerus, M. Schmitz, S. Engels, J. Dauber, M. Oellers, F. Haupt, K. Watanabe, T. Taniguchi, B. Beschoten, C. Stampfer, *Sci. Adv.* 1 (2015) e1500222.
- [34] S. Bae, H. Kim, Y. Lee, X. Xu, J.-S. Park, Y. Zheng, J. Balakrishnan, T. Lei, H. Ri Kim, Y. Il Song, Y.-J. Kim, K.S. Kim, B. Özyilmaz, J.-H. Ahn, B.H. Hong, S. Iijima, *Nat. Nanotechnol.* 5 (2010) 574–578.
- [35] R. Van Noorden, *Nature* 483 (2012) S32–S33.
- [36] W.S. Hummers, R.E. Offeman, *J. Am. Chem. Soc.* 80 (1958) 1339.
- [37] D. Li, M.B. Muller, S. Gilje, R.B. Kaner, G.G. Wallace, *Nat. Nanotechnol.* 3 (2008) 101–105.
- [38] G. Eda, G. Fanchini, M. Chhowalla, *Nat. Nanotechnol.* 3 (2008) 270–274.
- [39] K.S. Kim, Y. Zhao, H. Jang, S.Y. Lee, J.M. Kim, K.S. Kim, J.-H. Ahn, P. Kim, J.-Y. Choi, B.H. Hong, *Nature* 457 (2009) 706–710.
- [40] X. Li, W. Cai, L. Colombo, R.S. Ruoff, *Nano Lett.* 9 (2009) 4268–4272.
- [41] S. Stankovich, D.A. Dikin, G.H.B. Dommett, K.M. Kohlhaas, E.J. Zimney, E.A. Stach, R.D. Piner, S.T. Nguyen, R.S. Ruoff, *Nature* 442 (2006) 282–286.
- [42] M.-S. Lee, K. Lee, S.-Y. Kim, H. Lee, J. Park, K.-H. Choi, H.-K. Kim, D.-G. Kim, D.-Y. Lee, S. Nam, J.-U. Park, *Nano Lett.* 13 (2013) 2814–2821.
- [43] M.P. de Jong, L.J. van, I. Jzendoorn, M.J.A. de Voigt, *Appl. Phys. Lett.* 77 (2000) 2255–2257.
- [44] S.T. Lee, Z.Q. Gao, L.S. Hung, *Appl. Phys. Lett.* 75 (1999) 1404–1406.
- [45] K.W. Wong, H.L. Yip, Y. Luo, K.Y. Wong, W.M. Lau, K.H. Low, H.F. Chow, Z.Q. Gao, W.L. Yeung, C.C. Chang, *Appl. Phys. Lett.* 80 (2002) 2788–2790.
- [46] A. Sharma, G. Andersson, D.A. Lewis, *Phys. Chem. Chem. Phys.* 13 (2011) 4381–4387.
- [47] T.S. Bejjital, D. Compton, K.A. Sierras, D.R. Cairns, S.N. Kukureka, *Thin Solid Films* 528 (2013) 229–236.
- [48] T.-H. Han, S.-J. Kwon, N. Li, H.-K. Seo, W. Xu, K.S. Kim, T.-W. Lee, *Angew. Chem. Int. Ed.* 55 (2016) 6197–6201.
- [49] T.-H. Han, S.-J. Kwon, H.-K. Seo, T.-W. Lee, *2D Mater.* 3 (2016) 014003.
- [50] H. Cho, S.D. Kim, T.-H. Han, I. Song, J.-W. Byun, Y.-H. Kim, S. Kwon, S.-H. Bae, H. C. Choi, J.-H. Ahn, T.-W. Lee, *2D Mater.* 2 (2015) 014002.
- [51] L.S. Panchakarla, K.S. Subrahmanyam, S.K. Saha, A. Govindaraj, H.R. Krishnamurthy, U.V. Waghmare, C.N.R. Rao, *Adv. Mater.* 21 (2009) 4726–4730.
- [52] P.A. Denis, *Chem. Phys. Lett.* 492 (2010) 251–257.
- [53] D.C. Wei, Y.Q. Liu, Y. Wang, H.L. Zhang, L.P. Huang, G. Yu, *Nano Lett.* 9 (2009) 1752.
- [54] H. Wang, Y. Zhou, D. Wu, L. Liao, S. Zhao, H. Peng, Z. Liu, *Small* 9 (2013) 1316–1320.
- [55] R. Lv, Q. Li, A.R. Botello-Méndez, T. Hayashi, B. Wang, A. Berkdemir, Q. Hao, A. L. Elías, R. Cruz-Silva, H.R. Gutiérrez, Y.A. Kim, H. Muramatsu, J. Zhu, M. Endo, H. Terrones, J.-C. Charlier, M. Pan, M. Terrones, *Sci. Rep.* 2 (2012).
- [56] F. Güneş, H.-J. Shin, C. Biswas, G.H. Han, E.S. Kim, S.J. Chae, J.-Y. Choi, Y.H. Lee, *ACS Nano* 4 (2010) 4595–4600.
- [57] H. Pinto, A. Markevich, *Beilstein J. Nanotechnol.* 5 (2014) 1842–1848.
- [58] K.S. Mali, J. Greenwood, J. Adisoejoso, R. Phillipson, S. De Feyter, *Nanoscale* 7 (2015) 1566–1585.
- [59] P.A. Denis, *Chem. Phys. Lett.* 492 (2010) 251–257.
- [60] H. Wang, Y. Zhou, D. Wu, L. Liao, S. Zhao, H. Peng, Z. Liu, *Small* 9 (2013) 1316–1320.
- [61] W. Xu, L. Wang, Y. Liu, S. Thomas, H.-K. Seo, K.-I. Kim, K.S. Kim, T.-W. Lee, *Adv. Mater.* 27 (2015) 1619–1623.
- [62] W. Xu, T.-S. Lim, H.-K. Seo, S.-Y. Min, H. Cho, M.-H. Park, Y.-H. Kim, T.-W. Lee, *Small* 10 (2014) 1999–2005.
- [63] K.S. Mali, J. Greenwood, J. Adisoejoso, R. Phillipson, S. De Feyter, *Nanoscale* 7 (2015) 1566–1585.
- [64] H.-J. Shin, W.M. Choi, D. Choi, G.H. Han, S.-M. Yoon, H.-K. Park, S.-W. Kim, Y.W. Jin, S.Y. Lee, J.M. Kim, J.-Y. Choi, Y.H. Lee, *J. Am. Chem. Soc.* 132 (2010) 15603–15609.
- [65] H. Liu, Y. Liu, D. Zhu, *J. Mater. Chem.* 21 (2011) 3335–3345.
- [66] W.H. Lee, J.W. Suk, J. Lee, Y. Hao, J. Park, J.W. Yang, H.-W. Ha, S. Murali, H. Chou, D. Akinwande, *ACS Nano* 6 (2012) 1284.
- [67] K.K. Kim, A. Reina, Y. Shi, H. Park, L.-J. Li, Y.H. Lee, J. Kong, *Nanotechnology* 21 (2010) 285205.
- [68] H. Park, S. Chang, M. Smith, S. Gradečak, J. Kong, *Sci. Rep.* 3 (2013) 1581.
- [69] J.-B. Lee, K. Rana, B.H. Seo, J.Y. Oh, U. Jeong, J.-H. Ahn, *Carbon* 85 (2015) 261–268.
- [70] H. Park, R.M. Howden, M.C. Barr, V. Bulović, K. Gleason, J. Kong, *ACS Nano* 6 (2012) 6370–6377.
- [71] H. Park, S. Chang, J. Jean, J.J. Cheng, P.T. Araujo, M. Wang, M.G. Bawendi, M.S. Dresselhaus, V. Bulović, J. Kong, S. Gradečak, *Nano Lett.* 13 (2013) 233–239.
- [72] H. Kim, J. Byun, S.-H. Bae, T. Ahmed, J.-X. Zhu, S.-J. Kwon, Y. Lee, S.-Y. Min, C. Wolf, H.-K. Seo, J.-H. Ahn, T.-W. Lee, *Adv. Energy Mater.* 6 (2016) 1600172.
- [73] Y. Wang, X. Chen, Y. Zhong, F. Zhu, K.P. Loh, *Appl. Phys. Lett.* 95 (2009) 63302.
- [74] X. Qiao, Y. Tao, Q. Wang, D. Ma, C. Yang, L. Wang, J. Qin, F. Wang, *J. Appl. Phys.* 108 (2010) 34508.
- [75] A. Benor, S. Takizawa, C. Pérez-Bolívar, P. Anzenbacher, *Appl. Phys. Lett.* 96 (2010) 243310.
- [76] Y. Zhang, J. Lee, S.R. Forrest, *Nat. Commun.* 5 (2014) 5008.
- [77] T.-H. Han, W. Song, T.-W. Lee, *ACS Appl. Mater. Interfaces* 7 (2015) 3117–3125.
- [78] T.-H. Han, Y.-H. Kim, M.H. Kim, W. Song, T.-W. Lee, *ACS Appl. Mater. Interfaces* 8 (2016) 6152–6163.
- [79] T.-H. Han, M.-H. Park, S.-J. Kwon, S.-H. Bae, H.-K. Seo, H. Cho, J.-H. Ahn, T.-W. Lee, *NPG Asia Mater.* 8 (2016) e303.
- [80] J. Lee, T.-H. Han, M.-H. Park, D.Y. Jung, J. Seo, H.-K. Seo, H. Cho, E. Kim, J. Chung, S.-Y. Choi, T.-S. Kim, T.-W. Lee, *Nat. Commun.* 7 (2016) 11791.
- [81] S. Tongay, K. Berke, M. Lemaitre, Z. Nasrollahi, D.B. Tanner, A.F. Hebard, B.R. Appleton, *Nanotechnology* 22 (2011) 425701.
- [82] A. Kasry, M.A. Kuroda, G.J. Martyna, G.S. Tulevski, A.A. Bol, *ACS Nano* 4 (2010) 3839–3844.
- [83] J. Wu, M. Agrawal, H.A. Becerril, Z. Bao, Z. Liu, Y. Chen, P. Peumans, *ACS Nano* 4 (2010) 43–48.
- [84] D.W. Lee, T.-K. Hong, D. Kang, J. Lee, M. Heo, J.Y. Kim, B.-S. Kim, H.S. Shin, *J. Mater. Chem.* 21 (2011) 3438–3442.
- [85] H. Chang, G. Wang, A. Yang, X. Tao, X. Liu, Y. Shen, Z. Zheng, *Adv. Funct. Mater.* 20 (2010) 2893–2902.
- [86] X. Wu, S. Li, Y. Zhao, Y. Tang, J. Liu, X. Guo, D. Wu, G. He, *ACS Appl. Mater. Interfaces* 6 (2014) 15753–15759.
- [87] T. Sun, Z.L. Wang, Z.J. Shi, G.Z. Ran, W.J. Xu, Z.Y. Wang, Y.Z. Li, L. Dai, G.G. Qin, *Appl. Phys. Lett.* 96 (2010) 13301.
- [88] A. Kuruvila, P.R. Kidambi, J. Kling, J.B. Wagner, J. Robertson, S. Hofmann, J. Meyer, *J. Mater. Chem.* C 2 (2014) 6940–6945.
- [89] N. Li, S. Oida, G.S. Tulevski, S.-J. Han, J.B. Hannon, D.K. Sadana, T.-C. Chen, *Nat. Commun.* 4 (2013) 2294.
- [90] J. Meyer, P.R. Kidambi, B.C. Bayer, C. Weijtens, A. Kuhn, A. Centeno, A. Pesquera, A. Zurutuza, J. Robertson, S. Hofmann, *Sci. Rep.* 4 (2014) 5380.

- [91] H.-K. Seo, H. Kim, J. Lee, M.-H. Park, S.-H. Jeong, Y.-H. Kim, S.-J. Kwon, T.-H. Han, T.-W. Lee, *Adv. Mater.* 12 (2017) 1605587.
- [92] Y.-H. Kim, H. Cho, J.H. Heo, T.-S. Kim, N. Myoung, C.-L. Lee, S.H. Im, T.-W. Lee, *Adv. Mater.* 27 (2015) 1248–1254.
- [93] Y.-C. Hsiao, T. Wu, M. Li, Q. Liu, W. Qin, B. Hu, *J. Mater. Chem. A* 3 (2015) 15372–15385.
- [94] S.-Y. Kim, J.-J. Kim, *Org. Electron.* 13 (2012) 1081–1085.
- [95] S.D. Stranks, G.E. Eperon, G. Grancini, C. Menelaou, M.J.P. Alcocer, T. Leijtens, L. M. Herz, A. Petrozza, H.J. Snaith, *Science* 342 (2013) 341–344.
- [96] Z.-K. Tan, R.S. Moghaddam, M.L. Lai, P. Docampo, R. Higler, F. Deschler, M. Price, A. Sadhanala, L.M. Pazos, D. Credgington, F. Hanusch, T. Bein, H.J. Snaith, R.H. Friend, *Nat. Nanotechnol.* 9 (2014) 687–692.
- [97] H. Cho, S.-H. Jeong, M.-H. Park, Y.-H. Kim, C. Wolf, C.-L. Lee, J.H. Heo, A. Sadhanala, N. Myoung, S. Yoo, S.H. Im, R.H. Friend, T.-W. Lee, *Science* 350 (2015) 1222–1225.
- [98] F. Filliaux, S. Menu, J. Conard, H. Fuzellier, S.W. Parker, A.C. Hanon, J. Tomkinson, *Chem. Phys.* 242 (1999) 273–281.
- [99] M.S.A. Abdou, S. Holdcroft, *Synth. Met.* 60 (1993) 93–96.
- [100] H.-J. Shin, S.M. Kim, S.-M. Yoon, A. Benayad, K.K. Kim, S.J. Kim, H.K. Park, J.-Y. Choi, Y.H. Lee, *J. Am. Chem. Soc.* 130 (2008) 2062–2066.
- [101] D. Kim, D. Lee, Y. Lee, D.Y. Jeon, *Adv. Funct. Mater.* 23 (2013) 5049–5055.
- [102] K.C. Kwon, K.S. Choi, S.Y. Kim, *Adv. Funct. Mater.* 22 (2012) 4724–4731.
- [103] P.R. Kidambi, C. Weijtens, J. Robertson, S. Hofmann, J. Meyer, *Appl. Phys. Lett.* 106 (2015) 063304.
- [104] X.C. Dong, D.L. Fu, W.J. Fang, Y.M. Shi, P. Chen, L.J. Li, *Small* 5 (2009) 1422.
- [105] C.L. Hsu, C.T. Lin, J.H. Huang, C.W. Chu, K.H. Wei, L.J. Li, *ACS Nano* 6 (2012) 5031.
- [106] W. Chen, S. Chen, D.C. Qi, X.Y. Gao, A.T.S. Wee, *J. Am. Chem. Soc.* 129 (2007) 10418.
- [107] Y.-H. Kim, T.-H. Han, H. Cho, S.-Y. Min, C.-L. Lee, T.-W. Lee, *Adv. Funct. Mater.* 24 (2014) 3808–3814.
- [108] P. Wei, J.H. Oh, G. Dong, Z. Bao, *J. Am. Chem. Soc.* 132 (2010) 8852–8853.
- [109] P.A. Denis, F. Iribarne, *J. Phys. Chem. C* 119 (2015) 15103–15111.
- [110] X. Gao, J. Jang, S. Nagase, *J. Phys. Chem. C* 114 (2010) 832–842.
- [111] I.-Y. Lee, H.-Y. Park, J.-H. Park, J. Lee, W.-S. Jung, H.-Y. Yu, S.-W. Kim, G.-H. Kim, J.-H. Park, *Org. Electron.* 14 (2013) 1586–1590.
- [112] Y. Kim, J. Ryu, M. Park, E.S. Kim, J.M. Yoo, J. Park, J.H. Kang, B.H. Hong, *ACS Nano* 8 (2014) 868–874.
- [113] B.-S. Kong, J. Geng, H.-T. Jung, *Chem. Commun.* (2009) 2174–2176.
- [114] J.O. Hwang, J.S. Park, D.S. Choi, J.Y. Kim, S.H. Lee, K.E. Lee, Y.-H. Kim, M.H. Song, S. Yoo, S.O. Kim, *ACS Nano* 6 (2012) 159–167.
- [115] S. Sanders, A. Cabrero-Vilatela, P.R. Kidambi, J.A. Alexander-Webber, C. Weijtens, P. Braeuner-Werner, A.I. Aria, M.M. Qasim, T.D. Wilkinson, J. Robertson, S. Hofmann, J. Meyer, *Nanoscale* 7 (2015) 13135–13142.
- [116] Y. Li, D.-Q. Zhang, L. Duan, R. Zhang, L.-D. Wang, Y. Qiu, *Appl. Phys. Lett.* 90 (2007) 012119.
- [117] J. Zhao, Y. Cai, J.-P. Yang, H.-X. Wei, Y.-H. Deng, Y.-Q. Li, S.-T. Lee, J.-X. Tang, *Appl. Phys. Lett.* 101 (2012) 193303.
- [118] C. Hartwigsen, W. Witschel, E. Spohr, *Phys. Rev. B* 55 (1997) 4953–4959.
- [119] L.S. Liao, W.K. Slusarek, T.K. Hatwar, M.L. Ricks, D.L. Comfort, *Adv. Mater.* 20 (2008) 324–329.
- [120] T.-W. Lee, T. Noh, B.-K. Choi, M.-S. Kim, D.W. Shin, *Appl. Phys. Lett.* 92 (2008) 043301.
- [121] P.-H. Ho, Y.-C. Yeh, D.-Y. Wang, S.-S. Li, H.-A. Chen, Y.-H. Chung, C.-C. Lin, W.-H. Wang, C.-W. Chen, *ACS Nano* 6 (2012) 6215–6221.
- [122] Y. Sun, S.R. Forrest, *Nat. Photon.* 2 (2008) 483–487.
- [123] H. Cho, J.W. Shin, N.S. Cho, J. Moon, J.H. Han, Y.D. Kwon, S. Cho, J.I. Lee, *IEEE J. Sel. Top. Quantum Electron.* 22 (2016) 48–53.
- [124] F. Bouville, E. Maire, S. Meille, B. Van de Moortèle, A.J. Stevenson, S. Deville, *Nat. Mater.* 13 (2014) 508–514.
- [125] Y.-W. Su, S.-C. Lan, K.-H. Wei, *Mater. Today* 15 (2012) 554–562.
- [126] C. Hontoria-Lucas, A.J. López-Peinado, J.D. d. López-González, M.L. Rojas-Cervantes, R.M. Martín-Aranda, *Carbon* 33 (1995) 1585–1592.
- [127] G. Eda, Y.-Y. Lin, S. Miller, C.-W. Chen, W.-F. Su, M. Chhowalla, *Appl. Phys. Lett.* 92 (2008) 233305.
- [128] J. Wu, H.A. Becerril, Z. Bao, Z. Liu, Y. Chen, P. Peumans, *Appl. Phys. Lett.* 92 (2008) 263302.
- [129] E. Kymakis, K. Savva, M.M. Stylianakis, C. Fotakis, E. Stratakis, *Adv. Funct. Mater.* 23 (2013) 2742–2749.
- [130] H. Feng, R. Cheng, X. Zhao, X. Duan, J. Li, *Nat. Commun.* 4 (2013) 1539.
- [131] H. Park, J. a Rowehl, K.K. Kim, V. Bulovic, J. Kong, *Nanotechnology* 21 (2010) 505204.
- [132] Y.M. Lee, W. Kim, Y.H. Kim, J.K. Kim, J. Jang, W.-S. Choe, J.H. Park, P.J. Yoo, *ChemSusChem* 8 (2015) 2385–2391.
- [133] Y. Wang, S.W. Tong, X.F. Xu, B. Özyilmaz, K.P. Loh, *Adv. Mater.* 23 (2011) 1514–1518.
- [134] K.-G. Lim, S. Ahn, Y.-H. Kim, Y. Qi, T.-W. Lee, *Energy Environ. Sci.* 9 (2016) 932–939.
- [135] H. Park, J. Kong, *Adv. Energy Mater.* 4 (2014) 1301280.
- [136] K.-S. Shin, H. Jo, H.-J. Shin, W.M. Choi, J.-Y. Choi, S.-W. Kim, *J. Mater. Chem.* 22 (2012) 13032–13038.
- [137] K.-S. Shin, H. Jo, H.-J. Shin, W.M. Choi, J.-Y. Choi, S.-W. Kim, *J. Mater. Chem.* 22 (2012) 13032–13038.
- [138] S. Lee, J.-S. Yeo, Y. Ji, C. Cho, D.-Y. Kim, S.-I. Na, B.H. Lee, T. Lee, *Nanotechnology* 23 (2012) 344013.
- [139] Y. Wang, S.W. Tong, X.F. Xu, B. Özyilmaz, K.P. Loh, *Adv. Mater.* 23 (2011) 1514–1518.
- [140] J. Bardeen, *Phys. Rev.* 71 (1947) 717–727.
- [141] G. Jo, S.-I. Na, S.-H. Oh, S. Lee, T.-S. Kim, G. Wang, M. Choe, W. Park, J. Yoon, D.-Y. Kim, Y.H. Kahng, T. Lee, *Appl. Phys. Lett.* 97 (2010) 213301.
- [142] M. Choe, B.H. Lee, G. Jo, J. Park, W. Park, S. Lee, W.-K. Hong, M.-J. Seong, Y.H. Kahng, K. Lee, *Org. Electron.* 11 (2010) 1864–1869.
- [143] L. Gomez De Arco, Y. Zhang, C.W. Schlenker, K. Ryu, M.E. Thompson, C. Zhou, *ACS Nano* 4 (2010) 2865–2873.
- [144] H. Park, P.R. Brown, V. Bulović, J. Kong, *Nano Lett.* 12 (2012) 133–140.
- [145] Y.-Y. Choi, S.J. Kang, H.-K. Kim, W.M. Choi, S.-I. Na, *Sol. Energy Mater. Sol. Cells* 96 (2012) 281–285.
- [146] S. Lee, J.-S. Yeo, Y. Ji, C. Cho, D.-Y. Kim, S.-I. Na, B.H. Lee, T. Lee, *Nanotechnology* 23 (2012) 344013.
- [147] H. Park, J. Kong, *Adv. Energy Mater.* 4 (2014) 1301280.
- [148] H. Park, S. Chang, X. Zhou, J. Kong, T. Palacios, S. Gradečak, *Nano Lett.* 14 (2014) 5148–5154.
- [149] Y.M. Lee, W. Kim, Y.H. Kim, J.K. Kim, J. Jang, W.-S. Choe, J.H. Park, P.J. Yoo, *ChemSusChem* 8 (2015) 2385–2391.
- [150] L. Gomez De Arco, Y. Zhang, C.W. Schlenker, K. Ryu, M.E. Thompson, C. Zhou, *ACS Nano* 4 (2010) 2865–2873.
- [151] H. Park, S. Chang, X. Zhou, J. Kong, T. Palacios, S. Gradečak, *Nano Lett.* 14 (2014) 5148–5154.
- [152] W.S. Yang, J.H. Noh, N.J. Jeon, Y.C. Kim, S. Ryu, J. Seo, S. Il Seok, *Science* 348 (2015) 1234–1237.
- [153] X. Li, D. Bi, C. Yi, J.-D. Décuppet, J. Luo, S.M. Zakeeruddin, A. Hagfeldt, M. Grätzel, *Science* 353 (2016) 58–62.
- [154] H. Sung, N. Ahn, M.S. Jang, J.-K. Lee, H. Yoon, N.-G. Park, M. Choi, *Adv. Energy Mater.* 6 (2016) 1501873.
- [155] J. Yoon, H. Sung, G. Lee, W. Cho, N. Ahn, H.S. Jung, M. Choi, *Energy Environ. Sci.* 10 (2017) 337–345.
- [156] Z. Liu, P. You, C. Xie, G. Tang, F. Yan, *Nano Energy* 28 (2016) 151–157.
- [157] P. You, Z. Liu, Q. Tai, S. Liu, F. Yan, *Adv. Mater.* 27 (2015) 3632–3638.
- [158] H. Kim, K.-G. Lim, T.-W. Lee, *Energy Environ. Sci.* 9 (2016) 12–30.
- [159] H. Sung, N. Ahn, M.S. Jang, J.-K. Lee, H. Yoon, N.-G. Park, M. Choi, *Adv. Energy Mater.* 6 (2016) 1501873.
- [160] J.J. Liou, F. Schwierz, *Solid. State. Electron.* 47 (2003) 1881–1895.
- [161] A. Nourbakhsh, M. Cantoro, T. Vosch, G. Pourtois, F. Clemente, M.H. van der Veen, J. Hofkens, M.M. Heyns, S.D. Gendt, B.F. Sels, *Nanotechnology* 21 (2010) 435203.
- [162] T. Goksu, R.R. Nair, A. Bonetti, M. Böhmmer, A. Lombardo, K.S. Novoselov, A.K. Geim, A.C. Ferrari, A. Hartschuh, *ACS Nano* 3 (2009) 3963–3968.
- [163] D.C. Elias, R.R. Nair, T.M.G. Mohiuddin, S.V. Morozov, P. Blake, M.P. Halsall, A.C. Ferrari, D.W. Boukhvalov, M.I. Katsonelos, A.K. Geim, K.S. Novoselov, *Science* 323 (2009) 610–613.
- [164] J. Son, S. Lee, S.J. Kim, B.C. Park, H.-K. Lee, S. Kim, J.H. Kim, B.H. Hong, J. Hong, *Nat. Commun.* 7 (2016) 13261.
- [165] J. Balakrishnan, G. Kok Wai Koon, M. Jaiswal, A.H. Castro Neto, B. Ozyilmaz, *Nat. Phys.* 9 (2013) 284–287.
- [166] R. Balog, B. Jørgensen, J. Wells, E. Lægsgaard, P. Hofmann, F. Besenbacher, L. Hornekær, J. Am. Chem. Soc. 131 (2009) 8744–8745.
- [167] J. Dai, J. Yuan, P. Giannozzi, *Appl. Phys. Lett.* 95 (2009) 232105.
- [168] M.Y. Han, B. Özyilmaz, Y. Zhang, P. Kim, *Phys. Rev. Lett.* 98 (2007) 206805.
- [169] W. Xu, H.-K. Seo, S.-Y. Min, H. Cho, T.-S. Lim, C.-Y. Oh, Y. Lee, T.-W. Lee, *Adv. Mater.* 26 (2014) 3459–3464.
- [170] X. Li, X. Wang, L. Zhang, S. Lee, H. Dai, *Science* 319 (2008) 1229–1232.
- [171] P.B. Bennett, Z. Pedramrazi, A. Madani, Y.-C. Chen, D.G. de Oteyza, C. Chen, F.R. Fischer, M.F. Crommie, J. Bokor, *Appl. Phys. Lett.* 103 (2013) 253114.
- [172] J. Cai, P. Ruffieux, R. Jaafar, M. Bieri, T. Braun, S. Blankenburg, M. Muoth, A.P. Seitsonen, M. Saleh, X. Feng, K. Mullen, R. Fasel, *Nature* 466 (2010) 470–473.
- [173] W. Xu, T.-W. Lee, *Mater. Horiz.* 3 (2016) 186–207.
- [174] C.-G. Lee, S. Park, R.S. Ruoff, A. Dodabalapur, *Appl. Phys. Lett.* 95 (2009) 23304.
- [175] S. Pang, H.N. Tsao, X. Feng, K. Müllen, *Adv. Mater.* 21 (2009) 3488–3491.
- [176] B. Kang, S. Lim, W.H. Lee, S.B. Jo, K. Cho, *Adv. Mater.* 25 (2013) 5856–5862.
- [177] S. Lee, G. Jo, S.-J. Kang, G. Wang, M. Choe, W. Park, D.-Y. Kim, Y.H. Kahng, T. Lee, *Adv. Mater.* 23 (2011) 100–105.
- [178] W.H. Lee, J. Park, S.H. Sim, S.B. Jo, K.S. Kim, B.H. Hong, K. Cho, *Adv. Mater.* 23 (2011) 1752–1756.
- [179] S.K. Lee, J.W. Yang, H.H. Kim, S.B. Jo, B. Kang, H. Bong, H.C. Lee, G. Lee, K.S. Kim, K. Cho, *ACS Nano* 8 (2014) 7968–7975.
- [180] J. Park, W.H. Lee, S. Huh, S.H. Sim, S.B. Kim, K. Cho, B.H. Hong, K.S. Kim, *J. Phys. Chem. Lett.* 2 (2011) 841.
- [181] W.H. Lee, J. Park, S.H. Sim, S. Lim, K.S. Kim, B.H. Hong, K. Cho, *J. Am. Chem. Soc.* 133 (2011) 4447.
- [182] H. Gao, L. Wang, J. Zhao, F. Ding, J. Lu, *J. Phys. Chem. C* 115 (2011) 3236–3242.
- [183] M.-H. Park, J.-Y. Kim, T.-H. Han, T.-S. Kim, H. Kim, T.-W. Lee, *Adv. Mater.* 27 (2015) 4308–4314.
- [184] S. Reineke, F. Lindner, G. Schwartz, N. Seidler, K. Walzer, B. Lussem, K. Leo, *Nature* 459 (2009) 234–238.
- [185] M. Mesta, M. Carvelli, R.J. de Vries, H. van Eersel, J.J.M. van der Holst, M. Schober, M. Furno, B. Lüssem, K. Leo, P. Loebel, R. Coehorn, P.A. Bobbert, *Nat. Mater.* 12 (2013) 652–658.
- [186] Y.-J. Pu, G. Nakata, F. Satoh, H. Sasabe, D. Yokoyama, J. Kido, *Adv. Mater.* 24 (2012) 1765–1770.

- [187] A.C. Arias, J.D. MacKenzie, I. McCulloch, J. Rivnay, A. Salleo, *Chem. Rev.* 110 (2010) 3–24.
- [188] S.-Y. Min, T.-S. Kim, B.J. Kim, H. Cho, Y.-Y. Noh, H. Yang, J.H. Cho, T.-W. Lee, *Nat. Commun.* 4 (2013) 1773.
- [189] H. Ham, J. Park, Y. Kim, *Org. Electron.* 12 (2011) 2174–2179.
- [190] A.A. Dameron, S.D. Davidson, B.B. Burton, P.F. Garcia, R.S. McLean, S.M. George, *J. Phys. Chem. C* 112 (2008) 4573–4580.
- [191] S. Sarkar, J.H. Culp, J.T. Whyland, M. Garvan, V. Misra, *Org. Electron.* 11 (2010) 1896–1900.
- [192] J. Granstrom, J.S. Swensen, J.S. Moon, G. Rowell, J. Yuen, A.J. Heeger, *Appl. Phys. Lett.* 93 (2008) 193304.
- [193] P.F. Garcia, R.S. McLean, M.H. Reilly, M.D. Groner, S.M. George, *Appl. Phys. Lett.* 89 (2006) 31915.
- [194] J.S. Bunch, S.S. Verbridge, J.S. Alden, A.M. van der Zande, J.M. Parpia, H.G. Craighead, P.L. McEuen, *Nano Lett.* 8 (2008) 2458–2462.
- [195] R.R. Nair, H.A. Wu, P.N. Jayaram, I.V. Grigorieva, A.K. Geim, *Science* 335 (2012) 442–444.
- [196] S. Chen, L. Brown, M. Levendorf, W. Cai, S.-Y. Ju, J. Edgeworth, X. Li, C.W. Magnuson, A. Velamakanni, R.D. Piner, J. Kang, J. Park, R.S. Ruoff, *ACS Nano* 5 (2011) 1321–1327.
- [197] Z. Liu, J. Li, F. Yan, *Adv. Mater.* 25 (2013) 4296–4301.
- [198] H. Yamaguchi, J. Granstrom, W. Nie, H. Sojoudi, T. Fujita, D. Voiry, M. Chen, G. Gupta, A.D. Mohite, S. Graham, M. Chhowalla, *Adv. Energy Mater.* 4 (2014) 1300986.
- [199] K. Choi, S. Nam, Y. Lee, M. Lee, J. Jang, S.J. Kim, Y.J. Jeong, H. Kim, S. Bae, J.-B. Yoo, S.M. Cho, J.-B. Choi, H.K. Chung, J.-H. Ahn, C.E. Park, B.H. Hong, *ACS Nano* 9 (2015) 5818–5824.
- [200] J.Y. Oh, S. Rondeau-Gagné, Y.-C. Chiu, A. Chortos, F. Lissel, G.-J.N. Wang, B.C. Schroeder, T. Kurosawa, J. Lopez, T. Katsumata, J. Xu, C. Zhu, X. Gu, W.-G. Bae, Y. Kim, L. Jin, J.W. Chung, J.B.-H. Tok, Z. Bao, *Nature* 539 (2016) 411–415.
- [201] S. Won, Y. Hwangbo, S.-K. Lee, K.-S. Kim, K.-S. Kim, S.-M. Lee, H.-J. Lee, J.-H. Ahn, J.-H. Kim, S.-B. Lee, *Nanoscale* 6 (2014) 6057–6064.
- [202] B.W. An, B.G. Hyun, S.-Y. Kim, M. Kim, M.-S. Lee, K. Lee, J.B. Koo, H.Y. Chu, B.-S. Bae, J.-U. Park, *Nano Lett.* 14 (2014) 6322–6328.